
Mechanics of Hydraulic Fracturing

Mark G. Mack, Schlumberger Dowell
Norman R. Warpinski, Sandia National Laboratories

6-1. Introduction

The mechanics of hydraulic fracturing is a convenient description of the processes and mechanisms that are important to fracturing technology. Mechanics generally refers to an engineering discipline that is concerned with the mechanical properties of the material under consideration and the response of that material to the physical forces of its environment. Hydraulic fracturing is complicated because it involves four different types of mechanics: fluid, solid, fracture and thermal. In fracturing, fluid mechanics describes the flow of one, two or three phases within the fracture; solid mechanics describes the deformation or opening of the rock because of the fluid pressure; fracture mechanics describes all aspects of the failure and parting that occur near the tip of the hydraulic fracture; and thermal mechanics describes the exchange of heat between the fracturing fluid and the formation. Furthermore, the responses are coupled and depend on each other. To develop tools for the design and analysis of a process as complicated as hydraulic fracturing, it is necessary to build models that describe each of the responses sufficiently. This chapter describes the history and technology associated with these models.

A model of a process is a representation that captures the essential features of the process in a manner that provides an understanding of the process (Starfield *et al.*, 1990). The construction of the model depends on the type of question it is required to answer. The three main types of models are physical, empirical and mechanistic (or analytic). Each has advantages and disadvantages, which are outlined in the following.

- Physical models are scale models of actual processes. The primary advantage of such models is that, by definition, they incorporate the correct assumptions of material behavior. For example, if a fracturing fluid is pumped between a pair of par-

allel rock faces with roughness comparable to fractured rock, no assumptions need to be made about how the fluid behaves rheologically. Instead, how it behaves is simply observed. Unfortunately, physical models are usually expensive to build and use.

In addition, there are major issues of scale-up if the model is significantly smaller than the actual structure. For example, in a model of a bridge, the weight is proportional to the scale factor cubed, but the length of any element is proportional only to the scale factor. Thus, even elements that do not fail in the model may fail in practice. Nevertheless, scale models are useful provided an appropriate dimensional analysis is performed and if the scale factor is not too great (de Pater *et al.*, 1993).

- Empirical models are developed by observation. Typically, laboratory or field data are gathered and combined to create design charts or empirical equations, which can then be used to predict or design future cases. For example, if 100 wells in an area have been fractured with different-size treatments, 6 months of cumulative production could be plotted against treatment size. Provided the scatter is not too great, the production response from a new treatment can be predicted from the historical data.

The advantages of empirical models are that no assumptions need to be made about any behavior and there is no scale effect. The primary disadvantage is low confidence in extrapolation outside the range of the data. The 100-well data set may be useful in the same field, even for treatments slightly larger than any in the data set, but is most likely irrelevant in another area. For an empirical model to be useful, the data must be arranged in terms of suitable dimensionless variables, so that it is as general as possible. For example, the 100-well data set may be useful in a different area provided the results are normalized with respect to permeability and pay thickness. To obtain the right

dimensionless quantities, however, it is generally necessary to have at least some understanding of the mechanics of the physical process being modeled.

- Analytical models are mathematical representations of a physical reality in which the governing mechanics are stated in the form of equations. The equations typically define both physical laws, such as conservation of mass, and constitutive laws, such as elasticity. The former are inviolable laws of nature, whereas the latter are hypotheses of physical behavior that require laboratory work to confirm that they are applicable and to determine the constants in the model.

The major advantages of analytical models are that they may be extrapolated outside the range in which they were developed, provided the various component laws still hold. Thus, if the elastic constant of a spring has been measured, the force required for a given displacement of the spring can be predicted, even for displacements that have not been tested. If the spring is cut in half, the behavior of each half can be predicted. Perhaps the greatest limitation of analytical models, however, is the assumptions that are made in developing the model. For example, it is typically assumed that rock is homogeneous, yet there are many cases where it is fractured or otherwise variable from point to point, and this may not be accounted for in the model.

A simulator is a computational implementation of a model. Many analytical models are tractable only if they are solved numerically, unless a large number of approximations or simplifying assumptions are made. With the widespread availability of computers, it is now generally accepted that better answers may be obtained by numerically solving a more general model rather than by solving a simplified model exactly. Nevertheless, it must be emphasized that useful rules of thumb and relations between quantities can often be developed much more easily using analytic solutions, which provide insight into the relations between parameters affecting the results for more complex conditions. Some of the simplest rules would probably not be “discovered” from a numerical solution without a great deal of effort, if at all. An extensive presentation of analytic-based solutions and approximations for the mechanics of hydraulic fracturing was provided by Valkó and Economides (1996).

Four important reasons for developing and using models of hydraulic fracture treatments are to

- perform economic optimization (i.e., determine what size treatment provides the highest rate of return on investment)
- design a pump schedule
- simulate the fracture geometry and proppant placement achieved by a specified pump schedule
- evaluate a treatment (by comparing the predictions of a model with actual behavior).

In each of these cases, the objective is a quantitative estimate of either the volume of fluid and proppant required to create a fracture with a desired conductivity and geometry or the geometry produced by a specified pump schedule.

6-2. History of early hydraulic fracture modeling

6-2.1. Basic fracture modeling

Sneddon (1946) and Sneddon and Elliot (1946) developed the solutions for the stress field and pressure associated with static pressurized cracks. They showed that the width of a static penny-shaped (i.e., circular) crack of radius R under constant pressure is given by the expression

$$w(r) = \frac{8p_{net}R(1-\nu^2)}{\pi E} \sqrt{(1-(r/R)^2)}, \quad (6-1)$$

which describes an ellipsoid, and the volume of the crack V by

$$V = \frac{16(1-\nu^2)R^3}{3E} p_{net}, \quad (6-2)$$

where the net pressure p_{net} is defined as the pressure in the crack minus the stress against which it opens, ν is Poisson’s ratio, and E is Young’s modulus. Sack (1946) showed that the pressure required to extend a crack of radius R under constant pressure is given by

$$p_{net} = \sqrt{\frac{\pi\gamma_f E}{2(1-\nu^2)R}}, \quad (6-3)$$

where γ_f is the specific fracture surface energy. Equations 6-1 and 6-2 are derived using the theory of linear elasticity, and Eq. 6-3 is derived using linear elastic fracture mechanics. The basis of Eq. 6-3 is that the energy required to create the surface area when a crack is propagated must equal the work done by the

pressure in the crack to open the additional width. A more detailed discussion of fracture mechanics is in Chapter 3. Combining Eqs. 6-2 and 6-3, Perkins and Kern (1961) showed that the pressure for propagation of a radial fracture is

$$p_{net} = \left(\frac{2\pi^3 \gamma_f^3 E^2}{3(1-\nu^2)^2 V} \right)^{1/5} \quad (6-4)$$

Thus, if the fracture volume is known, p_{net} can be calculated and Eq. 6-2 used to determine R . For example, if the injection rate q_i is constant, fluid friction in the fracture is negligible, and there is no leakoff, Eq. 6-4 can be substituted into Eq. 6-2 with the volume V replaced by $q_i t$ as

$$q_i t = \frac{16(1-\nu^2)R^3}{3E} \left(\frac{2\pi^3 \gamma_f^3 E^2}{3(1-\nu^2)^2 q_i t} \right)^{1/5}, \quad (6-5)$$

where t is the time. Rearranging and solving for R ,

$$R = \left[\frac{9E q_i^2 t^2}{128\pi \gamma_f (1-\nu^2)} \right]^{1/5} \quad (6-6)$$

Sneddon and Elliot (1946) also showed that for fractures of a fixed height h_f and infinite extent (i.e., plane strain), the maximum width is

$$w = \frac{2p_{net} h_f (1-\nu^2)}{E} \quad (6-7)$$

and the shape of the fracture is elliptical, so that the average width $\bar{w} = (\pi/4)w$. The term $E/(1-\nu^2)$ appears so commonly in the equations of hydraulic fracturing that it is convenient to define the plane strain modulus E' as

$$E' = \frac{E}{1-\nu^2}, \quad (6-8)$$

which is used for this chapter. (A plane strain deformation is one in which planes that were parallel before the deformation remain parallel afterward. This is generally a good assumption for fractures in which one dimension [length or height] is much greater than the other.)

6-2.2. Hydraulic fracture modeling

Several introductory and key papers published between the late 1950s and early 1970s that developed the foundation of hydraulic fracture modeling approach the problem by making different assumptions concern-

ing the importance of different aspects. Carter (1957) neglected both fluid viscosity effects and solid mechanics and concentrated on leakoff. Khristianovich and Zheltov (1955) made some simplifying assumptions concerning fluid flow and focused on fracture mechanics. Perkins and Kern (1961) assumed that fracture mechanics is relatively unimportant and focused on fluid flow. These three basic models are each described in some detail in following sections.

The first work on hydraulic fracture modeling was performed by several Russian investigators (summarized by Khristianovich *et al.*, 1959). The first reference in English is Khristianovich and Zheltov's (1955) paper. The other major contribution was the work of Perkins and Kern (1961). These models were developed to calculate the fracture geometry, particularly the width, for a specified length and flow rate, but did not attempt to satisfy the volume balance. Carter (1957) introduced a model that satisfies volume balance but assumes a constant, uniform fracture width. This model was used into the late 1970s for determining volume balance, with more realistic width profiles from the aforementioned geometry models to ensure that the fracture width was sufficient for proppant entry. This approach was made obsolete by extensions to the Khristianovich and Zheltov and Perkins and Kern models developed by Geertsma and de Klerk (1969) and Nordgren (1972), respectively. These two basic models, generally known as the KGD and PKN models after their respective developers, were the first to include both volume balance and solid mechanics.

The PKN and KGD models, both of which are applicable only to fully confined fractures, differ in one major assumption: the way in which they convert a three-dimensional (3D) solid and fracture mechanics problem into a two-dimensional (2D) (i.e., plane strain) problem. Khristianovich and Zheltov assumed plane strain in the horizontal direction; i.e., all horizontal cross sections act independently or equivalently, and all sections are identical (Fig. 6-1), which is equivalent to assuming that the fracture width changes much more slowly vertically along the fracture face from any point on the face than it does horizontally. In practice, this is true if the fracture height is much greater than the length or if complete slip occurs at the boundaries of the pay zone. Perkins and Kern, on the other hand, assumed that each vertical cross section acts independently (Fig. 6-2), which is equivalent to assuming that the pressure at any section is dominated by the height of the section rather than the length of

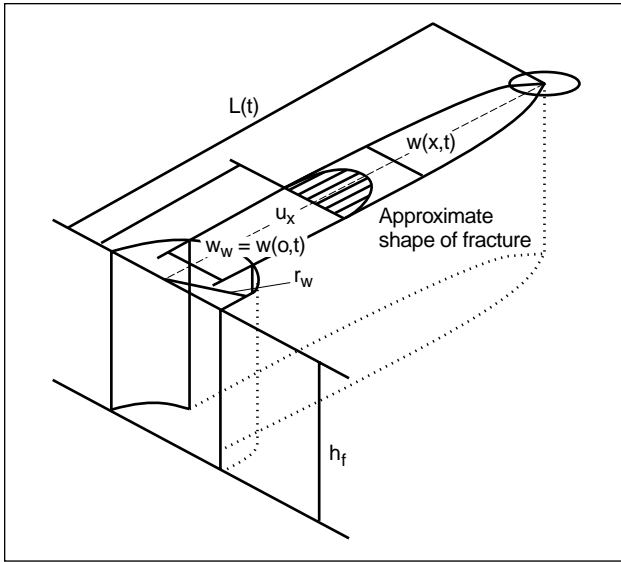


Figure 6-1. KGD fracture.

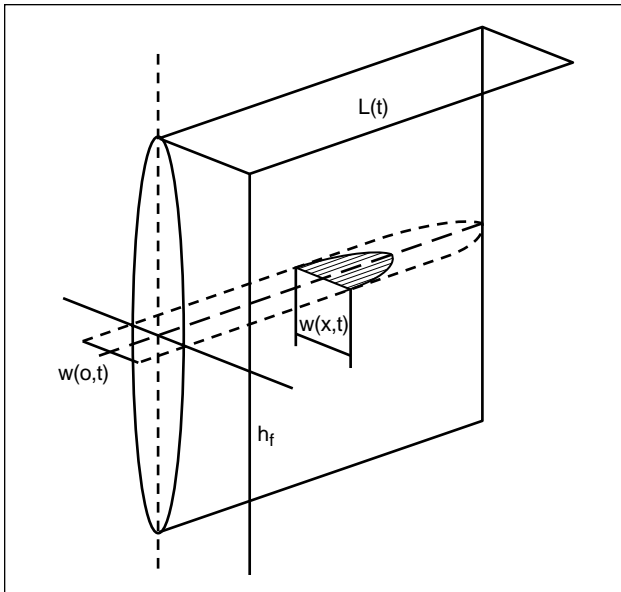


Figure 6-2. PKN fracture.

the fracture. This is true if the length is much greater than the height. This difference in one basic assumption of the models leads to two different ways of solving the problem and can also lead to different fracture geometry predictions. In the case of the PKN model, fracture mechanics and the effect of the fracture tip are not considered; the concentration is on the effect of fluid flow in the fracture and the corresponding pressure gradients. In the KGD model, however, the tip region plays a much more important role, and the fluid pressure gradients in the fracture can be approximated.

- Derivation of Perkins and Kern model of a vertical fracture

Perkins and Kern (1961) assumed that a fixed-height vertical fracture is propagated in a well-confined pay zone; i.e., the stresses in the layers above and below the pay zone are sufficiently large to prevent fracture growth out of the pay zone. They further assumed the conditions of Eq. 6-7, as shown in Fig. 6-2, that the fracture cross section is elliptical with the maximum width at a cross section proportional to the net pressure at that point and independent of the width at any other point (i.e., vertical plane strain). Although Perkins and Kern developed their solution for non-Newtonian fluids and included turbulent flow, it is assumed here that the fluid flow rate is governed by the basic equation for flow of a Newtonian fluid in an elliptical section (Lamb, 1932):

$$\frac{dp}{dx} = -\frac{64q\mu}{\pi h_f w^3}, \quad (6-9)$$

where p is the pressure, x is the distance along the fracture, and μ is the fluid viscosity.

Substituting Eq. 6-7 into Eq. 6-9, replacing the flow q by one-half of the injection rate ($q_i/2$) and assuming that the flow rate is constant along the fracture length (which implies that both leakoff and storage in the fracture resulting from width increases are neglected) obtains

$$p_{net}^3 dp_{net} = -\frac{4}{\pi} \frac{\mu q_i E'^3}{h_f^4} dx. \quad (6-10)$$

Integrating this expression along the fracture half-length L obtains, with $p_{net} = 0$ at the fracture tip,

$$p_{net} = \left[\frac{16\mu q_i E'^3}{\pi h_f^4} L \right]^{1/4}, \quad (6-11)$$

from which Eq. 6-7 implies that

$$w(x) = 3 \left[\frac{\mu q_i (L-x)}{E'} \right]^{1/4}. \quad (6-12)$$

In oilfield units (with q_i in bbl/min and w in in.), the width at the wellbore ($x = 0$) is

$$w_w = 0.38 \left(\frac{q_i \mu L}{E'} \right)^{1/4}. \quad (6-13)$$

For this model, the average width in the fracture is $\pi/4$ (about 80%) of the wellbore width. With a

Newtonian fluid, the model width is independent of the fracture height.

Perkins and Kern (1961) noted that the average net pressure in the fracture would greatly exceed the minimum pressure for propagation, calculated by an equation similar to Eq. 6-4, unless the fluid flow rate was extremely small or the fluid had an unrealistically low viscosity. Thus, under typical hydraulic fracturing conditions, the pressure resulting from fluid flow is far larger than the minimum pressure required to extend a stationary fracture. This justifies neglecting fracture mechanics effects in this model. Furthermore, they pointed out that the fracture would continue to extend after pumping stopped, until either leakoff limited further extension or the minimum pressure for fracture propagation was reached.

Several important observations concern this solution:

- assumption of plane strain behavior in the vertical direction
 - demonstration that fracture toughness could be neglected, because the energy required to propagate the fracture was significantly less than that required to allow fluid flow along the fracture length
 - assumption that leakoff and storage or volume change in the fracture could be neglected
 - assumption of fixed height
 - no direct provision of fracture length as part of the solution.
- Inclusion of leakoff

Although Perkins and Kern (1961) suggested that their paper could be used in practical applications, they neglected both leakoff and storage of fluid in the fracture. They assumed that some other method would be used to calculate the fracture length, such as that proposed by Carter (1957).

Carter introduced the basic equation for leakoff, which is discussed in detail in Section 6-4. The leakoff velocity u_L at a point on the fracture wall is

$$u_L = \frac{C_L}{\sqrt{t - t_{exp}}}, \quad (6-14)$$

where C_L is the leakoff coefficient, t is the current time, and t_{exp} is the time at which point u_L was exposed. Carter introduced a simple mass balance:

$$q_i = q_L + q_f, \quad (6-15)$$

where q_L is the leakoff rate over the whole fracture and q_f is the volume rate of storage in the fracture. If the fracture width \bar{w} is assumed to be constant in both space and time, Eq. 6-15 can be written as

$$q_i = 2 \int_0^{A_f(t)} u_L dA_f + \bar{w} \frac{\partial A_f}{\partial t}, \quad (6-16)$$

where A_f is the fracture face area. Carter showed that Eq. 6-16 can be rewritten as

$$q_i = 2 \int_0^t u_L(t - \lambda) \frac{\partial A_f}{\partial \lambda} d\lambda + \bar{w} \frac{\partial A_f}{\partial t}. \quad (6-17)$$

Substituting Eq. 6-14 into Eq. 6-17 and using Laplace transformations, he showed that this could be solved to obtain

$$A_f = \frac{q_i \bar{w}}{4\pi C_L^2} \left(e^{S^2} \operatorname{erfc}(S) + \frac{2}{\sqrt{\pi}} S - 1 \right), \quad (6-18)$$

where

$$S = \frac{2C_L \sqrt{\pi t}}{\bar{w}}. \quad (6-19)$$

The fracture wing length L as a function of time is then obtained by dividing the area by twice the fracture height. Harrington and Hannah (1975) showed (see Sidebar 6A) that Eq. 6-18 could be simplified with little loss of accuracy to

$$A_f = \frac{q_i t}{\bar{w} + 2C_L \sqrt{2t}}, \quad (6-20)$$

which is much easier to work with for simple calculations.

Designs were performed by iterating between the Carter technique to obtain the fracture length as a function of time (Eq. 6-19) and the Perkins and Kern model to determine the width (Eq. 6-13) until a consistent solution was found, and then Eq. 6-11 was used to determine the pressure.

Nordgren (1972) added leakoff and storage within the fracture (resulting from increasing width) to the Perkins and Kern model, deriving what is now known as the PKN model. To add storage and leakoff, the equation of continuity (i.e., conservation of mass) is added to the set of equations (6-7 and 6-9) used by Perkins and Kern:

$$\frac{\partial q}{\partial x} + q_L + \frac{\partial A}{\partial t} = 0, \quad (6-21)$$

6A. Approximation to the Carter equation for leakoff

Equation 6-20 was derived by assuming that the exposure time t_{exp} in Eq. 6-14 is equal to $t/2$, for which integration gives the volume lost per unit area of the fracture face as

$$u_L = 2C_L \sqrt{t/2} = C_L \sqrt{2t}. \quad (6A-1)$$

Harrington and Hannah (1975) introduced efficiency as:

$$\eta = \frac{V_f}{V_i} = \frac{V_f}{V_f + V_L}, \quad (6A-2)$$

where V_f is the fracture volume, V_i is the volume of fluid injected, and V_L is the leaked-off volume, which in terms of Eq. 6-20 becomes

$$\eta = \frac{\bar{w}}{\bar{w} + 2C_L \sqrt{2t}} \quad (6A-3)$$

or

$$\eta = \frac{1}{1 + 2C_L \sqrt{2t}/\bar{w}}. \quad (6A-4)$$

This approximation allows the efficiency η and S in Eq. 6-19 to be related by

$$\eta = \frac{1}{1 + 0.8S} \quad (6A-5)$$

or

$$S = 1.25 \frac{1 - \eta}{\eta}, \quad (6A-6)$$

which also shows that S tends to 0 as the efficiency tends to 1 (negligible fluid loss) and that S tends to infinity for zero efficiency (i.e., negligible fracture volume relative to the fluid-loss volume). An improved approximation for $\sqrt{2t}$ is in Chapter 9 (i.e., $g_0 \sqrt{t}$, where g_0 is within 5% of 1.5 and varies with efficiency).

where q is the volume flow rate through a cross section, A is the cross-sectional area of the fracture ($\pi w h_f / 4$ for the PKN model), and q_L is the volume rate of leakoff per unit length:

$$q_L = 2h_f u_L, \quad (6-22)$$

where u_L is from Eq. 6-14. The cross-sectional area A is not A_f , the area of the fracture face. Substituting for pressure in terms of width, similar to the method of Perkins and Kern, Eq. 6-21 can be written as

$$\frac{E'}{128\mu h_f} \frac{\partial^2 w^4}{\partial x^2} = \frac{8C_L}{\pi \sqrt{t - t_{exp}}(x)} + \frac{\partial w}{\partial t}. \quad (6-23)$$

Nordgren solved this equation numerically in a dimensionless form to obtain the width and length as a function of time. The dimensionless time t_D used in the solution is defined by

$$t_D = \left[\frac{64C_L^5 E' h_f}{\pi^3 \mu q_i^2} \right]^{2/3} t. \quad (6-24)$$

Dimensionless time t_D is a stronger function of the leakoff coefficient ($C_L^{10/3}$) than time t^1 .

Because Nordgren's solution was ultimately obtained numerically, it is not possible to express it analytically. However, some useful approximations to the fracture geometry for the limiting cases of high and low efficiency can be obtained (see Sidebar 6B). These expressions provide useful physical insight into the behavior of fractures. For example, the equation for length when leakoff is high (i.e., low efficiency) indicates that the length is determined simply by a mass balance between leakoff and flow into the fracture; i.e., the length increases just fast enough for the leakoff rate to balance the inflow. Analytical extensions to the PKN model that include power law fluids and explicit consideration of the efficiency between the bounding values of 0 and 1 can be obtained.

It is important to reemphasize that even for contained fractures, the PKN solution is valid only when the fracture length is much greater than the height. Typically, if the height is less than about one-third of the total (tip to tip) fracture length, the error resulting from the plane strain assumption is negligible.

6B. Approximations to Nordgren's equations

Nordgren (1972) derived two limiting approximations, for storage-dominated, or high-efficiency ($t_D < 0.01$), cases and for leakoff-dominated, or low-efficiency ($t_D > 1.0$), cases, with t_D defined by Eq. 6-24. They are useful for quick estimates of fracture geometry and pressure within the limits of the approximations. Both limiting solutions overestimate both the fracture length and width (one neglects fluid loss and the other neglects storage in the fracture), although within the stated limits on t_D , the error is less than 10%.

The storage-dominated ($\eta \rightarrow 1$) approximation is

$$L(t) = 0.39 \left[\frac{E' q_i^3}{\mu h_f^4} \right]^{1/5} t^{4/5} \quad (6B-1)$$

$$w_w = 2.18 \left[\frac{\mu q_i^2}{E' h_f} \right]^{1/5} t^{1/5}, \quad (6B-2)$$

and the high-leakoff ($\eta \rightarrow 0$) approximation is

$$L(t) = \frac{q_i t^{1/2}}{2\pi C_L h_f} \quad (6B-3)$$

$$w_w = 4 \left[\frac{\mu q_i^2}{\pi^3 E' C_L h_f} \right]^{1/4} t^{1/8}. \quad (6B-4)$$

Equation 6B-3 could also be obtained from the approximation in Sidebar 6A, with the fracture width set to zero and $2\sqrt{2t}$ replaced by $\pi\sqrt{t}$, which is more correct. Once the width is determined from Eq. 6B-2 or 6B-4, the pressure can be found from Eq. 6-7.

- Derivation of the Khristianovich–Geertsma–de Klerk model

Khristianovich and Zheltov (1955) derived a solution for the propagation of a hydraulic fracture by assuming the width of the crack at any distance from the well is independent of vertical position (i.e., a rectangular cross section with slip at the upper and lower boundaries), which is a reasonable assumption for a fracture with a height much greater than its length. Their solution includes the fracture mechanics aspects of the fracture tip. They recognized that to solve this problem analytically it was necessary to simplify the solution. They did this by assuming that the flow rate in the fracture is constant and that the pressure in the fracture could be approximated by a constant pressure in the majority of the fracture body, except for a small region near the tip with no fluid penetration, and hence no fluid pressure. This assumption can be made because the pressure gradient caused by fluid flow is highly sensitive to fracture width and therefore occurs primarily in the tip region. The concept of fluid lag remains an important element of the mechanics of the fracture tip and has been validated at the field scale (Warpinski, 1985). They showed that provided this dry region is quite small (a few percent of the total length), the pressure in the main body of the fracture is nearly equal to the pressure at the well over most of the length, with a sharp decrease near the tip.

Using Khristianovich and Zheltov's result that the tip region is very small, Geertsma and de Klerk (1969) gave a much simpler solution to the same problem. Their derivation is outlined in the following.

For a rectangular cross section, the equivalent of Eq. 6-9 is

$$\frac{\partial p}{\partial x} = -\frac{12q\mu}{h_f w^3}, \quad (6-25)$$

which can be written in integral form as

$$p_{net} = \frac{6\mu q_i}{h_f} \int_0^L \frac{dx}{w^3}. \quad (6-26)$$

It can be shown that applying Barenblatt's tip condition (which requires that the fracture tip must close smoothly, as illustrated in Fig. 6-3) implies that the stress intensity factor (see Chapter 3) is zero:

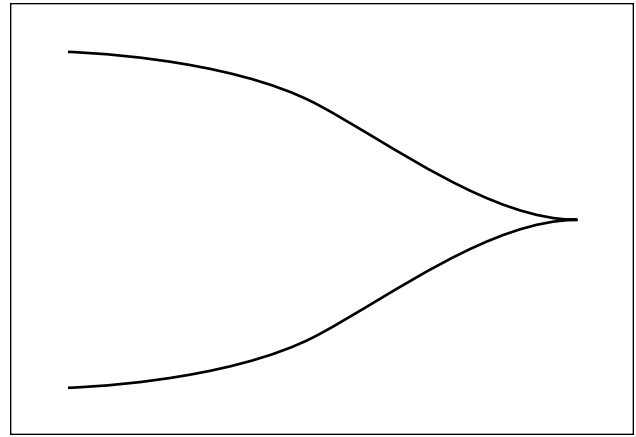


Figure 6-3. Barenblatt's tip condition.

$$\int_0^L \frac{p_{net}(x)dx}{\sqrt{1-(x/L)^2}} = 0. \quad (6-27)$$

The width profile with a small unpressured tip region is close to that obtained for a constant net pressure over the entire fracture, which is equivalent to Eq. 6-7 with h_f replaced by $2L$:

$$w_w = \frac{4}{E'} L p_{net}. \quad (6-28)$$

Solving Eqs. 6-26 through 6-28, they found expressions of the form given by Perkins and Kern (1961):

$$p_{net,w} \approx \left[\frac{21\mu q_i}{64\pi h_f L^2} E'^3 \right]^{1/4}, \quad (6-29)$$

with the wellbore width given by

$$w_w = \left[\frac{84 \mu q_i L^2}{\pi E' h_f} \right]^{1/4}. \quad (6-30)$$

For no leakoff, the equations can be solved for length and width, respectively:

$$L(t) = 0.38 \left[\frac{E' q_i^3}{\mu h_f^3} \right]^{1/6} t^{2/3} \quad (6-31)$$

$$w_w = 1.48 \left[\frac{\mu q_i^3}{E' h_f^3} \right]^{1/6} t^{1/3}. \quad (6-32)$$

The high-leakoff solution for the PKN model (Eq. 6B-3) also applies to the KGD model, but Geertsma and de Klerk did not provide an explicit width relationship for the KGD model in the case of high leakoff.

Geertsma and de Klerk also extended the model to include fluid leakoff, following Carter's (1957) method. Fluid loss is incorporated by assuming that it has no effect on fracture shape or pressure distribution. The volume of a two-wing KGD fracture is

$$V_f = \frac{\pi}{2} h_f L w_w. \quad (6-33)$$

Performing a volume balance and solution procedure similar to that of Carter, they obtained

$$L = \frac{q_i w_w}{64 C_L^2 h_f} \left(e^{s^2} \operatorname{erfc}(S) + \frac{2}{\sqrt{\pi}} S - 1 \right), \quad (6-34)$$

where

$$S = \frac{8 C_L \sqrt{\pi t}}{\pi w_w}. \quad (6-35)$$

To include the effects of spurt loss S_p , w_w should be replaced by $w_w + (8/\pi)S_p$, which is equivalent to the Carter relation with w replaced by $\bar{w} + 2S_p$ and $\bar{w} = \pi w/4$.

- Assumptions of the PKN and KGD models

Both the PKN and KGD models contain a number of assumptions that are revisited in this section. They assume that the fracture is planar (i.e., that it propagates in a particular direction, perpendicular to the minimum stress, as described in Chapter 3). They also assume that fluid flow is one-dimensional (1D) along the length of the fracture. In the case of the models described, they assume Newtonian fluids (although Perkins and Kern also provided solutions for power law fluids), and leakoff behavior is governed by a simple expression derived from filtration theory (Eq. 6-14). The rock in which the fracture propagates is assumed to be a continuous, homogeneous, isotropic linear elastic solid; the fracture is considered to be of fixed height or completely confined in a given layer; and one of two assumptions is made concerning the length to height ratio of the fracture—i.e., height is large (KGD) or small (PKN) relative to length. Finally, the KGD model includes the assumption that tip processes dominate fracture propagation, whereas the PKN model neglects fracture mechanics altogether.

Since these models were developed, numerous extensions have been made that relax these assumptions, the most important of which are the solutions for power law fluids. These two models

are still used to design treatments and are usually available as options in simulators.

Similar solutions can be derived for radial fractures (see Sidebar 6C).

6C. Radial fracture geometry models

Both Perkins and Kern (1961) and Geertsma and de Klerk (1969) considered radial fractures, which grow unconfined from a point source. This model is applicable when there are no barriers constraining height growth or when a horizontal fracture is created.

Geertsma and de Klerk formulated the radial model using the same arguments outlined in "Derivation of the Khristianovich-Geertsma-de Klerk model" (page 6-7). The fracture width is

$$w_w = 2.56 \left[\frac{\mu q_i R}{E'} \right]^{1/4} \quad (6C-1)$$

and the radial length R is

$$R = \sqrt{\frac{q_i (4w_w + 15S_p)}{30\pi^2 C_L^2} \left(e^{s^2} \operatorname{erfc}(S) + \frac{2}{\sqrt{\pi}} S - 1 \right)}, \quad (6C-2)$$

where

$$S = \frac{15 C_L \sqrt{\pi t}}{4w_w + 15S_p}. \quad (6C-3)$$

An explicit relationship for pressure can be derived by considering the solution for flow from a point source, in which case the pressure in the fracture is a function of the expression $\ln(r_w/R)$, where r_w is the radius of the wellbore.

The no-fluid-loss approximations for the radial model are

$$w_w = 2.17 \left[\frac{\mu^2 q_i^3}{E'^2} \right]^{1/9} t^{1/9} \quad (6C-4)$$

$$R = 0.52 \left[\frac{E' q_i^3}{\mu} \right]^{1/9} t^{4/9}. \quad (6C-5)$$

The large-fluid-loss approximation for radial length is

$$R = \frac{1}{\pi} \left[\frac{q_i^2 t}{C_L^2} \right]^{1/4}. \quad (6C-6)$$

An expression for width in the case of large fluid loss was not provided but can be found from Eqs. 6C-1 and 6C-6.

6-3. Three-dimensional and pseudo-three-dimensional models

The simple models discussed in the previous sections are limited because they require the engineer to specify the fracture height or to assume that a radial fracture will develop. This is a significant limitation, because it is not always obvious from logs and other

data where or whether the fracture will be contained. Also, the fracture height usually varies from the well (where the pressure is highest) to the tip of the fracture. This limitation can be remedied by the use of planar 3D and pseudo-3D (P3D) models.

The three major types of hydraulic fracture models that include height growth are categorized according to their major assumptions.

- General 3D models make no assumptions about the orientation of the fracture. Factors such as the wellbore orientation or perforation pattern may cause the fracture to initiate in a particular direction before turning into a final preferred orientation (perpendicular to the far-field minimum in-situ stress). Simulators incorporating such models are computationally intensive and generally require a specialist to obtain and interpret the results. They are most applicable in research environments, for which they are used for studying details of fracture initiation and near-well complexities such as those discussed in Section 6-8, rather than overall fracture growth. One example of such a study was published by Brady *et al.* (1993). These models are not discussed further in this volume.
- Planar 3D models are based on the assumption that the fracture is planar and oriented perpendicular to the far-field minimum in-situ stress. No attempt is made to account for complexities that result in deviations from this planar behavior. Simulators based on such models are also computationally demanding, so they are generally not used for routine designs. They should be used where a significant portion of the fracture volume is outside the zone where the fracture initiates or where there is more vertical than horizontal fluid flow. Such cases typically arise when the stress in the layers around the pay zone is similar to or lower than that within the pay. This type of model is described in more detail in Section 6-3.1.
- P3D models attempt to capture the significant behavior of planar models without the computational complexity. The two main types are referred to here as “lumped” and cell-based. In the lumped (or elliptical) models, the vertical profile of the fracture is assumed to consist of two half-ellipses joined at the center, as shown in Fig. 6-4. The horizontal length and wellbore vertical tip extensions are calculated at each time step, and the assumed shape is matched to these positions. These models make the

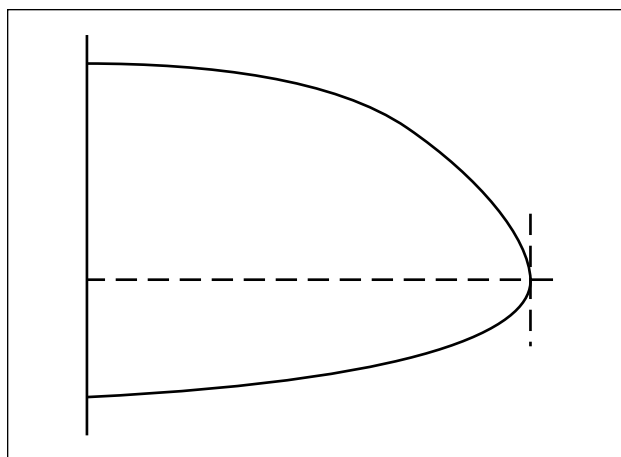


Figure 6-4. Conceptual representation of the lumped model.

inherent assumptions that fluid flow is along streamlines from the perforations to the edge of the ellipse and that the streamlines have a particular shape, derived from simple analytical solutions. Cell-based models treat the fracture as a series of connected cells. They do not prescribe a fracture shape, but generally assume plane strain (i.e., each cell acts independently) and do not fully couple the calculation of fluid flow in the vertical direction to the fracture geometry calculation.

In the fixed-height models described previously, no consideration is given to the layers surrounding the fractured zone. The planar and P3D models use data about the properties of the surrounding zones to predict the rate of growth into these zones. For the purpose of this chapter, planar 3D models are defined as those in which calculation of the full 2D fluid-flow field in the fracture is coupled to the 3D elastic response of the rock, and P3D models are defined as those that approximate either the coupling or the 3D elasticity in some manner.

Regardless of which type of model is used to calculate the fracture geometry, only limited data are available on typical treatments to validate the model used. For commercial treatments, the pressure history during treatment is usually the only data available to validate the model. Even in these cases, the quality of the data is questionable if the bottomhole pressure must be inferred from the surface pressure. The bottomhole pressure is also not sufficient to uniquely determine the fracture geometry in the absence of other information, such as that derived from tiltmeters and microseismic data (see Sidebar 6D). If a simulator incorporates the correct model, it should match both

6D. Field determination of fracture geometry

Fracture geometry can be determined by using the two techniques of microseismic activity and tiltmeters. Microseisms can be used to locate the fracture, thus providing estimates of its length and height, whereas tiltmeters can provide information about fracture width.

Microseisms

Although all models of hydraulic fracturing assume that the rock is a continuous medium, it is well known that reservoirs have natural fractures, bedding planes and other weakness features that respond as a noncontinuum. Such features have been used to image hydraulic fractures using seismic techniques.

Hydraulic fractures induce two large changes in the reservoir as they are created. The stress in the surrounding rock is perturbed because of fracture opening, and the pore pressure is increased as a result of leakoff of the high-pressure fracturing fluid. Both of these features can result in the generation of large shear stresses on many of the weakness planes near the hydraulic fracture, resulting in small shear slippages called microseisms or microearthquakes.

Microseisms generate seismic waves that can be detected by sensitive seismic receivers in nearby wells. As shown in Fig. 6D-1, both compressional waves (*P*-waves) and shear waves (*S*-waves) can be generated by the microseism, and these two waves travel with different velocities. If a receiver can detect both the *P*- and *S*-waves, the time separation can be determined and the distance to the source inferred from

$$d = \frac{u_p u_s}{u_p - u_s} [t_s - t_p], \quad (6D-1)$$

where u_p and u_s are the compressional and shear velocities, respectively, and t_s and t_p are the shear and compressional arrival times.

The direction in space can be determined by using a triaxial receiver to examine the amplitude of the *P*-wave. The *P*-wave has the characteristic that its particle motion (how the rock mass vibrates) is aligned with the direction of travel of the wave. By obtaining the orientation of the resultant amplitude vector at any time, the microseism can be traced back to its source.

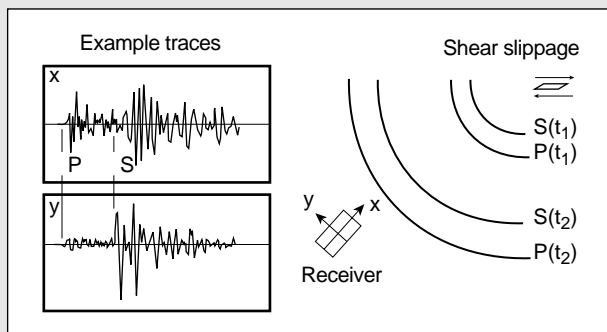


Figure 6D-1. Microseismic traces at the receiver resulting from shear slippage.

With multiple seismic receivers, triangulation techniques can be employed and greater accuracy obtained. With either approach, however, the objective is to locate the zone of microseisms surrounding the hydraulic fracture and deduce the size and shape of the fracture from this information.

Downhole tiltmeters

Width development in a hydraulic fracture results in elastic deformation of the formation. This deformation can be used for fracture diagnostics to provide significant information about fracture height and width and also about formation characteristics.

As a fracture is opened, the deformation of the rock extends for large distances into the reservoir. Although the deformation is small at distances of more than a few tens of feet, highly sensitive tiltmeter devices can measure these small changes in position. A tiltmeter does not actually measure the displacement of the earth, but rather the curvature of the displacement, and it is capable of measuring up to nanoradian resolution (a nanoradian is the angle induced by stretching a line from New York to Los Angeles and raising the New York side by the diameter of a pencil). Tiltmeters have long been used for surface diagnostics of earth movement, but the application of a string of downhole tiltmeters provides highly sensitive fracture data.

Figure 6D-2 shows a schematic of the tilt response of the formation measured in a well offset to the fracture treatment. The characteristic S-shaped curve is typical of tilt, as opposed to strain, and can be simply explained. Straight across from the fracture, the rock is pushed away, but is not tilted on the geometric axis of the fracture, and there is zero tilt. Above the fracture, the earth experiences curvature that is defined as negative for this example. The curvature reaches a maximum at a well-defined point and then decreases to zero as the distance from the fracture increases. The bottom is identical to the top, except that the curvature has the opposite direction and opposite sign.

Two aspects of this distribution are important for diagnostics. First, the locations of the maximum tilt values are a function of the height h_f of the fracture relative to the distance d away. Thus, fracture height can be quickly estimated. Second, the amplitude of the tilt is a function of the width of the fracture, so the width during fracturing, and possibly the final propped width, can be estimated as well.

Branagan *et al.* (1996) provided an example of the application of tiltmeters to the calculation of hydraulic fracture geometry.

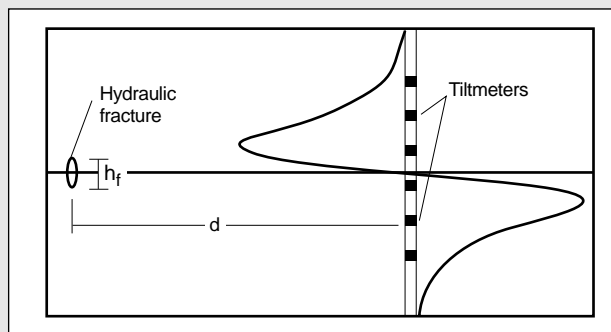


Figure 6D-2. Tiltmeter response to hydraulic fracture width.

treating pressure and fracture geometry. These issues are addressed in Section 6-12 and Chapter 9.

6-3.1. Planar three-dimensional models

A planar fracture is a narrow channel of variable width through which fluid flows. The fracture geometry is defined by its width and the shape of its periphery (i.e., height at any distance from the well and length). Both the width at any point and the overall shape vary with time. They depend on the pressure distribution, which itself is determined by the pressure gradients caused by the fluid flow within the fracture. Because the relation between pressure gradient and flow rate is highly sensitive to the fracture width (Eq. 6-9), the geometry and fluid flow are tightly coupled. Although the mechanics of these processes are described separately in this section, the complexity of solving any fracture model lies in the close coupling between the different processes. Three separate problems are considered:

- width profile in a fracture of known shape and pressure distribution
- shape of the fracture
- flow of fluid in a fracture of known shape and width (i.e., known geometry).

Hirth and Lothe (1968) and Bui (1977) showed how the pressure and width in a fracture may be related. Basically, the width at any point (x,y) is determined by an integral of the net pressure over the entire fracture, expressed as

$$w(x,y) = \iint_S f(x-x', y-y')(p(x',y') - \sigma(x',y')) dx' dy', \quad (6-36)$$

where σ is the stress.

The details of the elastic influence function f in Eq. 6-36 are beyond the scope of this volume. Useable forms of Eq. 6-36 can be derived generally only for homogeneous linear elastic materials (see Sidebar 6E). In fracturing applications, the rock is usually also assumed to be isotropic.

The shape of the fracture evolves with time. In essence, the boundary (i.e., the vertical and horizontal tips) moves outward as the fluid provides sufficient energy to fracture the rock at the boundary. More complex tip behavior is discussed subsequently, but in this

section it is assumed that this process is described by linear elastic fracture mechanics (LEFM). If the LEFM failure criterion is exceeded at any point on the fracture periphery, the fracture will extend until the criterion is again met. For simple shapes and pressure distributions, such as ellipses under constant pressure, the criterion can be specified analytically, similar to Eq. 6-3. For more complex shapes and pressure distributions, analytical solutions are not available. In these cases, it can be shown that a relatively simple criterion can be written in terms of the width near the tip and the critical stress intensity factor or fracture toughness K_{Ic} , which is introduced in Chapter 3:

$$w(x) = \frac{4\sqrt{2}K_{Ic}}{\sqrt{\pi E'}} \sqrt{x}, \quad (6-37)$$

where x is the distance measured from the tip. Relations between fracture mechanics parameters such as the specific surface energy (used in Eq. 6-3) and the fracture toughness are provided in Chapter 3.

The fluid flow is described by equations for conservation of mass (a general form of Eq. 6-21, including the density ρ and expressed in terms of velocity u):

$$\left(\frac{\partial(\rho w u_x)}{\partial x} + \frac{\partial(\rho w u_y)}{\partial y} \right) + \frac{\partial}{\partial t}(\rho w) + 2\rho u_L = 0, \quad (6-38)$$

which can be written as a vector equation:

$$\nabla \cdot (\rho w \bar{u}) + \frac{\partial}{\partial t}(\rho w) + 2\rho u_L = 0, \quad (6-39)$$

and the conservation of momentum (a general form of Eq. 6-9) is

$$\rho \frac{D\bar{u}}{Dt} = -\nabla p - [\nabla \cdot \tau] + \rho \bar{g}, \quad (6-40)$$

where τ is the shear stress and \bar{g} is the acceleration of gravity.

The first two terms in Eq. 6-38 relate to the spatial change of the mass-flow vector, and the second two terms represent the storage resulting from width increases and leakoff, respectively. Equation 6-40 is a vector equation. The term on the left-hand side is the rate of change of momentum, and the terms on the right-hand side are the pressure, viscous and gravitational forces, respectively. It simply states that a small element of fluid accelerates because of the forces acting on it. This equation can be expanded and then simplified for the geometries of interest in hydraulic frac-

6E. Lateral coupling in pseudo-three-dimensional models

Assume that a fracture has a fixed height and that it consists of a number of elements each of constant width over the height (i.e., a KGD fracture). Let the grid points be represented by points x_i in the center of the elements with corners $(x_{l,i}, y_{b,i})$, $(x_{r,i}, y_{t,i})$ and $(x_{r,k}, y_{b,k})$, as shown in Fig. 6E-1. Crouch and Starfield (1983) developed a boundary element solution technique called the displacement discontinuity method. They showed that the pressure at any point is given by

$$p(x_i) = \sum_k A_{ik} w_k, \quad (6E-1)$$

where A_{ik} is an influence function of the form

$$A_{ik} = \frac{G}{4\pi(1-\nu)} I(x_{c,i}, y_{c,i}; x_{l,k}; x_{r,k}, y_{b,k}, y_{t,k}), \quad (6E-2)$$

where the influence function I is defined as

$$I = \frac{[(x_{c,i} - x_{r,k})^2 + (y_{c,i} - y_{t,k})^2]^{1/2}}{(x_{c,i} - x_{r,k})(y_{c,i} - y_{t,k})} - \frac{[(x_{c,i} + x_{l,k})^2 + (y_{c,i} - y_{t,k})^2]^{1/2}}{(x_{c,i} + x_{l,k})(y_{c,i} - y_{t,k})} + \frac{[(x_{c,i} + x_{l,k})^2 + (y_{c,i} + y_{b,k})^2]^{1/2}}{(x_{c,i} + x_{l,k})(y_{c,i} + y_{b,k})} - \frac{[(x_{c,i} - x_{r,k})^2 + (y_{c,i} + y_{b,k})^2]^{1/2}}{(x_{c,i} - x_{r,k})(y_{c,i} + y_{b,k})}. \quad (6E-3)$$

To accurately solve Eq. 6E-1 requires a large number of elements. Also, it is difficult to extend directly to other shapes such as ellipses or for nonconstant heights. To overcome these problems, the equation is modified as follows. The width at any point can be written as

$$w(x_k) = w(x_i) + \Delta w_{ki}, \quad (6E-4)$$

where Δw_{ki} is defined as

$$\Delta w_{ki} = w(x_k) - w(x_i). \quad (6E-5)$$

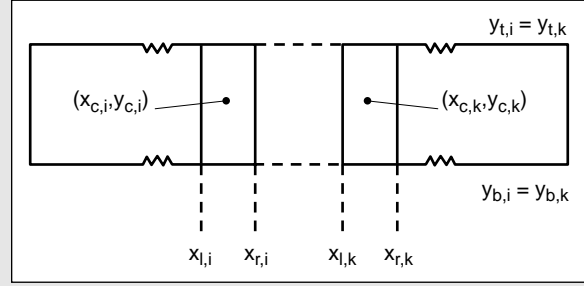


Figure 6E-1. Geometry for displacement continuity solution.

Equation 6E-1 can then be written as

$$p(x_i) = p(w_i) + p_{corr}, \quad (6E-6)$$

where

$$p(w_i) = w(x_i) \sum A_{ik} \quad (6E-7)$$

$$p_{corr} = \sum A_{ik} \Delta w_{ki}. \quad (6E-8)$$

The term $w(x_i) \sum A_{ik}$ thus represents the pressure induced by a fracture of constant width $w(x_i)$. For a fracture of infinite length, this pressure would be exact if calculated using the plane strain solution. The term $p(w)$ can therefore be obtained as the sum of the plane strain solution and the effect of two semi-infinite fractures of $w - w_i$ attached at the tip of each fracture wing.

From Eq. 6E-2, the influence functions decrease with distance from an element. The advantages of the form of Eq. 6E-8 are that the corrections are smallest near the element where the widths are almost the same and that the self-correction is exactly zero by definition. The number of elements required to obtain an accurate solution is significantly reduced, and variable heights and other shapes are easily introduced. Lateral coupling is relatively easy to introduce to the explicit solution method because the pressure correction is simply added before the fluid velocities are calculated.

turing (see Sidebar 6F). For a particular component, such as the x component, Eq. 6-40 can be written as

$$\rho \frac{Du_x}{Dt} = -\frac{\partial p}{\partial x} - \left(\frac{\partial \tau_{xx}}{\partial x} + \frac{\partial \tau_{yx}}{\partial y} + \frac{\partial \tau_{zx}}{\partial z} \right) + \rho g_x. \quad (6-41)$$

A constitutive law relating the stresses τ to the flow rate is required to complete the description of fluid flow. In the case of steady flow in a narrow channel such as a fracture, the full details of the constitutive law are not required, because the narrow fracture width results in the complete dominance of some stress terms. The only terms of interest are the shear stresses induced by velocity gradients across the fracture. In addition, use is made of the lubrication approximation, so flow perpendicular to the fracture wall (the z direction) is neglected. With these assump-

tions, the equations for the stress in a Newtonian fluid reduce to

$$\begin{aligned} \tau_{xz} &= \tau_{zx} = -\mu \left(\frac{\partial u_x}{\partial z} \right) \\ \tau_{yz} &= \tau_{zy} = -\mu \left(\frac{\partial u_y}{\partial z} \right), \end{aligned} \quad (6-42)$$

and Eq. 6-41 can be written as

$$\rho \frac{Du_x}{Dt} = -\frac{\partial p}{\partial x} + \mu \left(\frac{\partial^2 u_x}{\partial z^2} \right) + \rho g_x. \quad (6-43)$$

For the special case of a narrow channel (Poiseuille flow), where velocity gradients parallel to the flow are small and there is no flow perpendicular to the channel, the time-dependent term simplifies to a partial

6F. Momentum conservation equation for hydraulic fracturing

Equation 6-40 is a vector equation, for which a component can be written as

$$\rho \frac{Du_i}{Dt} = -\frac{\partial p}{\partial x_i} - \left(\frac{\partial \tau_{xi}}{\partial x} + \frac{\partial \tau_{yi}}{\partial y} + \frac{\partial \tau_{zi}}{\partial z} \right) + \rho g_i, \quad (6F-1)$$

where u is the velocity, g is the gravitational acceleration, and i is x , y or z . The term on the left side of Eq. 6F-1 is termed the substantial derivative, which is the rate of change seen by an observer moving with the fluid motion. It can be related to the usual partial derivative (i.e., the rate of change seen by a stationary observer) as

$$\frac{D}{Dt} = \frac{\partial}{\partial t} + u_x \frac{\partial}{\partial x} + u_y \frac{\partial}{\partial y} + u_z \frac{\partial}{\partial z}. \quad (6F-2)$$

Thus, Eq. 6F-2 can be expanded to

$$\begin{aligned} & \rho \left(\frac{\partial u_i}{\partial t} + u_x \frac{\partial u_i}{\partial x} + u_y \frac{\partial u_i}{\partial y} + u_z \frac{\partial u_i}{\partial z} \right) \\ &= -\frac{\partial p}{\partial x_i} - \left(\frac{\partial \tau_{xi}}{\partial x} + \frac{\partial \tau_{yi}}{\partial y} + \frac{\partial \tau_{zi}}{\partial z} \right) + \rho g_i. \end{aligned} \quad (6F-3)$$

This completely general equation can be simplified for a narrow channel in an impermeable medium. Leakoff does not occur in this case, so components in the z direction can be neglected. In addition, the flow is assumed to be steady state, so time derivatives can be ignored. In this case, Eq. 6F-3 simplifies to

$$\begin{aligned} & \rho \left(u_x \frac{\partial u_i}{\partial x} + u_y \frac{\partial u_i}{\partial y} \right) \\ &= -\frac{\partial p}{\partial x_i} - \left(\frac{\partial \tau_{xi}}{\partial x} + \frac{\partial \tau_{yi}}{\partial y} + \frac{\partial \tau_{zi}}{\partial z} \right) + \rho g_i, \end{aligned} \quad (6F-4)$$

for $i = 1$ or 2 . Even for a permeable medium, Eq. 6F-4 is used. In this case, leakoff is treated as a sink term and included in the mass balance, but it is assumed not to affect the equations relating pressure, stress and fluid velocity.

Newtonian fluids

To make Eq. 6F-4 useful, the stress components must be determined, which is done by assuming a model of fluid behavior. For example, a Newtonian fluid is a model with one parameter, the viscosity μ . The stress components are

$$\begin{aligned} \tau_{xx} &= \mu \frac{\partial u_x}{\partial x} + \frac{2}{3} \mu (\nabla \cdot u) \\ \tau_{yy} &= 2\mu \frac{\partial u_y}{\partial y} + \frac{2}{3} \mu (\nabla \cdot u) \\ \tau_{zz} &= 2\mu \frac{\partial u_z}{\partial z} + \frac{2}{3} \mu (\nabla \cdot u) \\ \tau_{xy} = \tau_{yx} &= -\mu \left(\frac{\partial u_x}{\partial y} + \frac{\partial u_y}{\partial x} \right) \\ \tau_{yz} = \tau_{zy} &= -\mu \left(\frac{\partial u_y}{\partial z} + \frac{\partial u_z}{\partial y} \right) \\ \tau_{zx} = \tau_{xz} &= -\mu \left(\frac{\partial u_z}{\partial x} + \frac{\partial u_x}{\partial z} \right). \end{aligned} \quad (6F-5)$$

The first three components of Eq. 6F-5 are the normal stresses, and the last three are the shear stresses. The last term of the normal components is zero for incompressible fluids. In the case of 1D flow between parallel plates, without leakoff, two of the velocity components are identically zero. In addition, conservation of mass implies that the third component cannot vary with position. Hence, all three normal components are identically zero. The equations thus reduce to those for shear flow. Although these assumptions are not strictly true in general, they are used for the flow calculations in hydraulic fracture modeling. It can also be shown that for a narrow channel, the velocity gradients perpendicular to the walls (the z direction) are much greater than those in the parallel directions. Finally, therefore, the stress components for a Newtonian fluid in a hydraulic fracture can be written as

$$\begin{aligned} \tau_{zx} &= -\mu \left(\frac{\partial u_x}{\partial z} \right) \\ \tau_{zy} &= -\mu \left(\frac{\partial u_y}{\partial z} \right). \end{aligned} \quad (6F-6)$$

Substituting Eq. 6F-6 into Eq. 6F-4 obtains

$$\begin{aligned} \rho \left(u_x \frac{\partial u_x}{\partial x} + u_y \frac{\partial u_x}{\partial y} \right) &= -\frac{\partial p}{\partial x} + \mu \frac{\partial^2 u_x}{\partial z^2} \\ \rho \left(u_x \frac{\partial u_y}{\partial x} + u_y \frac{\partial u_y}{\partial y} \right) &= -\frac{\partial p}{\partial y} + \mu \frac{\partial^2 u_y}{\partial z^2} + \rho g. \end{aligned} \quad (6F-7)$$

For 1D flow along the fracture length, as typically assumed in P3D models, Eq. 6F-7 can be simplified to

$$\frac{\partial^2 u_x}{\partial z^2} = \frac{1}{\mu} \frac{\partial p}{\partial x}. \quad (6F-8)$$

Assuming zero slip (i.e., zero velocity at the fracture wall), the solution to Eq. 6F-8 is

$$u_x = \frac{1}{2\mu} \frac{\partial p}{\partial x} \left(z^2 - (w/2)^2 \right). \quad (6F-9)$$

Integrating to obtain the average velocity across the channel,

$$\bar{u}_x = \frac{-w^2}{12\mu} \frac{\partial p}{\partial x}. \quad (6F-10)$$

The flow rate per unit height is obtained by multiplying the average velocity by the width w .

In the case of 2D flow, the left-hand sides of Eq. 6F-7 are zero if inertia may be neglected. In this case for the y direction, an equation can be formed similar to Eq. 6F-10, except that it includes a gravitational term.

derivative of velocity with respect to time. It is usually assumed that the flow is steady state, which finally obtains

$$\frac{\partial p}{\partial x} = \mu \left(\frac{\partial^2 u_x}{\partial z^2} \right) + \rho g_x \quad (6-44)$$

and a similar equation for the y component.

Equations 6-36 through 6-44 summarize the planar 3D model for Newtonian fluids. Similar results can be obtained for non-Newtonian fluids (see Sidebar 6G). These equations are generally not amenable to analytic solutions, but require a numerical simulation. In addition, although it is relatively straightforward to write the conceptual equations, efficient and robust numerical solutions are difficult to obtain. The primary reasons for this difficulty are the extremely close coupling of the different parts of the solution (e.g., fluid flow and solid deformation), the nonlinear relation between width and pressure, and the complexity of a moving-boundary problem.

The first numerical implementation of a planar model was reported by Clifton and Abou-Sayed (1979). In essence, their approach was to define

a small fracture, initiated at the perforations, divide it into a number of equal elements (typically 16 squares) and then begin solution of the equations. As the boundary extends, the elements distort to fit the new shape. One difficulty with such a solution is that the elements can develop large aspect ratios and very small angles, as shown in Fig. 6-5. The numerical schemes typically used to solve the equations do not usually perform well with such shapes.

A different formulation was described by Barree (1983), and numerous field applications have been reported (e.g., Barree, 1991). It neatly avoids the problem of grid distortion by dividing the layered reservoir into a grid of equal-size rectangular elements, which are defined over the entire region that the fracture may cover. In this case, the grid does not move. Instead, as the failure criterion is exceeded, the elements ahead of the failed tip are opened to flow and become part of the fracture, as shown in Fig. 6-6. Two limitations of this approach are that

- the number of elements in the simulation increases as the simulation proceeds, so that the initial number may be small, resulting in inaccuracy

6G. Momentum balance and constitutive equation for non-Newtonian fluids

The definition of a Newtonian fluid is the one-parameter relation between stress and velocity (Eq. 6G-5). In tensor notation, this can be written as

$$\tau_{ij} = -\mu \Delta_{ij}, \quad (6G-1)$$

where Δ is the rate of deformation tensor, with components

$$\Delta_{ij} = \frac{\partial u_i}{\partial x_j} + \frac{\partial u_j}{\partial x_i}. \quad (6G-2)$$

The viscosity may be a function of pressure and temperature or other variables, including the history of the fluid, but not of Δ . For non-Newtonian fluids, an equation similar to Eq. 6G-1 may be written:

$$\tau_{ij} = -\mu_a \Delta_{ij}, \quad (6G-3)$$

where μ_a is a function of Δ . For flows of the type of interest in fracturing, it can be shown that μ_a may depend only on Δ through a relation of the form

$$\mu_a = \mu_a(I_2), \quad (6G-4)$$

where I_2 is the second tensor invariant:

$$I_2 = \sum_i \sum_j \Delta_{ij} \Delta_{ji}. \quad (6G-5)$$

For example, for a power law fluid, the function μ_a is

$$\mu_a = K \left| \frac{I_2}{2} \right|^{n-1} \quad (6G-6)$$

and for a Bingham plastic

$$\mu_a = \mu_0 + \frac{\tau_0}{\sqrt{\frac{|I_2|}{2}}}. \quad (6G-7)$$

The commonly used consistency index K' is dependent on the flow geometry and is related to a basic fluid property, the generalized consistency index K (Eq. 6G-6). For parallel plates (i.e., in a slot), which can represent a fracture, the relationship is

$$K' = K \left(\frac{2n+1}{3n} \right)^n. \quad (6G-8)$$

For a pipe it is

$$K' = K \left(\frac{3n+1}{4n} \right)^n. \quad (6G-9)$$

The maximum difference between the two expressions is less than 4% for all values of n . For 1D flow of a power law fluid between parallel plates, the average fluid velocity is given by

$$\bar{u}_x = \left(\frac{1}{K} \right)^{1/n} \left(\frac{\partial p}{\partial x} \right)^{1/n} \frac{n}{1+2n} \left(\frac{w}{2} \right)^{\frac{1+n}{n}}. \quad (6G-10)$$

For the special case of the power law exponent $n = 1$, this reverts to the equation for a Newtonian fluid, with K' replaced by the viscosity. Table 6G-1 summarizes useful information for the laminar flow of both Newtonian and power law fluids under different geometries. However, the expressions for pressure drop are not generally applicable for drag-reducing fluids such as those used in hydraulic fracturing.

6G. Momentum balance and constitutive equation for non-Newtonian fluids (continued)

Table 6G-1. Summarized expressions for laminar flow of Newtonian and power law fluids.				
	Fluid Type	Pipe	Parallel Plates	Ellipse (zero eccentricity)
Reynold's number (N_{Re})	Newtonian	$\frac{\rho u D}{\mu}$	$\frac{2\rho u w}{\mu}$	$\frac{\pi\rho u w}{2\mu}$
	Power law	$\frac{8^{1-n}\rho D^n u^{2-n}}{K'_p}$	$\frac{3^{1-n}2^{2-n}\rho u^{2-n}w^n}{K'_{pp}}$	$\frac{\pi^{2-n}\rho u^{2-n}w^n}{2^n K'_{ell}}$
Hydraulic diameter (D_H) Friction factor $\left(f = \left(\frac{D_H}{4L}\Delta p\right) / \left(\frac{1}{2}\rho u^2\right)\right)$		D $16/N_{Re}$	$2w$ $24/N_{Re}$	$\pi w/2$ $2\pi^2/N_{Re}$
Velocity distribution	Newtonian	$u_r = 2u\left[1 - \left(\frac{2r}{D}\right)^2\right]$	$u_x = \frac{3u}{2}\left[1 - \left(\frac{2y}{w}\right)^2\right]$	$u_x = 2u\left[1 - \left(\frac{2y}{w}\right)^2 - \left(\frac{2z}{h}\right)^2\right]$
	Power law	$u_r = \left(\frac{3n+1}{n+1}\right)u\left[1 - \left(\frac{2r}{D}\right)^{\frac{n+1}{n}}\right]$	$u_x = \left(\frac{2n+1}{n+1}\right)u\left[1 - \left(\frac{2y}{w}\right)^{\frac{n+1}{n}}\right]$	
Pressure drop ($\Delta p/L$ or dp/dx)	Newtonian	$\frac{128\mu q}{\pi D^4}$	$\frac{12\mu q}{h,w^3}$	$\frac{64\mu q}{\pi h,w^3}$
	Power law	$\frac{2^{5n+2}q^n K}{\pi^n D^{3n+1}}$	$\left(\frac{4n+2}{n}\right)^n \frac{2q^n K}{h^n w^{2n+1}}$	See Eq. 6-57
K'		$K'_p = K\left(\frac{3n+1}{4n}\right)^n$	$K'_{pp} = K\left(\frac{2n+1}{3n}\right)^n$	-

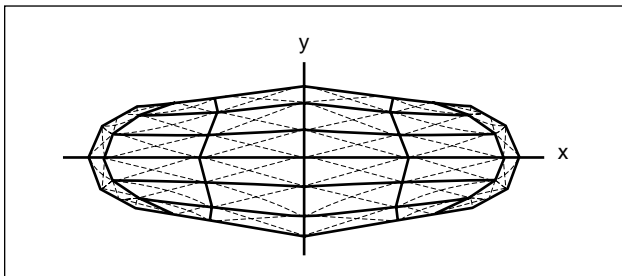


Figure 6-5. Planar 3D fracture divided into elements that were initially square.

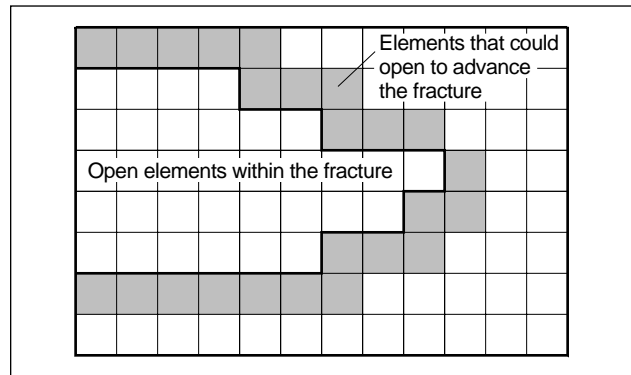


Figure 6-6. Fixed-grid solution showing elements open to advance the fracture.

- the general size of the fracture must be estimated in advance of the simulation to ensure that a “reasonable” number of elements is used.

In addition, this particular implementation has two simplifying assumptions, that a simplified method is used for representing modulus contrasts and a tensile

strength criterion is used for fracture extension, rather than a fracture mechanics effect. The failure criterion is used to compare the stress at the center of all boundary elements with the material tensile strength.

If the strength is exceeded, then the element is assumed to open. However, the fracture-induced stress in the material near the tip of a fracture varies with the square root of the distance from the tip. Hence, the failure criterion is grid-resolution dependent.

6-3.2. Cell-based pseudo-three-dimensional models

In cell-based models, the fracture length is divided into a number of discrete cells. This is directly analogous to the planar models, except that only one direction is discrete instead of two. Fluid flow is assumed to be essentially horizontal along the length of the fracture, and the solid mechanics is typically simplified by assuming plane strain at any cross section. As in the PKN model, these assumptions make these models suitable primarily for reasonably contained fractures, which are long relative to their height.

These two assumptions allow separating the solid and fracture mechanics solution from the fluid flow as follows. Plane strain implies that each cross section acts independently of any other. In addition, the assumption of 1D fluid flow implies that the pressure in the cross section is always

$$p = p_{cp} + \rho_f g y, \quad (6-45)$$

where p_{cp} is the pressure along a horizontal line through the center of the perforations and y is the vertical distance from the center of the perforations. Equation 6-45 is valid only if vertical fracture extension is sufficiently slow that the pressure gradient resulting from vertical flow can be neglected. This assumption that the vertical tips of the fracture are approximately stationary at all times is called the equilibrium-height assumption.

- Solid mechanics solution

With the equilibrium-height assumption, the solid mechanics solution simplifies to the determination of the fracture cross-sectional shape as a function of the net pressure, or p_{cp} . Simonson *et al.* (1978) derived this solution for a symmetric three-layer case. Fung *et al.* (1987) derived a more general solution for nonsymmetric multilayer cases. Following Fung *et al.* the stress intensity factors at the top and bottom tips K_{Ia} and K_{Ib} , respectively, can be written in terms of the pressure at the center of the perforations p_{cp} and the closure stresses in the layers σ_i as

$$K_{Ia} = \sqrt{\frac{\pi h_f}{2}} \left[p_{cp} - \sigma_n + \rho_f g \left(h_{cp} - \frac{3}{4} h_f \right) \right] + \sqrt{\frac{2}{\pi h_f}} \sum_{i=1}^{n-1} (\sigma_{i+1} - \sigma_i) \left[\frac{h_f}{2} \cos^{-1} \left(\frac{h_f - 2h_i}{h_f} \right) - \sqrt{h_i - (h_f - h_i)} \right] \quad (6-46)$$

$$K_{Ib} = \sqrt{\frac{\pi h_f}{2}} \left[p_{cp} - \sigma_n + \rho_f g \left(h_{cp} - \frac{1}{4} h_f \right) \right] + \sqrt{\frac{2}{\pi h_f}} \sum_{i=1}^{n-1} (\sigma_{i+1} - \sigma_i) \left[\frac{h_f}{2} \cos^{-1} \left(\frac{h_f - 2h_i}{h_f} \right) - \sqrt{h_i - (h_f - h_i)} \right], \quad (6-47)$$

where ρ_f is the fluid density, h_{cp} is the height at the center of the perforations, and h_i is the height from the bottom tip of the fracture to the top of the i th layer, as shown in Fig. 6-7.

This set of nonlinear equations can be solved by iteration. Assuming that the solution (two vertical tip positions plus the pressure) at one value of p_{cp} is known, a height increment is assumed. The incremental height growth in the two vertical directions is then calculated such that Eqs. 6-46 and 6-47 are both satisfied, and p_{cp} to obtain these positions is calculated. Finally, the width profile associated with this solution can be obtained as

$$w(y) = \frac{4}{E'} \left(p_{cp} + \rho_f g (h_{cp} - y) - \sigma_n \right) \sqrt{y(h_f - y)} + \frac{4}{\pi E'} \sum_{i=1}^{n-1} (\sigma_{i+1} - \sigma_i) \left[(h_i - y) \cosh^{-1} \left(\frac{y}{|y - h_i|} + \frac{h_f - 2h_i}{h_f} + \frac{h_i}{|y - h_i|} \right) + \sqrt{y(h_f - y)} \cos^{-1} \left(\frac{h_f - 2h_i}{h_f} \right) \right], \quad (6-48)$$

where y is the elevation measured from the bottom tip of the fracture.

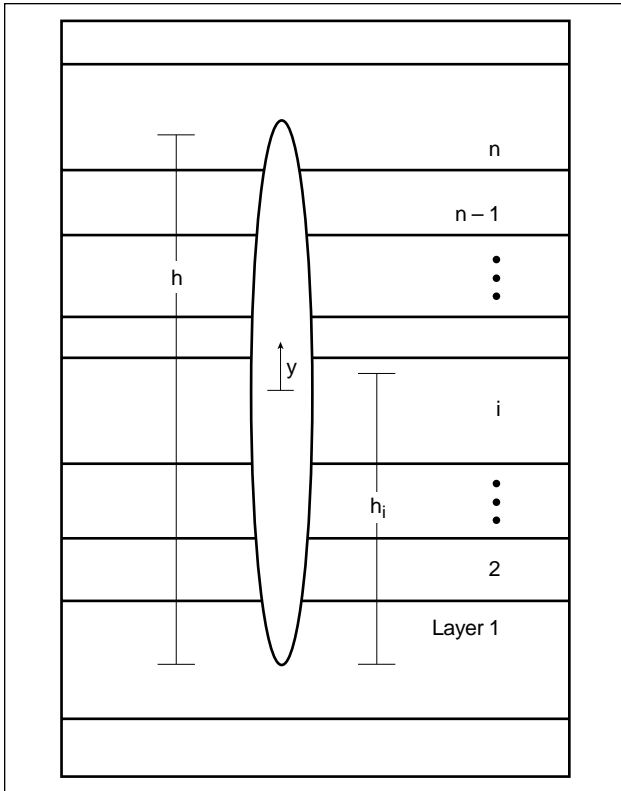


Figure 6-7. Definition of variables for the fracture containment problem.

Consider, for example, the symmetric three-layer case shown in Fig. 6-8. If the gravitational component is neglected, so that the problem is symmetric, then the penetrations into the two barriers are equal. In this case, Eq. 6-46 can be simplified significantly and written as (Simonson *et al.*, 1978)

$$K_{lu} = K_{ll} = \sqrt{\frac{\pi h_f}{2} \left[p_{cp} - \sigma_{pay} - \frac{2\Delta\sigma}{\pi} \cos^{-1} \left(\frac{h_{pay}}{h_f} \right) \right]}, \quad (6-49)$$

where $\Delta\sigma$ is the difference in stress between the central layer (pay zone) and the surrounding layers, and h_{pay} and σ_{pay} are the thickness and stress of the pay zone, respectively. Figure 6-9 shows fracture height as a function of net pressure, as calculated by Eq. 6-49.

Although Eq. 6-49 is for a special case, it shows two interesting practical results. First, penetration into the barrier layers occurs at a critical net pressure:

$$p_{net,crit} = \sqrt{\frac{2K_{lc}^2}{\pi h_f}}. \quad (6-50)$$

For example, if K_{lc} is 2000 psi/in.^{1/2} and h_f is 20 ft [240 in.], the critical net pressure for breakthrough

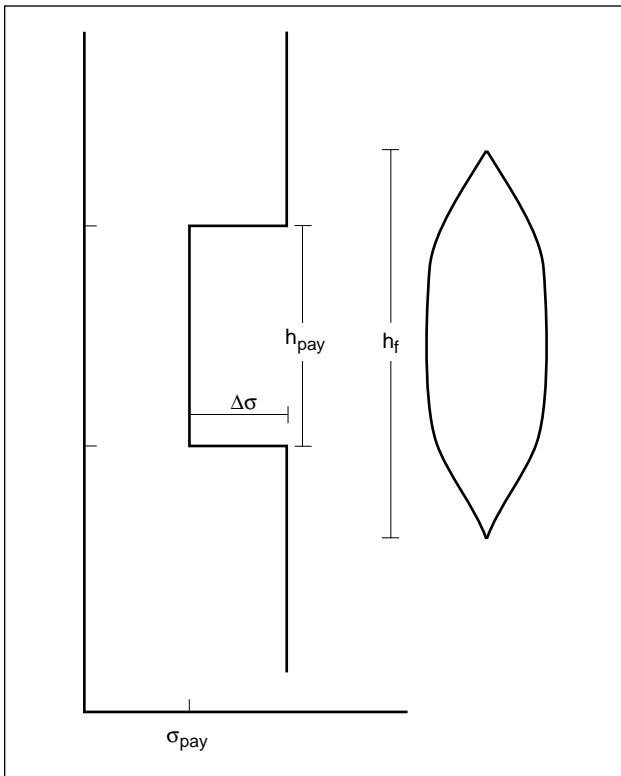


Figure 6-8. Simple three-layer height growth problem.

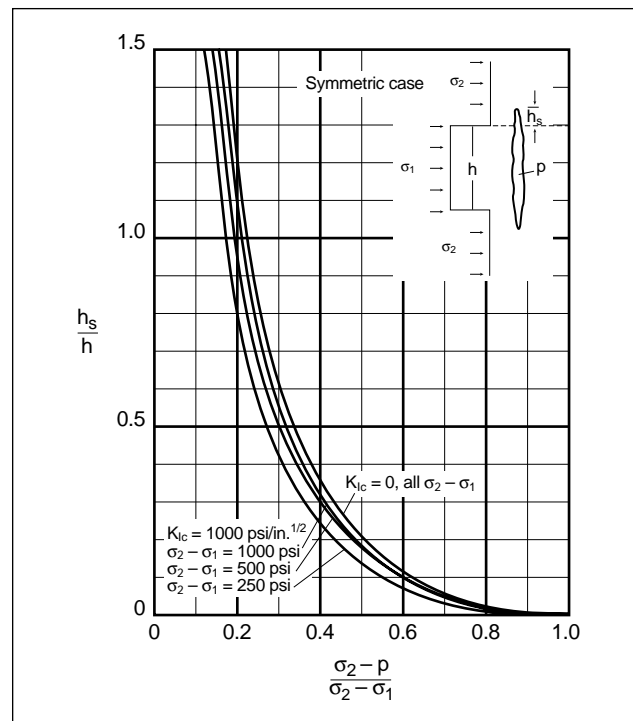


Figure 6-9. Fracture height versus net pressure for symmetric barriers. h_s = penetration into the boundary layer.

is only about 100 psi. Second, the net pressure cannot reach the stress contrast because this would result in infinite fracture height.

In a typical cell-based simulator, a table of these solutions is calculated prior to simulating the fracture evolution rather than at each time step of the calculation, and the relations among width, pressure and height are used to greatly speed up the solution of the fluid flow equations (conservation of mass and momentum).

- Fluid mechanics solution

One of the major differences between planar 3D and P3D models is the fluid flow calculation. The fluid flow model in most P3D models is the same as that introduced by Nordgren (1972) (i.e., a 1D version of the model described for the planar 3D model). In this model, both vertical flow and the variation of horizontal velocity as a function of vertical position are neglected. This results in the inability of typical P3D models to represent several aspects of behavior, namely (Smith and Klein, 1995)

- effect of variations in width in the vertical direction on fluid velocity
- local dehydration, which is approximated as simultaneous dehydration over the entire height of the fracture
- fluid loss after tip screenouts (TSOs), when fluid flow through the proppant pack is ignored
- proppant settling resulting from convection or gravity currents.

The average velocity and width are used (width is replaced by cross-sectional area divided by height) to simplify the conservation of mass (Eq. 6-38 for an incompressible fluid) to

$$\frac{\partial Au}{\partial x} + \frac{\partial A}{\partial t} = -2 \sum_i (u_L h_L)_i, \quad (6-51)$$

where u is the average cross-sectional velocity and u_L and h_L are the leakoff rate (Eq. 6-14) and height in each layer. Similarly, the conservation of momentum simplifies to

$$\frac{\partial p}{\partial x} = -\frac{\partial \tau_{xz}}{\partial z}. \quad (6-52)$$

For a power law fluid with properties n and K ,

$$\tau_{xz} = K \left(\frac{\partial u_x}{\partial z} \right)^n. \quad (6-53)$$

Solving Eq. 6-52 with Eq. 6-53 with the no-slip boundary condition (i.e., zero velocity at the fracture wall), the average velocity across the channel is

$$\bar{u}_x = -\text{sgn} \left(\frac{\partial p}{\partial x} \right) \left(\left| \frac{\partial p}{\partial x} \right| / K \right)^{1/n} \frac{n}{1+2n} \left(\frac{w}{2} \right)^{\frac{1+n}{n}}, \quad (6-54)$$

where sgn represents the sign of the quantity.

In the special case of a Newtonian fluid, $n = 1$ and $\mu = K$, and Eq. 6-54 becomes

$$\bar{u}_x = -\frac{w^2}{12\mu} \frac{\partial p}{\partial x}. \quad (6-55)$$

To obtain the total flow rate across the height of the cross section, and hence an average velocity for substitution in Eq. 6-51, Eq. 6-54 is integrated from the bottom to the top tip of the cross section:

$$q = \int_{h_f} w(y) \bar{u}_x(y) dy. \quad (6-56)$$

The average velocity is thus determined as

$$u = \frac{q}{A} = -\text{sgn} \left(\frac{\partial p}{\partial x} \right) \Phi \left[\left(\left| \frac{\partial p}{\partial x} \right| / 2K \right) \left(\frac{A}{h_f} \right)^{1+n} \right]^{1/n}, \quad (6-57)$$

where the channel function Φ is

$$\Phi = \left(\frac{h_f}{A} \right)^{\frac{1+2n}{n}} \frac{n}{2+4n} \frac{1}{h_f} \int w(y) \frac{1+2n}{n} dy. \quad (6-58)$$

Relations for the PKN model with power law fluids can be derived following this approach (see Nolte, 1979, 1991).

- Laminar and turbulent flow

When fluid flows between parallel plates at a low rate without leakoff, any fluid element remains a fixed distance from the wall of the channel, except in a small entrance region. This is known as laminar flow. By contrast, in turbulent flow, eddies occur, and fluid is continually mixed. This mixing results in added friction and different flow behavior. The Reynold's number N_{Re} (defined in Table 6G-1) enables determining whether laminar or turbulent flow will occur. If N_{Re} exceeds 2100, flow will be turbulent. Inside the fracture, N_{Re} is typically well below this value, except for particularly thin fluids, such as acid.

– Rheology of fracturing fluids

Fracturing fluids are generally treated as power law fluids, and because they are shear thinning (i.e., viscosity decreases with increasing shear rate), n is usually less than 1. The effective parameters of the power law model K' and n' are typically derived from laboratory measurements (see Chapter 8) over a range of shear rates. For shear-thinning fluids, the apparent viscosity (derived from K' and n') decreases as shear rate increases, and the viscosity would be infinite at zero shear rate. In reality, limiting low- and high-shear viscosities occur and must be considered.

Fracturing fluid properties change with time and temperature. Typically, exposure to high temperatures reduces fluid viscosity. However, crosslinkers may cause initial viscosity increases prior to the degradation. The effects of temperature and time are included in numerical hydraulic fracture simulators, typically by means of tables of K' and n' versus time at a series of temperatures, which are similar to those in service company handbooks.

• Numerical solution of the model

The three basic solutions described for height-growth mechanics (pressure-width-height relation), conservation of mass and conservation of momentum (velocity-pressure relation) are coupled and solved simultaneously. There are several methods by which the coupled equations may be solved, two of which are introduced here. Either a fixed or moving mesh may be used for the two methods, as described previously for planar 3D models. In this section, the explicit finite-difference method is introduced with a grid that moves with the fluid and an implicit method is described. In each case, prior to starting the simulation of the fracture evolution, a table of the pressure-height-width relation (from the equilibrium-height solution) is calculated as described for “Solid mechanics solution” in Section 6.3-2.

For the explicit finite-difference method, the fluid in the fracture at any time is divided into n elements, each with a cross-sectional area A_i and bounded by two vertical surfaces at x_i and x_{i+1} , moving at velocities u_i and u_{i+1} , respectively, as shown in Fig. 6-10. (The grid is numbered such that $i = 1$ represents the tip to facilitate the addition

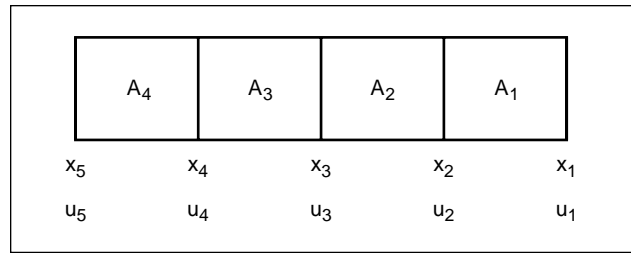


Figure 6-10. Fracture divided into elements with positions and velocities defined at grid points.

of new elements at the well, as necessary.) Mass-conservation Eq. 6-51 can be rewritten as

$$\frac{\partial A}{\partial t} = -2 \sum_i (h_L u_L)_i - \frac{\partial A u}{\partial x}, \quad (6-59)$$

with the derivatives replaced by central finite-difference approximations to obtain

$$A_i^{t+\Delta t} = A_i^t - \frac{h}{\Delta x} V_L + A_i^t (u_{i+1} - u_i) \frac{\Delta t}{\Delta x}, \quad (6-60)$$

where V_L represents the volume leaked off over the element of length Δx in time step Δt . The velocities are calculated at the grid points, and the area is assumed constant in each element. The cross-sectional area can thus be updated from the values of the velocities and areas at the previous time step. Once this has been done, the pressure at each cross section can be obtained from the solid mechanics solution by looking up the pressure in the precalculated pressure-height-width relation table for the corresponding area A . Pressure gradients can then be calculated using the approximation

$$\left. \frac{\partial p}{\partial x} \right|_i \approx \frac{p_{i-1} - p_i}{(x_{i-1} - x_{i+1})/2} \quad (6-61)$$

and new velocities obtained using Eq. 6-57. Once all the velocities are known at a given time, the positions of the grid points are updated using

$$x_i(t + \Delta t) = x_i(t) + u_i(t + \Delta t) \Delta t. \quad (6-62)$$

This method is known as a Lagrangian method because the grid coordinates move with the fluid. Leakoff causes each element to shrink and possibly even disappear as it penetrates farther into the fracture, limiting the usefulness of this method for modeling hydraulic fracturing treatments. In addition, new elements must continually be added at the wellbore. This makes it difficult to control how

many elements are present at any time or the sizes of the elements. Another approach is to introduce a fixed grid, as discussed for planar 3D models. This has the advantage that the number of elements in the simulation is relatively small near the beginning of the simulation when less accuracy is required and increases as the simulation progresses. Yet another approach is to introduce a moving mesh in which the grid points move at some reasonable velocity, for example, such that the fracture is always divided into a fixed number of equal-size elements (i.e., using a stretching coordinate system; see Sidebar 6H).

One of the primary limitations of explicit finite-difference methods, such as those introduced in the

preceding text, is that the time step used in the calculation may not exceed a critical value to ensure stability. Because only quantities from the previous step are used in moving forward, numerical errors can grow larger from step to step if the time step is too large. In the development of a general hydraulic fracturing simulator using such differencing schemes, the time step must be chosen carefully to avoid stability problems and yet minimize the computation time. A simple stability analysis is in Sidebar 6H.

It has been found that in cases of high leakoff or large widths (such as TSO designs), the critical time step for stability may be too small for efficient solution of the system, limiting the utility of the

6H. Stretching coordinate system and stability analysis

Stretching coordinate system

One way to simplify grid point bookkeeping is to use a stretching coordinate system. If

$$X = \frac{x}{L(t)}, \quad (6H-1)$$

then X will always remain bounded between 0 and 1 while x varies between 0 and $L(t)$. Placing a grid on X will fully cover the fracture regardless of the growth characteristics. However, although the gridding is simplified, the complexity of the differential equation is increased. The derivatives are found as

$$\frac{\partial}{\partial x} = \frac{1}{L} \frac{\partial}{\partial X} \quad (6H-2)$$

$$\frac{\partial}{\partial t} = \frac{\partial}{\partial t} - \frac{X}{L} \frac{dL}{dt} \frac{\partial}{\partial X}. \quad (6H-3)$$

Equation 6-59 becomes

$$\frac{\partial A}{\partial t} - \frac{X}{L} \frac{dL}{dt} \frac{\partial A}{\partial X} = -\frac{1}{L} \frac{\partial q}{\partial X} - q_L, \quad (6H-4)$$

and the other equations of the system are similarly transformed.

Stability analysis

A full stability analysis for a nonlinear system is difficult, but an approximate time-step limitation can be found as follows.

Assume that the pressure gradient can be written as

$$\frac{\partial p}{\partial x} = C_p \frac{\partial A}{\partial x}. \quad (6H-5)$$

In the case of the PKN model, where the fracture height h_f is fixed, $C_p = \beta h_f$, where β is defined by

$$p = \beta w. \quad (6H-6)$$

Substituting Eq. 6H-5 into Eq. 6-59 and applying the chain rule,

$$\frac{\partial A}{\partial t} = \frac{D}{n} A \left[A^{1+n} \frac{\partial A}{\partial x} \right]^{1/n-1} \left[A^{1+n} \frac{\partial^2 A}{\partial x^2} + (1+n) A^n \left(\frac{\partial A}{\partial x} \right)^2 \right], \quad (6H-7)$$

where absolute values must be assumed for all quantities, because an error analysis is being performed, and D is defined as

$$D = \frac{\Phi C_p^{1/n}}{(2Kh_f^{1+n})^{1/n}}. \quad (6H-8)$$

The highest order term in Eq. 6H-7 is

$$\frac{D}{n} A \left[A^{1+n} \frac{\partial A}{\partial x} \right]^{1/n-1} \left[A^{1+n} \frac{\partial^2 A}{\partial x^2} \right]. \quad (6H-9)$$

If the derivative is expanded using a central difference approximation, the term in A_x becomes

$$\frac{-2D}{n(\Delta x)^2} \frac{\partial A}{\partial x} A^{3+1/n}. \quad (6H-10)$$

To investigate the effect of an error introduced into A , A is replaced by $A(1 + \varepsilon)$, which can be approximated (for small ε) as

$$\frac{-2D}{n(\Delta x)^2} \frac{\partial A}{\partial x} A^{3+1/n} \left(1 + \left(3 + \frac{1}{n} \right) \varepsilon \right). \quad (6H-11)$$

If a time step is taken (discretizing Eq. 6H-7 similar to Eq. 6-59), then the error ε grows to

$$E = \Delta t \frac{-2D}{n(\Delta x)^2} \frac{\partial A}{\partial x} A^{3+1/n} \left(1 + \left(3 + \frac{1}{n} \right) \varepsilon \right). \quad (6H-12)$$

For this error to reduce in magnitude, it must be smaller than $A\varepsilon$, which can occur only if

$$\Delta t < \frac{(\Delta x)^2}{2AC_p C_v}, \quad (6H-13)$$

where the viscosity leakoff control coefficient C_v is

$$C_v = -\frac{(3n+1)v}{\frac{\partial p}{\partial x} n^2}. \quad (6H-14)$$

explicit scheme. An implicit finite-difference scheme, with no time-step limitation, may eliminate this limitation. In essence, implicit and explicit methods can be distinguished by the fact that explicit methods solve for quantities at one time step on the basis of only values at the previous time steps, whereas implicit methods include the use of quantities at the current time. This implies that a set of equations is set up and solved, because the quantities at the current time step must all be found simultaneously. For linear problems, a set of linear equations results, and these are easily solved by standard methods such as gaussian elimination. For the 1D flow problem, the implicit finite-difference formulation yields a tridiagonal system of equations (i.e., a sparse matrix with only three diagonals filled with nonzeros). Highly efficient solution techniques are available to solve such systems (e.g., Carnahan *et al.*, 1969). For nonlinear problems, however, such methods can be complex and are not always much more efficient than explicit methods. Iteration is frequently required, because a nonlinear system is linearized. If the linearization approximation is inaccurate, it must be corrected and resolved.

Another method without the time-step limitation, and which avoids forming a system of equations, is a method using integrated or analytical elements. A similar method to that described in the following was the basis of the commercial time-sharing method made available by Amoco between 1981 and 1983 (Nolte, 1982, 1988a). Consider once again the basic equations of the PKN model with $x = \phi$ at the tip:

$$w = \frac{2p_{nef}h_f}{E'} \quad (6-63)$$

$$\frac{dp}{dx} = \frac{64q\mu}{\pi h_f w^3}. \quad (6-64)$$

Substituting Eq. 6-64 for p into Eq. 6-63 obtains

$$\frac{E'}{2h_f} \frac{dw}{dx} = \frac{64q\mu}{\pi h_f w^3}. \quad (6-65)$$

Detailed numerical simulations have shown that the velocity varies much more slowly than the flow rate q because the reduction in width toward the tip partially compensates for fluid leakoff and storage in the fracture. Instead of the Perkins and Kern

(1961) assumption that q is constant (Eq. 6-10), replacing q by $\pi u h_f w/4$ allows writing Eq. 6-65 as

$$\frac{dw}{dx} = \frac{32\mu h_f}{E' w^2} u \quad (6-66)$$

or

$$w^2 dw = \frac{32\mu h_f}{E'} u dx. \quad (6-67)$$

Integrating over a distance Δx obtains

$$w(x + \Delta x) = \left[w^3(x) + \int_x^{x+\Delta x} \frac{96\mu h_f}{E'} u dx \right]^{1/3}. \quad (6-68)$$

If the terms under the integral can be assumed to be constant, this simplifies further to

$$w(x + \Delta x) = \left[w^3(x) + \frac{96\mu h_f}{E'} u \Delta x \right]^{1/3}. \quad (6-69)$$

If the height is not constant and the fluid is non-Newtonian, a similar equation can be written for the cross-sectional area of the fracture by using the power law rheological parameters:

$$A_{i+1}^t = \left[(A_i^t)^{n+2} + \frac{(n+2)\pi K h_f^{n+3}}{E' \Phi^n} u^n \Delta x \right]^{1/(n+2)}, \quad (6-70)$$

where

$$\Phi = \frac{n}{h_f(2+4n)} \int_{h_f} \left(\frac{w(y)}{\bar{w}} \right)^{\frac{1+2n}{n}} dy. \quad (6-71)$$

For an analytical solution, Δx would be the entire fracture length (Nolte, 1991), and this would be combined with a tip criterion and a volume-balance equation. The numerical solution proceeds similarly, except that Δx is chosen sufficiently small to obtain an accurate solution. Fluid loss is integrated over the time step, which allows obtaining acceptable accuracy, even with large time steps. The solution method at each time step is as follows:

1. Estimate a tip velocity.
2. For each element, working in from the tip to the well,
 - a. calculate an average fluid velocity based on the velocity at the outer side of the element and the estimated velocity at the inner side (At the first iteration, assume the inner fluid velocity is equal to the outer fluid velocity.)

- b. determine the cross-sectional area at the inner side of the element for the estimated velocity by using Eq. 6-70
 - c. determine the velocity at the inner side such that the leakoff and element volume change during the time step result in a mass balance
 - d. repeat the iteration using the new velocity.
3. Compare the actual flow into the fracture with the wellbore velocity calculated by the iterative scheme in the preceding step.
 4. Refine the estimate of the tip velocity using a Newton-Raphson method until volume balance is achieved, which typically takes two to four iterations.

This method of solving the equations is efficient because the velocity does not vary significantly along the fracture for typical cases. For typical PKN cases with a single fluid, the fracture can be divided into about 10 elements. For non-PKN cases, the grid must be chosen sufficiently fine that the integrand in Eq. 6-68 (which includes effects of fluid rheology and fracture height) is approximately constant in each element (because the solution scheme is derived with the assumption that it is constant).

Regardless of whether a moving- or fixed-grid method is used, usually only a small number of elements (about 10) is necessary to obtain a reasonably accurate solution to the equations described so far. However, other information may be required at a much finer resolution. To achieve this, the schedule is typically divided into a large number of substages (about 100). Quantities such as proppant concentration, fluid temperature and acid concentration can then be tracked on this finer grid. In addition, particularly in acid fracturing, it is desirable to track leakoff and etching on a finer grid. To do this for methods using a moving grid, a second grid that does not move is established. Quantities such as reservoir temperature, proppant bank height and leakoff volume in the reservoir are tracked on this solid-based grid.

- Nonequilibrium-height solution

It was noted in “Solid mechanics solution” in Section 6.3-2 that the assumption of slow height growth allows creating a pressure-height-width table prior to solving the equations of fracture evolution. This so-called equilibrium-height assumption

is quite accurate, provided that the fluid is moving relatively slowly in the vertical direction so that the pressure drop resulting from vertical fluid flow is negligible. This assumption is violated if high-permeability zones are exposed, because fluid must then move rapidly because of the increased leakoff in such layers. Also, if the stress in the surrounding zones is insufficient to confine the fracture and the vertical tips extend quickly, then the fluid must move quickly to fill the resulting fracture. In either of these cases, the pressure gradient resulting from vertical fluid flow may become large, and the equilibrium-height assumption becomes invalid at these locations in the fracture.

To remove this assumption and obtain valid results from a simulator, some restriction must be placed on height growth. For nonequilibrium-height growth, the pressure gradient because of fluid flow in the vertical direction must be approximated, based on the rate of height growth. It is common to base this approximation on the KGD model (e.g., Settari and Cleary, 1982). In Section 6-7 on tip effects, an analytical near-tip solution developed by Lenoach (1994) is discussed that provides an expression for the net pressure of the form

$$p_{net} = E' \left(\frac{2\sqrt{2}(2+n)}{\pi(2-n)} \right) \times \left[\frac{K}{E' h_f^n} \left(\frac{\cos[(1-\beta)\pi]}{\sin(\beta\pi)} \right)^{1+n} \left(\frac{2n+1}{n} \right)^n \frac{1}{n(2+n)^n} u_{tip}^{n/(2+n)} \right] \quad (6-72)$$

where u_{tip} is the tip velocity and β is $2/(2+n)$. As previously noted, for a fracture under constant pressure, the stress intensity factor is related to the net pressure by

$$p_{net} = \frac{K_{Ic}}{\sqrt{\pi h_f/2}} \quad (6-73)$$

The Lenoach tip solution can be used to obtain an apparent fracture toughness caused by the non-zero tip velocity by combining Eqs. 6-72 and 6-73. This effect can be added to the actual rock toughness, and the sum is used in Eqs. 6-46 and 6-47 instead of the actual rock toughness to determine the fracture height growth. The basic algorithm used to move from one pair of vertical tip positions to another during a time step is as follows:

1. Estimate the top and bottom tip velocities for the cell.
2. Calculate the new fracture tip positions at the end of the time step, using these velocities.
3. Calculate the stress intensity factors from Eqs. 6-46 and 6-47.
4. Determine the excess stress intensity factors (i.e., the calculated value minus the rock toughness).
5. Calculate the velocities required to generate these excess stress intensity factors, using Eqs. 6-72 and 6-73.
6. Compare the velocities with the guessed values and iterate until the correct velocities are found.

One of the advantages of the equilibrium-height models is the speed gained by precalculating a table of the fracture height-pressure relation. Not only is this not possible for the nonequilibrium model, but the iterative process to determine the tip positions can be time consuming. The nonequilibrium-height algorithm should therefore be used only when necessary because of the apparent rapid height growth indicated by the equilibrium-height calculation.

- **Lateral coupling**

In the description of the solid mechanics solution provided previously, the basic assumption is that individual cross sections act independently (i.e., plane strain in the horizontal direction, or laterally decoupled). This is implicit in the assumption that the pressure and width at any point are uniquely related. In reality, the pressure at any point is dependent not only on the local width, but also on the width distribution over the entire fracture, as discussed in Section 6-3.1 on planar 3D models. This lateral coupling is generally not important, unless the fracture wing length is less than the height. Even then, the fracture geometry will not be significantly different if lateral coupling is neglected, although the pressure response may be underestimated. Lateral coupling can be included in the solutions described previously (see Sidebar 6E).

The effect of lateral coupling during pumping is to increase the pressure at and near the well and to decrease it near the tip. Figure 6-11 shows the evolution of pressure during a treatment for a confined fracture simulated using the KGD, PKN and later-

ally coupled PKN models. The pressure predicted by the laterally coupled model is always higher than either the KGD or PKN solution would predict. It can also be shown that the width at the well is always smaller than that predicted by either of the simple models. The point in Fig. 6-11 where the pressure from the laterally coupled model is lowest (and where the pressures from the KGD and PKN models are equal) corresponds to a square, where the fracture wing length is one-half of the height. The pressure calculated by the laterally coupled model exceeds that predicted by the KGD or PKN model at this time by approximately 40%, which is comparable to the pressure in a radial fracture of similar dimensions.

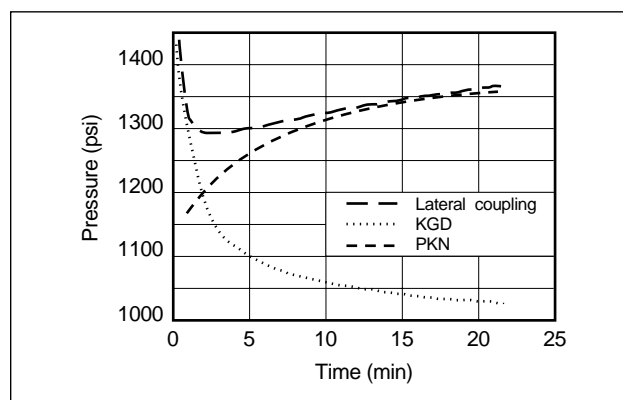


Figure 6-11. Pressure record with and without lateral coupling.

6-3.3. Lumped pseudo-three-dimensional models

Lumped models are an alternative to cell-based models and were first introduced by Cleary (1980b). Although more details are presented in subsequent paragraphs, it is worthwhile at this point to quote two sentences from the conclusions of his paper: “the heart of the formulae can be extracted very simply by a nondimensionalization of the governing equations; the remainder just involves a good physico-mathematical choice of the undetermined coefficients” and “results could be presented in the usual format of design charts, based on dimensionless groups extracted, . . . [a] more appealing procedure may be to program the solutions for a suitable pocket calculator, with the separately determinable γ or Γ coefficients and job parameters as input.” Although numerous papers have

been presented on the use of this model (e.g., Cleary *et al.*, 1994), which is now on laptop computers rather than pocket calculators, these sentences capture the essence of lumped models in that they are extremely simple models and the key to their successful use is the selection of appropriate coefficients for the problem analyzed.

Like all the models presented previously, the starting point of the lumped model is the set of basic equations defining the hydraulic fracturing process, which are mass conservation (Eq. 6-39), the relation between the distribution of crack opening over the length of the fracture $2L$, net pressure distribution (similar to Eq. 6-36) expressed as

$$p_{net}(x) = \int_{-L}^L I(x, x') w(x') dx', \quad (6-74)$$

and conservation of momentum (Eq. 6-40) expressed as

$$\tilde{q} q^{m-1} = -\gamma_4 w^{2n-m+1} \tilde{\nabla} p / \mu, \quad (6-75)$$

where γ_4 is the channel factor ($1/2$ for a Newtonian fluid), and various combinations of the power law factors m for turbulence and n enable consideration of both non-Newtonian fluids and turbulent flow.

In the lumped models, these equations are simplified by assuming a fracture shape and adopting a spatial averaging approach to reduce them to ordinary differential equations in time. This approach implicitly requires the assumption of a self-similar fracture shape (i.e., one that is the same as time evolves, except for a length scale). The shape is generally assumed to consist of two half-ellipses of equal lateral extent, but with different vertical extent.

It is instructive to consider some of the lumped equations for the KGD model (Cleary, 1980b). The mass balance is obtained by averaging over the fracture length:

$$\rho(q\bar{w} - Lq_L) = d(\gamma_3 \rho \bar{w} L) / dt, \quad (6-76)$$

where

$$\bar{w} \approx (\gamma_1 p_{net} / E) L \quad (6-77)$$

$$q^m \bar{w}^m \approx \gamma_5^m (\bar{w})^{2n+2} / L^2, \quad (6-78)$$

where

$$\gamma_5^m \equiv \gamma_2 \gamma_4 E / (\gamma_1 \mu), \quad (6-79)$$

which is the 1D form of Eq. 6-75. Equation 6-76 is similar to Eq. 6-15 (based on Carter, 1957) with the

addition of γ_3 , and Eq. 6-77 is identical to that of Geertsma and de Klerk (1969) with γ_3 replacing $4(1 - \nu^2)$. Superficially, these equations are extremely simple, but the values of the γ coefficients are not always obvious and may not be constant. As noted by Crockett *et al.* (1989), these models are extremely general, with the degree of accuracy limited ultimately only by the effort invested in determination of the γ coefficients by detailed simulations, laboratory experiments or field studies.

For more general fracture shapes (i.e., with height growth), it is typically assumed that height growth is governed by a KGD-type solution and length growth by a PKN-type solution (Cleary *et al.*, 1983), although this is not a theoretical limitation of lumped models.

One area in which lumped models have been exploited extensively is in the development of computer software systems to apply and use pressure data during a treatment. Some of the key characteristics and requirements for such a software system are that (Crockett *et al.*, 1989)

- the physics is realistic and general
- execution time is much faster than treatment time to allow repetitive execution for pressure history matching
- the software can use improved estimates of parameters obtained in real time (i.e., during the treatment).

Although these real-time software systems are generally referred to as real-time hydraulic fracture models (e.g., Crockett *et al.*, 1989), the model itself is only a small part of the software and should address the first requirement listed (i.e., realistic and general physics). The second and third requirements are computer hardware and software design constraints. Because lumped models were developed for pocket calculators in 1980, they impose a minimal impact on computer hardware and systems. As computing power continues to improve, it will become possible to run increasingly sophisticated models during treatment execution either at the wellsite or remotely. There are other software design issues, such as robust execution with a wide variety of parameter values, easy import and superposition of actual data on model output, and graphical display, that are required for a useful software system for real-time applications. Discussion of these issues is beyond the scope of this volume.

6-4. Leakoff

One of the key issues in designing a fracture treatment is accurate knowledge of how rapidly fluid will leak out of the fracture into the reservoir. Without this information, it would be impossible to design a treatment that provides a specified fracture geometry.

Mini-fracture treatments are performed to estimate the leakoff coefficient (see Chapter 9). Equation 6-14 introduced in “Inclusion of leakoff” in Section 6-2.2 is the basic equation of filtration and was first used for fracturing by Carter (1957). He showed that it was applicable for three separate leakoff processes:

- displacement and compressibility of reservoir fluid
- invasion of the formation by filtrate or fracturing fluid
- buildup of an external filter cake.

Williams (1970) divided the leakoff into three time periods, rather than considering the three processes. During the initial period, leakoff is quick, followed by a decreasing leakoff rate and finally a steady-state leakoff rate. In the initial period, filter cake has not formed, so the leakoff rate is controlled by the resistance of the formation to flow of the fracturing fluid. The external filter cake builds during the second period. Finally, the cake stops building, because the high-velocity fluid in the fracture prevents further polymer deposition. This last stage is referred to as dynamic leakoff. Williams lumped all leakoff prior to dynamic leakoff into a quantity he called spurt volume, although spurt loss has since been generally accepted to refer only to the initial high-leakoff period before the cake starts building.

Settari (1985) presented an excellent review of the classic leakoff model, as well as an even more general model of leakoff that represents an excellent framework for leakoff modeling. In the following sections, each of the three processes (displacement and compressibility of reservoir fluid, invasion of the formation by filtrate or fracturing fluid and buildup of filter cakes, either externally on low-permeability rocks or internally on high-permeability rocks) is considered as if it is the only one acting and then in combination. Finally, Settari’s general model is summarized.

The fluid-loss derivations in Eqs. 6-82 through 6-91 are for the pressure drop for individual loss mechanisms. For general application, they are in terms of the total pressure drop between the fracture and initial reservoir pressures in Eqs. 6-94 through 6-96 and in oilfield units in Eqs. 8-26 and 8-27.

6-4.1. Filter cake

In laboratory filtration experiments performed at constant pressure, the rate of filtration is proportional to the square root of time (see Chapter 8). A model for this process can be derived by assuming that

- the amount of cake deposited is proportional to the volume of fluid V_L passed through a unit surface area
- cake permeability k_{cake} is independent of its thickness
- flow through the cake obeys Darcy’s law
- pressure drop across the cake Δp_{cake} is constant

to write

$$u_L = \frac{dV_L}{dt} = \frac{k_{cake}}{\mu_{fil}} \frac{\alpha \Delta p_{cake}}{V_L}, \quad (6-80)$$

where μ_{fil} is the viscosity of the filtrate and it is assumed that the cake thickness L_{cake} is proportional to the fluid volume lost; i.e., $V_L = \alpha L_{cake}$. By integrating for V_L , it can be shown that

$$u_L = C_w / \sqrt{t}, \quad (6-81)$$

where the fluid-loss coefficient through the wall filter cake is

$$C_w = \sqrt{\frac{k_{cake} \alpha \Delta p_{cake}}{2\mu_{fil}}}. \quad (6-82)$$

Carter (1957) proposed that the volume leaked off can then be determined as

$$V_L = 2C_w \sqrt{t} + S_p, \quad (6-83)$$

where S_p is the volume that leaks off without forming a filter cake and can be interpreted as an integration constant. A more appropriate physical model is to assume that the initial volume that leaks off, without building a cake, is the spurt volume and that Eq. 6-80 applies after the cake is established. This interpretation results in

$$V_L = 2C_w \sqrt{t - t_{sp}} + S_p, \quad (6-84)$$

where t_{sp} is the spurt time.

Another approach to account for leakoff by using standard petroleum engineering concepts of reservoir permeability and treating the filter cake as a pressure-dependent resistance is outlined in Chapter 2 along with high-permeability conditions (Valkó and Economides, 1997). The following approach to the leakoff coefficient is as presented by Settari (1985).

6-4.2. Filtrate zone

The first zone inside the reservoir is called the filtrate zone or invaded zone. It is assumed that

- pressure drop Δp_v across the zone is constant
- filtrate fully displaces the mobile phase(s) within the formation, resulting in piston-like displacement and 100% filtrate saturation
- the fluid and rock are incompressible

to write

$$u_L = \frac{dV_L}{dt} = \frac{k_{fil}}{\mu_{fil}} \frac{\Delta p_v}{L_v}, \quad (6-85)$$

where k_{fil} is the permeability related to the filtrate and L_v is the length of the invaded zone. Integrating this equation, with the assumption that

$$L_v = V_L/\phi = \frac{1}{\phi} \int u_L dt, \quad (6-86)$$

where ϕ is the porosity, obtains

$$u_L = \frac{C_v}{\sqrt{t}}, \quad (6-87)$$

where the viscosity control leakoff coefficient C_v is

$$C_v = \sqrt{\frac{k_{fil}\phi\Delta p_v}{2\mu_{fil}}} \quad (6-88)$$

and the leakoff volume at any time is

$$V_L = 2C_v\sqrt{t}. \quad (6-89)$$

The permeability to the filtrate k_{fil} reflects the relative permeability of the formation to flow of the filtrate. This effect may be significant when a water filtrate enters a hydrocarbon zone at nearly irreducible water saturation.

6-4.3. Reservoir zone

Although the uninvaded reservoir does not contain fracturing fluid, pressure is required to displace the reservoir fluid away from the fracture face. Assuming

- constant pressure drop Δp_c between the filtrate/reservoir interface and the far-field reservoir
- compressible flow with constant total compressibility c_t
- relatively slow movement of the front of the invading fluid
- an infinite reservoir,

the front can be treated as the face of an infinite porous medium, and an analytical solution (Collins, 1961) is used to obtain

$$u_L = \frac{C_c}{\sqrt{t}}, \quad (6-90)$$

where the compressibility control leakoff coefficient C_c is

$$C_c = \sqrt{\frac{k_r c_t \phi}{\pi \mu_r}} \Delta p_c, \quad (6-91)$$

where k_r is the permeability of the reservoir rock and μ_r is the reservoir fluid viscosity.

6-4.4. Combined mechanisms

In practice, all three processes occur simultaneously. The leakoff velocities in Eqs. 6-80, 6-85 and 6-90 must be equal, and the sum of the pressure drops must equal the total pressure difference between the reservoir pressure and the fracturing pressure:

$$\frac{C_t}{\sqrt{t}} = \sqrt{\frac{k_{cake} \alpha \Delta p_{cake}}{2\mu_{fil}(t-t_{sp})}} = \sqrt{\frac{k_{fil}\phi\Delta p_v}{2\mu_{fil}t}} = \sqrt{\frac{k_r c_t \phi}{\pi \mu_r t}} \Delta p_c \quad (6-92)$$

$$\Delta p_{cake} + \Delta p_v + \Delta p_c = \Delta p_{total}, \quad (6-93)$$

where C_t is the total leakoff coefficient and Δp_{total} is the difference between the pressure in the fracture and the far-field reservoir pressure p_r . If the spurt volume and time can be neglected, these equations can be combined (Williams *et al.*, 1979) to yield the total leakoff coefficient:

$$C_t = C_{wcv} = \frac{2C_c C_v C_w}{C_v C_w + \sqrt{C_w^2 C_v^2 + 4C_c^2 (C_v^2 + C_w^2)}} \quad (6-94)$$

with the coefficients C_w , C_c and C_v calculated using the overall pressure difference.

Equation 6-94 is valid only if the cake permeability is independent of pressure. If the cake is highly compressible and the cake permeability is approximately proportional to $1/\Delta p$, Nolte (1988a) has shown that the fluid loss is limited either by the cake or the reservoir. In that case, the fluid-loss rate is the minimum of Eq. 6-81, with the pressure drop equal to the total pressure drop, or

$$u_L = \frac{C_{cv}}{\sqrt{t}}, \quad (6-95)$$

where the combined leakoff coefficient is

$$C_{cv} = \frac{2C_c C_v}{C_v + \sqrt{C_v^2 + 4C_c^2}} \quad (6-96)$$

with the coefficients C_c and C_v again calculated using the total pressure difference.

6-4.5. General model of leakoff

A great deal of complexity can be added to the leakoff model in an attempt to account for detailed behavior such as the compressibility of the invading fluid and the moving boundary of the reservoir fluid. Given the accuracy with which the other parameters in a hydraulic fracture treatment are known, the inclusion of such effects is generally unnecessary. This section describes modification of the models to incorporate the two effects of the variable pressure difference and changing fluid properties.

The model described in previous sections can be generalized to account for multiple fluids. Settari (1985) showed that the fluid loss in the invaded zone can be described by replacing the term C_v with an equivalent term:

$$\bar{C}_v = \frac{2C_v^2 \sqrt{t}}{V_L}, \quad (6-97)$$

where C_v is calculated using the average viscosity and relative permeability of all the filtrate leaked off to the current time, and V_L is the fluid volume that previously leaked off into the reservoir. Settari also showed that replacing the wall-building coefficient for the fluid under consideration with an equivalent value would account for variations in leakoff behavior between fluids in a treatment. The equivalent value in this case is

$$\bar{C}_w = \frac{2C_w^2 \sqrt{t}}{V_L}, \quad (6-98)$$

where the previously leaked-off fluid volume V_L has also contributed to wall building.

The critical fluid component affecting wall building is the gel and/or fluid-loss additive concentration. An extension to Settari's model can be derived by considering Eq. 6-80, in which the thickness of the cake is assumed to be proportional not to the volume flowed through the wall but to the volume of gel deposited. Thus, the thickness is proportional not to the time-integrated velocity but to the integral over time of the

product of gel concentration and fluid velocity. In this case, Eq. 6-98 is replaced by

$$\bar{C}_w = \frac{2C_{gel} C_w^2 \sqrt{t}}{M_{gel}}, \quad (6-99)$$

where C_{gel} is the gel mass concentration in the fluid and M_{gel} is its specific density. There is an implicit assumption that the term $C_{gel} C_w^2$ is constant. This assumption is consistent with laboratory work reported by Mayerhofer *et al.* (1991). The viscosity of water decreases with increasing temperature, and this effect on the leakoff coefficient should be included in the fracture model.

6-4.6. Other effects

- Pressure evolution during treatment

If an estimate of the leakoff coefficient has been obtained from a mini-fracture decline analysis, then the most likely way to use the simulator would be to enter the total leakoff coefficient derived from the analysis. It is thus assumed that the leakoff behavior during the minifracture is the best representation of what will occur during the main treatment. However, if the leakoff behavior is unknown and is to be determined from fluid and reservoir properties, the best approach is to enter a laboratory-determined wall-building coefficient for each fluid and use the simulator to determine the total leakoff coefficient at each position in the fracture as a function of time and on the basis of the continually evolving pressure difference between the fracture and the reservoir. Except in overpressured reservoirs, the assumption of a constant total pressure difference is generally reasonable. The ratio of leakoff coefficients between the lowest pressure difference during the treatment (when the net pressure is zero and the pressure difference between the closure stress and the reservoir pressure is just $\Delta p = \sigma_c - p_r$) and at the end of pumping (when it is $\Delta p = p_{net} + \sigma_c - p_r$) is given for reservoir-controlled leakoff by

$$\frac{C_c(p_{net} = 0)}{C_c(p_{net} = p_{net,max})} = \frac{\sigma_c - p_r}{p_{net,max} + \sigma_c - p_r} \quad (6-100)$$

and for the wall-building or viscosity-controlled cases by

$$\frac{C_L(p_{net} = 0)}{C_L(p_{net} = p_{net,max})} = \sqrt{\frac{\sigma_c - p_r}{p_{net,max} + \sigma_c - p_r}}. \quad (6-101)$$

If the ratio is close to 1, a constant leakoff model can be used, in which the leakoff coefficients (C_c , C_v and C_w) for each fluid in the treatment can be precalculated on the basis of an assumed typical net pressure (e.g., 250 psi). If the effect of pressure changes is large, a variable leakoff model can be used, in which the pressure changes in the fracture are accounted for as the simulation proceeds. In this case, the reservoir component of leakoff C_c should be determined using a convolution of the pressure history during the treatment.

- Pressure-sensitive leakoff

One of the major assumptions of the analysis in the previous sections is that the permeability remains constant. In fact, many reservoirs may have fissures or other features that may open under the influence of the fracture treatment. The effect of this opening is to increase the leakoff rate (Warpinski, 1991). Pressure-sensitive leakoff is addressed more fully in Chapter 9.

- Poroelasticity and backstress

Chapter 3 discusses the influence of pore pressure on rock mass behavior. Poroelastic effects are changes in stress that occur as a result of changes in pore pressure in the reservoir. As fluid leaks out of the fracture into the reservoir, the affected part of the reservoir dilates, and a “backstress” develops, which increases the effective closure pressure. This effect is generally small, but it may be important in some cases, as discussed by Nolte *et al.* (1993). Chapter 3 provides the solution for a fracture in an infinite, homogeneous medium. Although the additional pressure results in an increased net pressure in the fracture, it generally has little effect on fracture geometry.

6-5. Proppant placement

The objective of hydraulic fracturing is to place proppant to provide a conductive path for production. The presence of proppant introduces three important issues in the behavior of fluids in hydraulic fractures:

- effect of proppant on fluid rheology
- convection or gravity currents
- proppant transport.

6-5.1. Effect of proppant on fracturing fluid rheology

Generally the viscosity of a proppant-laden slurry μ_{slurry} is higher than that of the carrying fluid μ_{base} alone. Experimental relations are well established for Newtonian fluids, but much less so for power law fluids. Nolte (1988b) showed that relations for power law fluids could be obtained by using the relations for Newtonian fluids and raising them to the power of n . For example, the viscosity ratio μ_r could be obtained as

$$\mu_r = \frac{\mu_{slurry}}{\mu_{base}} = \frac{1}{(1 - f_v/f_{vM})^{2.5n}}, \quad (6-102)$$

where f_v is the proppant volume fraction, and f_{vM} is the maximum fraction for a mobile slurry.

6-5.2. Convection

Density differences between fluids may result in the denser fluid flowing under the lighter fluid or the lighter fluid overriding the denser fluid. This phenomenon, known as convection or gravitational flow, is important in many fields, such as saltwater intrusion under fresh water (Badon Ghyben, 1888; Herzberg, 1901). In fracturing, it may be relevant if a high-density slurry stage flows under a previously pumped stage or pad, as well as for other 2D aspects of fluid flow, such as those considered by Clifton and Wang (1988).

The fluid flow equations for a Newtonian fluid can be written as

$$\begin{aligned} u_x &= \frac{-w^2}{12\mu} \frac{\partial p}{\partial x} \\ u_y &= \frac{-w^2}{12\mu} \left(\frac{\partial p}{\partial y} + \rho g \right) \end{aligned} \quad (6-103)$$

and (Eq. 6-38 for incompressible fluids)

$$\left(\frac{\partial(wu_x)}{\partial x} + \frac{\partial(wu_y)}{\partial y} \right) + \frac{\partial w}{\partial t} + 2u_L = 0. \quad (6-104)$$

Substituting Eq. 6-103 into Eq. 6-104 obtains

$$\frac{1}{12\mu} \left(\frac{\partial^2 w^3 p}{\partial x^2} + \frac{\partial^2 w^3 p}{\partial y^2} \right) = \frac{\partial w}{\partial t} + 2u_L - \frac{1}{12\mu} \frac{\partial w^3 \rho g}{\partial y}. \quad (6-105)$$

The last (gravitational) term on the right-hand side of Eq. 6-105 is the convective term. This can be treated as a source term, just as the other two terms are storage or sink terms, resulting from width change and leakoff. Barea and Conway (1994), Unwin and Hammond (1995) and Smith and Klein (1995) showed that this is generally not significant for most properly designed fracturing treatments. Smith and Klein showed that if excess pad was pumped, the fluid flow after pumping stops (i.e., afterflow) could lead to convection until the pad leaked off. Also, Eq. 6-105 shows the extreme sensitivity of convection to fracture width. If the width is large (e.g., in a low-modulus rock), convection may be more critical. Fortunately, such low moduli are usually associated with high permeabilities, in which case TSO designs and rapid leakoff after shut-in effectively prevent convection. Cleary and Fonseca (1992) presented a dimensionless number that reflects the ratio of buoyant and viscous forces. This ratio can be used to estimate the effect of different conditions on the severity of convection.

Finally, Clark and Courington's (1994) and Clark and Zhu's (1994) experiments on convection largely verify the theoretical and numerical results described here.

6-5.3. Proppant transport

Hydraulic fracturing produces a conductive channel by placing proppant in a crack created in a pay zone. Hence, an essential consideration in fracturing fluid design is to accomplish proppant transport. The effect of convection on proppant transport was previously discussed. There are two other factors that may impact proppant placement. The first, and most commonly understood, is settling. If a bottle containing a mixture of sand and water is shaken up and then left on a table, the sand will settle out of the water. It can be shown theoretically that the terminal velocity of a single particle far from any walls in a stagnant Newtonian fluid is given by Stokes law:

$$u_{\infty} = \frac{g(\rho_{sol} - \rho_f)d_{sol}^2}{18\mu}, \quad (6-106)$$

where ρ_{sol} is the solid particle density, ρ_f is the fluid density, and d_{sol} is the solid particle diameter.

The assumptions of this equation are of limited applicability in hydraulic fracturing because the fluids are non-Newtonian and the particles are highly con-

centrated and may be close to the channel walls, which causes two effects: hindered settling, which implies that particles get in the way of each other, and clustered settling, in which particles join together, effectively increasing the diameter in Eq. 6-106. Novotny (1977) presented a correlation for the particle velocity u_{sol} in hindered settling in terms of the volume fraction of solids f_v :

$$u_{sol} = u_{\infty}F(f_v), \quad (6-107)$$

where

$$F(f_v) = (1 - f_v)^{\beta} \quad (6-108)$$

and the exponent β ranges from 5.5 at low values of N_{Re} to 2 at high values of N_{Re} . For power law fluids, a generalized form of Stokes law (Eq. 6-106) is used:

$$u_{\infty} = \left[\frac{(\rho_{sol} - \rho_f)g d_{sol}^{n+1}}{3^{n-1}18K'} \right]^{1/n}. \quad (6-109)$$

Equation 6-108 can still be used to account for hindered settling. Other correlations have been developed, but a definitive correlation has not appeared in the literature. Many fracturing fluids are designed for almost perfect transport, so the settling rate is usually not important unless the fracture remains open for a long time after pumping stops.

Another effect on proppant placement is fluid migration (Nolte, 1988b) or encapsulation (Cleary and Fonseca, 1992). Fracturing fluids are generally viscoelastic. Although it is beyond the scope of this section to discuss this phenomenon in detail, one of its important effects is to drive proppant to the center of the flow channel. This migration could result in a dense sheet near the center of the channel, surrounded by clear fluid. This has the effect of accelerating particle settling, especially for low proppant concentrations. Unwin and Hammond (1995) presented simulations showing the effect of this migration on proppant placement.

6-6. Heat transfer models

The properties of many fracturing fluids show some dependence on temperature. In addition, the rates of the reactions that occur in acid fracturing are dependent on temperature. In a typical fracturing treatment, the fluid is pumped at a temperature signifi-

cantly below the reservoir temperature. As the fluid penetrates farther into the fracture, heat transfer occurs between the fracturing fluid and the rock, resulting in an increase in fluid temperature.

The temperature gradient in the direction perpendicular to the fracture wall is significantly larger than those in other directions, so the temperature gradients in the other directions can be neglected. In addition, heat conduction in the fluid can be ignored because it is small relative to both conduction in the rock and transport of heat with the moving fluid. These assumptions reduce the heat transfer problem to a 1D problem perpendicular to the fracture wall, with conduction through the rock to the fracture face and convection from the rock face into the fluid.

6-6.1. Historical heat transfer models

The first significant thermal model for hydraulic fracturing was published by Whitsitt and Dysart (1970). To obtain an analytical solution, they assumed a leakoff rate that varies linearly from zero at the well to a maximum at the fracture tip and accounted for the inhibiting effect of the leakoff, which occurs in the opposite direction to the heat transfer. Unfortunately, the solution they obtained contains an integral that must be evaluated numerically. Two of their more significant contributions are demonstration of the effect of temperature on acid reaction rates for acid fractures and that the temperature in much of the fracture is well below the reservoir temperature, so that fluids could be designed for lower temperatures than previously believed.

Sinclair (1971) obtained a solution to a similar problem, except that he assumed a uniform leakoff rate along the fracture. An example of the results is shown in Fig. 6-12. The significance of this figure is the relatively small fluid heat-up that occurs when the fluid efficiency is low. For an efficiency of 10%, the temperature in the fracture is approximately the inlet temperature over about 80% of the fracture length. At higher efficiencies, a more rapid heat-up occurs, so that about 50% or more of the fracture length is at or close to the reservoir temperature.

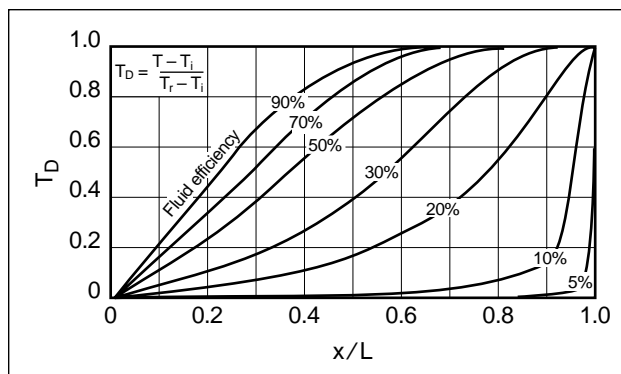


Figure 6-12. Temperature profile in a fracture for different fluid efficiencies. T_D = dimensionless temperature, T = absolute temperature, T_i = fluid temperature at the fracture mouth, T_r = reservoir temperature.

6-6.2. Improved heat transfer models

Meyer (1987) developed a solution that accounts for a finite-film, or convective, coefficient for heat transfer between the rock and the fluid and also introduced the power law Nusselt number to determine the value of the convective heat transfer coefficient. This showed that the effect of the finite-film coefficient is to reduce the rate of fluid heat-up.

Kamphuis *et al.* (1993) developed a numerical simulator that accounted for similar effects. One of the advantages of the numerical model is that it allows including more effects, such as variable pump rate during the treatment, and, of more practical importance, calculating temperature changes after shut-in. This model requires the introduction of a calculation grid in the rock.

Another algorithm has been developed to solve the heat transfer problem (see Sidebar 6I). It has many of the advantages of the numerical solution mentioned previously but is extremely computationally efficient. The equation for the fluid temperature is unconditionally stable; i.e., there is no upper limit on the time step. The results of simulation with this method compare favorably with the full numerical solution of Kamphuis *et al.* (see Sidebar 6J).

6-7. Fracture tip effects

All fracture models include the effects of rock deformation (width), mass transport and fluid loss in similar ways. However, the failure and opening of the fracture

6I. Efficient heat transfer algorithm

Mack and Elbel (1994) presented an efficient algorithm for the calculation of temperature changes in hydraulic fractures.

Consider a semi-infinite rock mass with constant surface flux F_0 starting at time zero. The temperature change of the rock surface ΔT_{surf} as a function of time t is (Carslaw and Jaeger, 1959)

$$\Delta T_{surf} = -C_0 F_0 \sqrt{t}, \quad (6I-1)$$

where

$$C_0 = \frac{2}{k_h} \left(\frac{\kappa}{\pi} \right)^{1/2}, \quad (6I-2)$$

where k_h is the thermal conductivity of a solid and κ is the thermal diffusivity of a solid.

For a piecewise constant-flux history, Eq. 6I-1 can be generalized to

$$\Delta T_{surf}^n = C_0 \sum_{i=1}^n (F_i - F_{i-1}) \sqrt{t_n - t_{i-1}}, \quad (6I-3)$$

where t_i and F_i represent the time and the surface flux, respectively, at the end of the i th time step. Thus,

$$\Delta T_{surf}^n = T_r^0 - E_n - C_0 F_n \sqrt{\Delta t_n}, \quad (6I-4)$$

where T_r^0 is the initial reservoir temperature, $\Delta t_n = t_n - t_{n-1}$, and E_n represents the effect of all previous time steps, which can be written as

$$E_n = C_0 \sum_{i=1}^{n-1} (F_i - F_{i-1}) \sqrt{t_n - t_{i-1}} - C_0 F_{n-1} \sqrt{\Delta t_n}. \quad (6I-5)$$

Now consider an element of fluid of height ∂y , length ∂x and width $w/2$ that experiences a change in temperature from T_{fl}^{n-1} at the beginning of a time step to T_{fl}^n at the end of the step. The quantity of heat required to cause this temperature change is $\rho_f C_{pfl} w \partial x \partial y (T_{fl}^n - T_{fl}^{n-1})/2$. Assuming a constant flux over time step Δt_n , this implies that the flux and temperatures over the area $\partial x \partial y$ are related by

$$(T_{fl}^n - T_{fl}^{n-1}) = \frac{F_n}{D_1} \Delta t_n, \quad (6I-6)$$

where

$$D_1 = \frac{\rho_f C_{pfl} w}{2}. \quad (6I-7)$$

Finally, consider the effect of heat transfer by convection from a rock surface at temperature T_{surf}^n to fluid at a temperature T_{fl}^n . If the heat transfer coefficient is h , the flux is

$$F_n = h(T_{surf}^n - T_{fl}^n). \quad (6I-8)$$

Equations 6I-3, 6I-6 and 6I-8 can be solved for T_{fl}^n , F_n and T_{surf}^n to yield

$$T_{fl}^n = \frac{T_r^0 - E_n + C_2 T_{fl}^{n-1}}{1 + C_2} \quad (6I-9)$$

$$F_n = \frac{D_1 (T_{fl}^n - T_{fl}^{n-1})}{\Delta t_n} \quad (6I-10)$$

$$T_{surf}^n = T_{fl}^n + \frac{F_n}{h} \quad (6I-11)$$

$$C_2 = \left(C_0 \sqrt{\Delta t_n} + 1/h \right) \frac{D_1}{\Delta t_n}. \quad (6I-12)$$

Defining D_0 as $1/C_0$,

$$T_{fl}^n = \frac{h D_0 \Delta t_n (T_r - E_n) + D_1 (h \sqrt{\Delta t_n} + D_0) T_{fl}^{n-1}}{h D_0 \Delta t_n + D_1 (h \sqrt{\Delta t_n} + D_0)}. \quad (6I-13)$$

It has been shown (Kamphuis *et al.*, 1993) that the effect of leakoff on the heat flux is equivalent to reducing the conductivity by the factor

$$\frac{\exp(-P^2)}{1 + \operatorname{erf}(P)}, \quad (6I-14)$$

where $P = C_0/\sqrt{k_h}$.

Meyer (1987) showed that the Nusselt number

$$\frac{hw}{k_f}, \quad (6I-15)$$

where k_f is the thermal conductivity of the fluid, for non-Newtonian fluids ranges from 6 for $n' = 0$ to 4.11 for $n' = 1$. A Nusselt number of 4.3 is most representative of typical fracturing fluids.

If a fracture treatment is simulated with an explicit finite difference scheme, it is not practical to retain the flux history of each solid grid point because many thousands of time steps may be required to simulate the entire treatment. It has been found that using 5 to 10 steps to represent the flux history is sufficient, provided the time steps are merged in such a way that the overall heat loss from the formation is conserved. This results in an accurate representation of the most recent temperature changes in the simulation, yet retains computational and storage efficiency.

at its tip boundary are addressed in numerous ways. Nevertheless, certain general principles can be described that apply to this region, and different implementations can be considered as modifications of the general principles. If the fracture tip is envisioned as the zone between the fracturing fluid and the undisturbed rock ahead of the fracture, then there are four possible features of this region that must be addressed:

- failure or opening process (normal LEFM)
- disturbed zone in the rock ahead of the fracture tip (damage not incorporated in the LEFM model)
- unwetted zone (fluid lag region)
- disturbed zone along the fracture face (e.g., dilatancy or compaction).

6J. Verification of efficient thermal calculations

The paper by Kamphuis *et al.* (1993) includes results for a KGD fracture in sandstone. The parameters are all held constant except for the leakoff coefficient C_L , which has values of $4E-5$, $1E-4$, $2E-4$ and $3E-4$ m/s^{1/2}. Figure 6J-1 compares the results obtained using the method described in Sidebar 6I and those obtained by Kamphuis *et al.* The dimensionless temperatures along the fracture are shown as a function of the leakoff coefficient, with the lowest curve representing the largest leakoff coefficient. The agreement is good, considering the relatively small number of elements (eight) used in this simulation and the relatively coarse nature of the heat transfer algorithm compared to Kamphuis *et al.*'s detailed finite-difference calculations.

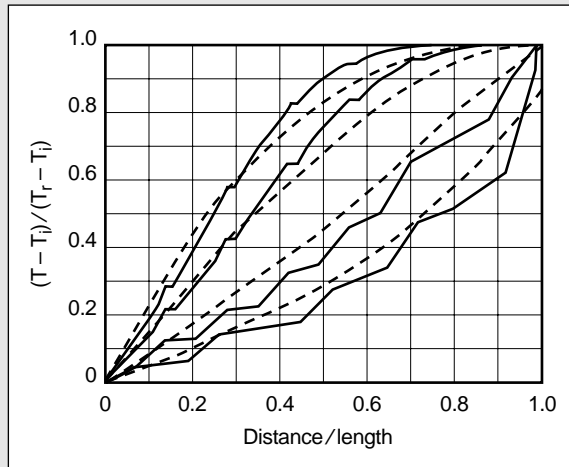


Figure 6J-1. Comparison of temperature calculations (solid lines) with the results of Kamphuis *et al.* (1993) (dashed lines).

These four mechanisms are typically neglected or handled in an ad hoc manner because of a lack of understanding and data, particularly on a field scale, about this complex zone.

6-7.1. Linear elastic fracture mechanics

Although early studies of fracture in rock used Griffith's (1921) crack theory and surface energy (Barenblatt, 1962; Perkins and Krech, 1968; Friedman *et al.*, 1972), most analyses of rock fracture are now formulated in terms of LEFM. The advantage of LEFM over earlier theories is that it incorporates, within a simple framework, some degree of dissipative energy processes, such as plastic flow and microcracking, when the zone of dissipation is small compared with the fracture length (see plateau region for K_{Ic} on Fig. 6-13). However, when this zone is not relatively small, energy-release methods should be used, as discussed in Chapter 3.

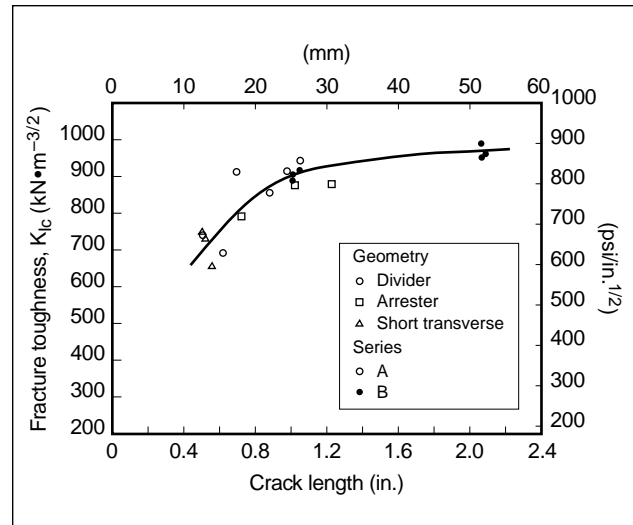


Figure 6-13. Scale dependence of fracture toughness in the laboratory (Schmidt, 1976).

• Stresses around a crack tip

Irwin (1957) identified three different types of singular stress fields (i.e., stress approaches infinity) around a crack tip and characterized these as Mode I (opening), Mode II (in plane sliding) and Mode III (antiplane sliding). For hydraulic fracture modeling, Mode I is of primary interest, although the other modes come into play in more complicated situations such as fracture turning from deviated wells. For a 2D crack opened by a constant internal pressure, Irwin showed that the stress intensity factor K_I is simply

$$K_I = \sqrt{\pi L} p_{net}, \quad (6-110)$$

where L is the crack length and p_{net} is the net internal pressure opening the crack. Similarly, for a radial crack

$$K_I = 2 \sqrt{\frac{R}{\pi}} p_{net}, \quad (6-111)$$

where R is the crack radius (see Sidebar 6K).

LEFM, as postulated by Irwin, holds that the crack will advance when the value of K_I exceeds some critical value K_{Ic} of the material, called the critical stress intensity factor. More commonly known as fracture toughness, K_{Ic} can be related to the surface energy of previous studies through

$$K_{Ic} = \sqrt{\frac{2E\gamma_F}{1-\nu^2}}, \quad (6-112)$$

6K. Crack tip stresses and the Rice equation

Irwin (1957) found that the opening mode of a 2D crack has a singular stress distribution in the near-crack-tip region:

$$\sigma_x = \frac{K_I}{\sqrt{2\pi r}} \cos(\theta/2) [1 - \sin(\theta/2) \sin(3\theta/2)] \quad (6K-1)$$

$$\sigma_y = \frac{K_I}{\sqrt{2\pi r}} \cos(\theta/2) [1 + \sin(\theta/2) \sin(3\theta/2)] \quad (6K-2)$$

$$\tau_{xy} = \frac{K_I}{\sqrt{2\pi r}} \cos(\theta/2) [\sin(\theta/2) \sin(\theta/2)], \quad (6K-3)$$

where θ is the angle measured from the crack axis, r is the distance from the crack tip, and K_I is the stress intensity factor.

By comparing the stress field given by Eqs. 6K-2 and 6K-3 with the solution of the stress field around the tip of a 2D crack extending from $-L$ to L , Rice (1968) showed that K_I can be calculated as

$$K_I = \frac{1}{\sqrt{\pi L}} \int_{-L}^L p(x) \sqrt{\frac{L+x}{L-x}} dx, \quad (6K-4)$$

where $p(x)$ is the pressure distribution in the crack. For constant pressure in the crack, Eq. 6K-4 reduces to Eq. 6-110.

For a radial crack, the equivalent equation is

$$K_I = \frac{2}{\sqrt{\pi R}} \int_0^R \frac{rp(r)}{\sqrt{R^2 - r^2}} dr, \quad (6K-5)$$

which, for constant pressure, reduces to Eq. 6-111.

where the specific fracture surface energy γ_F includes localized dissipative effects and can be determined in the laboratory, as discussed in Chapter 3. The attractiveness of this theory is its ability to include all the complicated failure processes in one parameter, which, hypothetically, is a material constant similar to modulus or strength. However, for the general case of dissipative effects, the linear elastic stresses given by Eqs. 6K-1 through 6K-3 may no longer apply near the crack tip.

- Application of fracture toughness to hydraulic fracturing in rocks

Although LEFM is attractive in its simplicity, two questions remain concerning its application to hydraulic fracturing:

- Is K_{Ic} a material property of rocks and what are its characteristics?
- Does K_{Ic} require modification for hydraulic fracturing applications?

The first question is difficult to answer because of scaling problems. In the initial application of K_{Ic} to rocks, Schmidt (1976) showed a clear size effect at small scales, but K_{Ic} appears to approach a “con-

stant” value as the crack size reaches some threshold value. Figure 6-13 shows example results for Indiana limestone that led Schmidt to conclude that K_{Ic} is a material constant. However, the small size of the laboratory samples is several orders of magnitude different than that of field-size hydraulic fractures, and size effects, which would invalidate the application of LEFM to this process, cannot be definitely ruled out.

Even without size difficulties, most rock material “constants” (such as Young’s modulus) are not constant and vary with confining stress, temperature, strain rate and the size of the rock mass tested. Similarly, in Schmidt and Huddle’s (1977) work with Indiana limestone, a significant increase of the critical stress intensity factor with confining stress was measured. Thiercelin (1987) confirmed this behavior but also showed that the amount of the increase is strongly dependent on the rock fabric and other factors.

Assuming that K_{Ic} is a material constant and scaling is not a problem, fracture toughness can be incorporated in a 2D or P3D crack model by integrating Eq. 6K-4 with the model-derived pressure distribution (or using Eq. 6-110 with a weighted-average pressure) to obtain the stress intensity factor K_I . Even an unwetted region can be included by modifying the pressure distribution used in Eq. 6K-4, as discussed later. For the calculated value of K_I :

- If K_I exceeds the input value of K_{Ic} , the crack is allowed to advance.
- If the value of K_I is less than or equal to K_{Ic} , the crack remains in its same position.
- If K_I becomes negative, the crack must retreat (i.e., the width reduces to zero) until K_I becomes ≥ 0 , as negative values indicate that the internal pressure is insufficient to support the entire crack size.

For field-size hydraulic fractures, L or R and p_{net} are so large that the stress intensity at a hydraulic fracture crack tip is much larger than typical laboratory K_{Ic} values of 500–2000 psi/in.^{1/2}. Hence, it is usually assumed that K_{Ic} for this normal crack growth process, as understood from the laboratory, is negligible except for small fractures and initial growth. The following sections discuss modifications to this theory.

6-7.2. Extensions to LEFM

In the practical application of hydraulic fracturing, the measured net pressures are usually larger than those predicted by models (Shlyapobersky, 1985, 1988a, 1988b; Cleary *et al.*, 1991). Although these high net pressures could be due to better than expected containment, poor measurement of the closure stress, near-wellbore effects, complex fracturing, poor understanding of rheology and many other factors, the general tendency has been to focus on the tip region as the source of these anomalous results. Considerable work on fracture tip effects began after Shlyapobersky (1985) suggested that hydraulic fracture data could be interpreted to show a scale effect on K_{Ic} for field-size fractures. Since then, three additional major mechanisms have been proposed to account for the high net pressures at the crack tip: fluid lag effects (Jeffrey, 1989; Gardner, 1992; Advani *et al.*, 1993), dilatancy (Cleary *et al.*, 1991) and damage (Yew and Liu, 1993; Valkó and Economides, 1993a).

- Fluid lag region

As applied to hydraulic fracturing, the unwetted zone near the crack tip has pressure less than the closure pressure and hence acts to clamp the fracture tip closed and reduce the stress intensity in the rock. This zone was first introduced by Khristianovich and Zheltov (1955) and successfully used by Geertsma and de Klerk (1969) in modeling 2D fractures. From their initial formulations, it is clear that this unwetted region could have an impact on fracture parameters if it were sufficiently large. In a simple 2D geometry, the application is straightforward, but the size of the unwetted zone and the exact pressure in the zone must be assumed. The pressure within the unwetted region is most likely the reservoir pressure for permeable rocks and could be as low as the vapor pressure of the fluid for impermeable rocks, so limits can be placed on its value. The size of the unwetted region is a more difficult problem and has been the subject of considerable investigation.

Fluid lag can be incorporated into the standard K_{Ic} form by defining an effective fracture toughness (Jeffrey, 1989):

$$K_{Ic}^{eff} = K_{Ic} + K_{Ic}^{lag}, \quad (6-113)$$

where

$$\begin{aligned} K_{Ic}^{lag} &= 2\sqrt{\frac{L}{\pi}} \int_{L-d}^L \frac{p_{tip}}{\sqrt{L^2 - x^2}} dx \\ &= 2p_{tip} \sqrt{\frac{L}{\pi}} \left[\frac{\pi}{2} - \arcsin\left(\frac{L-d}{L}\right) \right] \end{aligned} \quad (6-114)$$

for a 2D (KGD) crack, where p_{tip} is the net pressure (pressure near the tip minus the closure pressure) in the nonwetted region and d is the fluid lag distance. Typically, p_{tip} values are between $-\sigma_c + p_r$ and $-\sigma_c + p_{vapor}$, where σ_c is the closure stress, p_r is the reservoir pressure, and p_{vapor} is the vapor pressure of the fluid. The fracture propagation criterion now becomes

$$2\sqrt{\frac{L}{\pi}} \int_0^{L-d} \frac{p(t)}{\sqrt{L^2 - x^2}} dx = K_{Ic} + K_{Ic}^{lag}. \quad (6-115)$$

Similar equations can be written for radial cracks (Jeffrey, 1989).

Detailed study of the crack tip has led to the discovery of concepts unique to hydraulic fracturing. Modeling of the crack tip region by the SCR Geomechanics Group (1993; Lenoach, 1995) shows that even when effects of fracture toughness K_{Ic} are ignored, the consequences of coupled fluid flow and leakoff still result in a singularity at the crack tip. For an impermeable rock, the power of the hydraulic fracture singularity is not $\frac{1}{2}$ as for the rock behavior in LEFM, but rather $n/(2+n)$, where n is the power law index of the fluid. For permeable rocks, the power of the singularity is $3n/(4+4n)$, which is stronger than the impermeable singularity. Thus, an important singularity in stress may exist at the tip even under conditions in which the fracture toughness plays no role. They also made numerical simulations that show that the size of the fluid lag region adjusts to meet the fracture propagation criterion.

Models that determine the size of the unwetted region (Jeffrey, 1989; Gardner, 1992; Yew and Liu, 1993; SCR Geomechanics Group, 1993) generally produce small unwetted lengths, except at small confining stresses. However, only a small region is required near the tip to overshadow the effect from the fracture body. One shallow field experiment (relatively low confining stress) had sizable fluid lag zones (Warpinski, 1985), but no careful field study of fluid lag distances at higher confining stresses has been made. Fracture models where the lag distance is calculated generally show only a

small influence on global fracture parameters; a good example is calculation of the 3D aspects of the lag effect by Advani *et al.* (1993). Earlier in this chapter, it was shown that the dimension that controls fracture width is the smaller one. Hence, the KGD model is most applicable for short fractures and the PKN model for long fractures.

Advani *et al.*'s study shows that a similar effect occurs for the fracture mechanics; i.e., the length L in Eq. 6-114 must be replaced by the fracture height if the fracture length exceeds the height.

- Dilatancy

Although the LEFM concept can include small-scale damage and plasticity within its framework, the possibility exists that the damage zone around a field-size hydraulic fracture could be sufficiently large that the near-tip stress distribution becomes invalid, or other effects could alter the stress distribution. For example, Cleary *et al.* (1991) suggested that the mechanism responsible for elevating crack tip pressures is dilatancy just behind the fracture tip. They postulated that if this dilatancy occurs during the rock failure process, then the fracture width just behind the tip may be pinched slightly by the expanded fracture. Dilatation of material, which is essentially a volumetric expansion caused by failure, cannot be accommodated by the surrounding elastic material, so the rock stress in the near-tip region must increase. Yew and Liu (1993) developed a modified fracture toughness to include dilatation of the material ahead of the crack tip for the case where a plastic zone is created around the tip. An approximate equation for this behavior, in terms of an effective fracture toughness, was given as

$$K_{Ic}^{eff} = K_{Ic} + \frac{144\alpha^2}{\sqrt{3}\pi^2(1+\sqrt{3}\alpha)} \sqrt{\frac{1-\nu}{1+\nu}} \left[\frac{E - E_t}{\sqrt{EE_t}} \right] K_I, \quad (6-116)$$

where α is found by solving

$$\tan \phi = \frac{3\alpha}{\sqrt{1-12\alpha^2}}, \quad (6-117)$$

where ϕ is the friction angle and E_t is the Young's modulus of the plastic material.

Throughout the body of a fracture such dilatancy is negligible, but it could play an important role in the near-tip region, where the width is small. However, numerical simulations of crack growth, assum-

ing the rock experiences dilatant-plastic yielding, (Papanastasiou and Thiercelin, 1993) show no overall increase in the width at the fracture tip because plastic deformation dominates the dilation effect. De Pater *et al.* (1993) tried to identify dilatancy in laboratory tests and through detailed modeling of the fracture tip, but no clear evidence of such behavior was obtained.

- Other behavior: damage- and fluid-induced effects

Another approach to modeling near-tip rock behavior is to use a cumulative damage approach, in which the microcrack damage ahead of the crack forces the undamaged material to accept more of the load. Valkó and Economides (1993a) formulated a fracture model using this approach. Their model scales the damage with the fracture length, which is consistent with the KGD model and applies only to relatively short fractures. This analysis would be applicable for longer fractures if applied to a tip element or with a scaling criterion.

Because most of the modeling efforts associated with hydraulic fracturing deal with either fluid mechanics or rock mechanics, the strong chemical interactions that can affect rock behavior are often forgotten. An extreme example of this effect is the large reduction in strength that can occur as a result of stress corrosion cracking. Similarly, there has been some evidence that the chemistry, rheology or molecular structure may influence tip behavior. Holder *et al.* (1993) conducted laboratory tests in which the inferred fracture toughness values using crosslinked gels were substantially greater than those with linear gels or Newtonian fluids. Dunning (1980) found that surfactants can have a major effect on the crack propagation stress (or, alternatively, the fracture toughness). The effects of pH, total ions, and breakers and other fluid additives can cause additional chemical effects. However, these effects can influence tip failure only in the absence of a fluid lag region or where the fluid penetrates a damaged area ahead of the fracture tip.

6-7.3. Field calibration

Obtaining a definitive description of the fracture tip behavior is complex and difficult. From a practical standpoint, because the tip pressure must be consistent with field observations, its magnitude and impact can be estimated using observed pressure data, as dis-

cussed in Chapters 5 and 9. To maintain a credible description of fracture geometry, this should not be an ad hoc procedure. Shlyapobersky *et al.* (1988a, 1988b) proposed a method to calibrate a field-scale effective fracture toughness that assumes that the fracture stops growing soon after shut-in and fluid flow within the fracture stops. By determining an initial shut-in pressure (ISIP) at the time when fracture growth stops (if possible) and the closure stress in the formation, the method measures a value of p_{net} associated with an open fracture at the end of pumping. Given p_{net} , the effective fracture toughness is calculated from

$$K_{Ic}^{eff} = \alpha_g p_{net} \sqrt{R_{eff}}, \quad (6-118)$$

where R_{eff} is one-half of the fracture height for a long 2D crack or the crack radius for a penny-shaped crack, and α_g is a geometry coefficient, which depends on the geometry for a rectangular crack or is 0.64 for a penny-shaped crack.

This and other procedures to define tip effects by field calibration require an accurate measurement of p_{net} as well as reliable information on the fracture geometry (h_f , L and R), fluid flow within the fracture after shut-in and the expected nature of the rock's failure behavior.

6-8. Tortuosity and other near-well effects

High near-wellbore friction losses have been observed in fracture treatments, particularly in deviated wells or when the perforations are inadequate or poorly designed. Some attempts have been made to understand the effect of near-wellbore geometry on the placement of hydraulic fractures (Aud *et al.*, 1994) and to develop methods to prevent unplanned screenouts (Cleary *et al.*, 1993; Stadulis, 1995). Near-wellbore friction losses have been attributed to phenomena such as wellbore communication (perforations), tortuosity (fracture turning and twisting), perforation phasing misalignment and induced rock pinching, and multiple fractures (e.g., Stadulis, 1995). These effects have been identified as detrimental to the success of a fracturing treatment because of the increase in net pressure and the increased likelihood of unplanned screenouts caused by the limited fracture width near the wellbore.

6-8.1. Fracture geometry around a wellbore

Several researchers have investigated mechanisms related to fracture initiation in vertical and deviated wells. Behrmann and Elbel (1991) and Daneshy (1973) found that the perforation must be oriented within about 10° to 20° of the plane normal to the minimum far-field stress for a fracture to initiate at the perforation and extend. Other experiments show that when the perforations are not oriented in the direction of far-field fracture propagation and the well is deviated, the fractures can be nonplanar or S shaped (Weijers, 1995; El Rabaa, 1989). However, predicting the near-wellbore pressure drop in deviated wells is difficult because of the uncertainty of the near-well fracture geometry.

A symmetric bi-wing planar fracture is generally assumed to develop when a hydraulic fracture treatment is performed. Hydraulic fracture models such as the planar and P3D models described previously do not account for fracture initiation and near-wellbore effects. Apart from multiple fractures, the near-wellbore effects described here have no effect on the overall fracture geometry, except if a near-wellbore screenout is caused by near-wellbore effects. This is in contrast to fracture tip effects (see Section 6-7), which may affect fracture geometry significantly.

The purpose of modeling near-wellbore effects is twofold: to understand the source of near-wellbore screenouts, so that they may be predicted and prevented, and to correctly remove the near-wellbore contribution from the measured “net pressure” so that the remaining net pressure may be interpreted correctly as a characteristic of the overall fracture geometry.

6-8.2. Perforation and deviation effects

The three assumed components of near-wellbore pressure loss are friction through the perforation, fracture turning (i.e., tortuosity) and perforation misalignment friction, which are also assumed to be additive:

$$\Delta p_{near\ wellbore} = \Delta p_{pf} + \Delta p_{tort} + \Delta p_{misalign}. \quad (6-119)$$

It is not possible to predict near-wellbore effects, other than friction through perforations. Rather, models for these mechanisms of pressure increase are provided, and each mechanism has one or more parameters, which can be evaluated from field data.

6-8.3. Perforation friction

A discussion of perforating requirements for hydraulic fracturing is in Chapter 11. Insufficient or poor perforations can have a significant effect on the execution and evaluation of a fracturing treatment because they affect the breakdown and treating pressure. Improper perforating can result in near-wellbore screenouts if the perforations do not provide an adequate pathway to the main body of the fracture. The equation commonly used to calculate perforation friction implicitly assumes that the perforation is a short cylindrical tunnel (McClain, 1963):

$$\Delta p_{pf} = 0.2369 \frac{q^2 \rho}{n^2 D_p^4 C^2}, \quad (6-120)$$

where q is the total flow rate, ρ is the fluid density, n is the number of perforations, D_p is the perforation diameter, and C is the discharge coefficient. The discharge coefficient represents the effect of the perforation entrance shape on the friction pressure.

The effect of perforation friction on fracture treating pressure is usually negligible if the perforations are correctly sized and phased. If this is not the case, perforation friction is assumed to be constant during the entire treatment. When sand slurries are pumped at high differential pressure across the perforations, the pressure drop changes, owing to erosion. There are two effects of erosion on the pressure drop through a perforation: smoothing of the entrance of the perforation, with a resulting increase in the discharge coefficient C , and an increase in diameter D_p . Figure 6-14 shows the related evolution of the coefficient of discharge with the perforation geometry (Crump and Conway, 1988). These effects, and their implementation in a fracture simulator, are described in more detail in Romero *et al.* (1995).

Figure 6-15 illustrates the difference between the resulting pressure responses when perforation friction and erosion are included in the calculation and when they are neglected for a PKN geometry model. The pressure increases as expected for a confined fracture, until proppant reaches the perforations. Then the pressure decreases, mainly because of the increase in the discharge coefficient. After about 2000 lbm of sand is injected, the slope becomes positive again, almost paralleling the slope prior to the sand, which indicates a constant discharge coefficient and a slow increase of the perforation diameter.

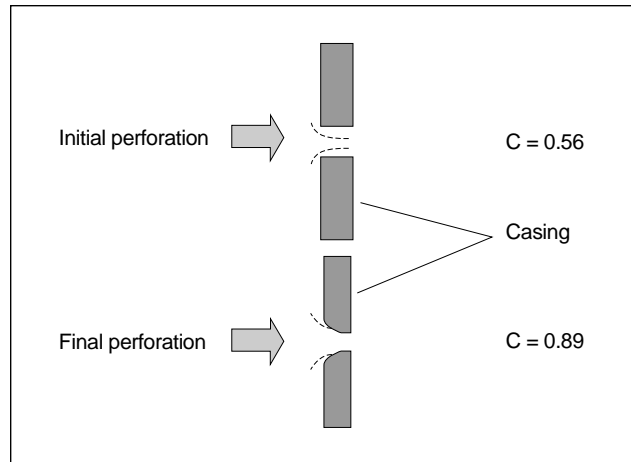


Figure 6-14. Evolution of the coefficient of discharge C with the erosion of entrance (Crump and Conway, 1988).

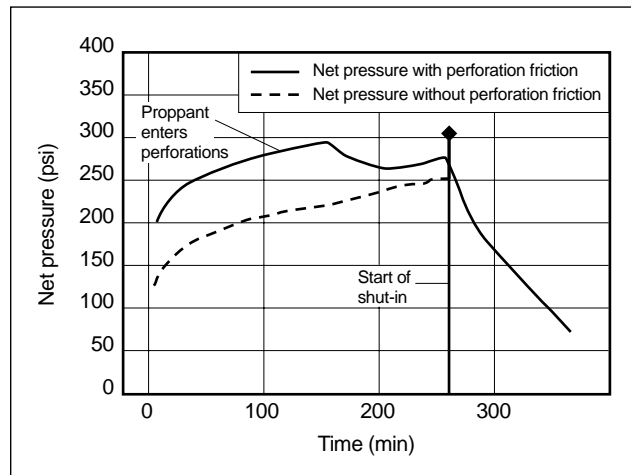


Figure 6-15. Effect of perforation friction on measured net pressure.

6-8.4. Tortuosity

Tortuosity is defined here as a convoluted pathway connecting the wellbore to the main body of the fracture. Several studies (Aud *et al.*, 1994; Cleary *et al.*, 1993) have identified tortuosity as an important phenomenon that could affect the execution of a fracture treatment when the wellbore and stress fields are misaligned. The simplified schematic of fracture geometry in Fig. 6-16 shows how a fracture may turn and twist to align itself with the preferred fracture plane.

The fracture width is proportional to the difference between the pressure in the fracture and the stress against which the fracture opens. When the fracture

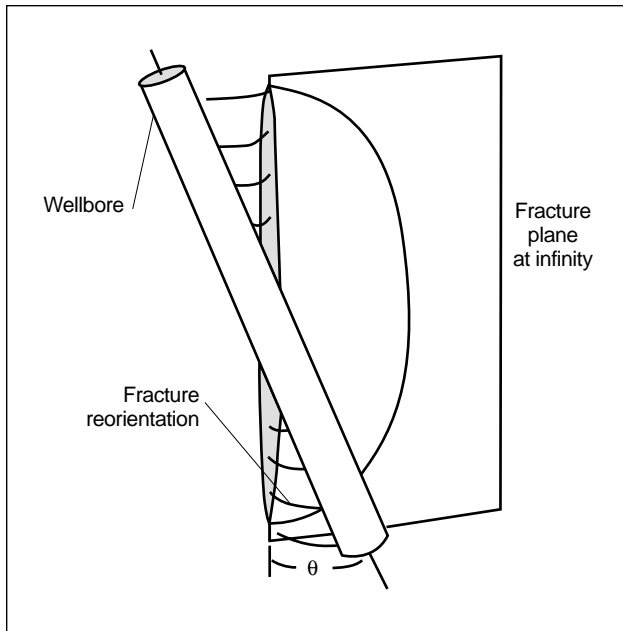


Figure 6-16. The fracture twists and turns to align itself with the preferred direction of propagation.

is opening against a stress higher than the minimum in-situ stress, the fracture width is reduced relative to that without turning. If the ratio between the stress against which the fracture is opening and the minimum in-situ stress is higher than about 1.5, the fracture mouth acts as a nozzle, allowing fluid to enter, but with a large pressure drop associated with the pinching of the fracture width at the well. This process of fracture width reduction along the reorientation path restricts flow and could cause near-wellbore screenouts.

The radius of curvature R of the reorientation path can be determined for a Newtonian fluid as (Romero *et al.*, 1995)

$$R = \lambda \sqrt{\frac{E^3 \mu q}{h_f} \left(\frac{1}{\sigma_{h,min} (\kappa - 1)} \right)^2}, \quad (6-121)$$

where λ is an experimental coefficient, q is the flow rate, $\sigma_{h,min}$ is the minimum horizontal stress, and κ is the ratio between the stress against which the fracture is opening and the minimum stress. The coefficient λ is obtained from experimental data (e.g., Abass *et al.*, 1994) or field data and can be considered a fitting parameter.

Fracture simulators such as the planar or P3D simulators discussed previously represent the behavior of the main body of the fracture, but an additional component is required to represent the tortuosity. A model

of the curved path is attached to the main body of the fracture. Equation 6-121 is used to define the shape of the path, and the outer boundary conditions (i.e., width and pressure at the end of the tortuous region) are the conditions at the wellbore, obtained from the simulator without tortuosity. Although the calculated pressure at the well may be higher than that predicted when tortuosity is neglected, the width may be lower because the stress against which the fracture is opening is higher. This may result in screenouts caused by near-wellbore bridging, which can be accounted for in the model by preventing proppant from entering if the width is too small.

The effect of tortuosity is largest near the beginning of the treatment and decreases as the treatment proceeds. This occurs because an increment in the closure stress, relative to that on a planar fracture, has a fixed absolute effect (Δw) on the width w . However, the pressure drop is, roughly speaking, inversely proportional to the width cubed, so that a change in width from w to $w - \Delta w$ has a much greater effect when w is small (i.e., when the fracture is first created). The model also shows that the pressure drop caused by tortuosity can be reduced by increasing the fluid viscosity, which has been reported in practice (Aud *et al.*, 1994) as an effective means of preventing near-well screenouts. Both added pump time prior to the introduction of proppant (i.e., increased pad) and increased viscosity may reduce near-wellbore screenouts because they cause the width to be greater in the tortuous region than it would have been. However, these treatment changes can be detrimental to height confinement and proppant placement and permeability in the resulting fracture, so other approaches to mitigate the cause of tortuosity should be considered.

6-8.5. Phasing misalignment

Perforating practices (i.e., hole size, spacing and orientation) vary widely. In general, not all the perforations in a well are aligned with the preferred fracture plane. Indeed, it would be quite coincidental for this to be the case, unless special efforts are made to obtain reliable information on the stress directions at a particular well. If 0° phasing is used, the orientation of the perforation to the plane of the hydraulic fracture may be as large as 90° . On the other hand, nearly perfect alignment or 0° phasing causes preferential propagation of one wing of the fracture with limited

penetration of the companion wing because of the pressure drop resulting from flow around the annulus to the nonconnected wing.

Nolte (1988a) pointed out that if the fracture does not initiate at the perforations, the fluid must communicate with the fracture through a narrow channel around the side of the casing. This channel can cause higher treating pressures because of the width restrictions (Fig. 6-17). As with the tortuosity effect discussed previously, this can cause both increased pressure and screenouts because of proppant bridging. Also, proppant may erode the restrictions. The circle in Fig. 6-17 represents a relatively stiff wellbore (casing and cement). If the fluid exits the well through the perforation, it must traverse the microannulus and pass the restriction area before entering the main body of the fracture. A geometry effect occurs as the rock is displaced by a distance w away from the cement, resulting in a channel around the annulus with a width of $w^2/8D$ at the fracture entrance (point A in the figure), where w is the fracture width and D is the wellbore diameter. In addition, an elastic response (Poisson's effect) occurs in which the fracture opening results in movement of the rock toward the wellbore, reducing the fracture width.

Figure 6-18 shows the displacement (in the direction of the fracture) obtained around the wellbore for a typical case in which the microannulus and fracture are subject to a constant fluid pressure. The negative displacement of the rock at the intersection between the wellbore and the fracture represents the wellbore pinching from the net pressure in the fracture (Poisson's effect). To maintain flow into the fracture through the pinch point, the microannulus must be pressurized to a higher level than the fracture. Figure 6-19 shows the pinching displacement when the net pressure varies

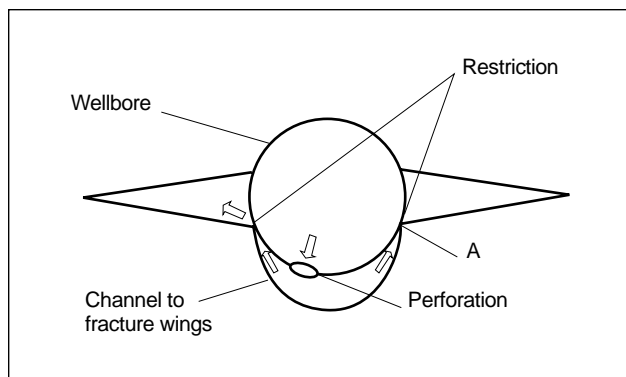


Figure 6-17. Nonalignment of perforations and the fracture plane causes pinch points.

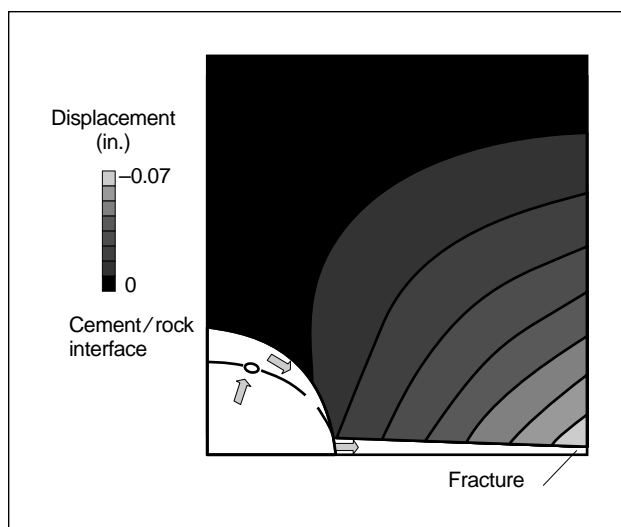


Figure 6-18. The displacement field around a fracture shows a tendency to pinch closed at the wellbore.

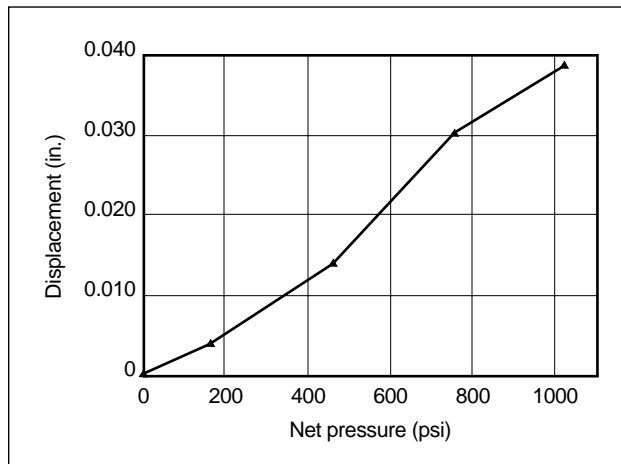


Figure 6-19. Evolution of wellbore pinching with increasing net pressure.

from 0 to 1000 psi for a typical case. The effect increases as fracturing pressure increases, in contrast to the tortuosity effect, which decreases as pressure and width increase.

If the pinch point is present when proppant attempts to enter the fracture, bridging may occur, resulting in premature screenout. The fluid travels through the pinch point at a high velocity, and either fluid or slurry may erode the pinch point, provided this occurs before bridging. The degree of erosion is affected by the viscosity of the fluid, proppant concentration and rock strength. The reported effectiveness of proppant slugs (Cleary *et al.*, 1993; Stadulis, 1995) may be due to this erosion. Because the slugs are small, they do

not bridge everywhere, so fluid entry at higher velocity continues and erodes some channels. Even prior to the use of slugs, it was common to inject proppant at low concentration to erode restrictions when high pressures occurred during the fracture initiation stage. In contrast to tortuosity, pinching is increased by large pads and higher net pressures. This may explain why, in some cases, prepad slugs can be injected at low net pressures when the pinching is smaller, but in the main treatment a near-well screenout occurs.

6-9. Acid fracturing

Hydraulic fracturing with acid (usually hydrochloric acid [HCl]) is an alternative to propped fractures in acid-soluble formations such as dolomites and limestones. The major difference between acid and propped fractures is that conductivity is obtained by etching the fracture faces instead of by using a proppant to prevent the fracture from closing. Acid fracturing may be preferred operationally because the potential for unintended proppant bridging and proppant flowback is avoided. However, designing and controlling the depth of penetration of the live acid into the formation and the etched conductivity are more difficult than controlling proppant placement. Acid penetration is governed by the chemical reaction between the rock and the fracturing fluid (as opposed to a simple mass balance in propped fractures), and conductivity is determined by the etching patterns formed by the reacting acid (as opposed to being a property of the proppant under a given stress). In both cases, acid fracturing introduces a dependence on rock properties that is not present in propped fracturing. In addition, the properties that acid fracturing design and control depend on are usually more difficult to determine than other formation properties.

The geometry of acid fractures can be determined by the same models used for propped fractures, with the exception of the impact of etched width on the width-pressure relation. However, several additional aspects of acid fracturing must be considered:

- acid transport to and reaction at the rock surface
- heat transfer, because the reaction releases heat, and the reaction rate is temperature sensitive
- leakoff, because acid leakoff behavior is significantly different from that of nonreactive fluids.

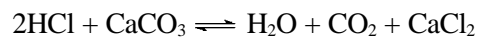
6-9.1. Historical acid fracturing models

Williams *et al.* (1979) provided a detailed discussion of acid fracturing models prior to 1980, and Li *et al.* (1993) reviewed some of the more recent work. One of the main drawbacks of most of the early models was that the fracture geometry calculation was separated from the acid reaction calculation to develop analytically tractable solutions. Since then, computer-based models have overcome these limitations, and the preceding models are no longer used. For example, Settari (1993) presented a detailed description of a comprehensive model with the fracture geometry and acid reaction calculations coupled, including a comprehensive leakoff model, coupled heat transfer and the capability to include multiple fluids with varying rheology.

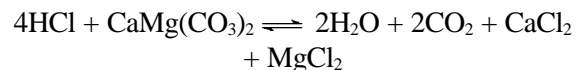
Much of what follows is based on the work described by Settari. Roodhart *et al.* (1993) presented a model in which they developed the heat transfer calculations extensively, using the work of Kamphuis *et al.* (1993). The other factor they included was the effect of the boundary layer thickness for acid reaction developing as the fluid enters the fracture, resulting in a thinner layer near the well and causing a higher etching rate. The aforementioned publications contain extensive lists of references.

6-9.2. Reaction stoichiometry

The main chemical reactions of interest in acid fracturing are those between HCl and calcium carbonate (limestone) or calcium-magnesium carbonate (dolomite). The chemical reaction for limestone is written as



and for dolomite as



The first reaction equation indicates that two molecules of HCl react with one molecule of calcium carbonate to form one molecule each of water, carbon dioxide and calcium chloride. The second equation shows that four molecules of HCl react with one molecule of calcium-magnesium carbonate to form two molecules each of water and carbon dioxide and one each of calcium chloride and magnesium chloride.

These so-called stoichiometric equations allow computing the volume of rock dissolved by a given volume of acid. These equations can be used to determine the dissolving power X_C of the acid, which is the volume of rock dissolved per unit volume of acid reacted. The mass dissolving power (i.e., the mass of rock dissolved per unit mass of acid reacted) is first defined as

$$\beta = \frac{(\text{molecular weight of rock}) \times (\text{rock stoichiometric coefficient})}{(\text{molecular weight of acid}) \times (\text{acid stoichiometric coefficient})} \quad (6-122)$$

For the limestone reaction,

$$\beta = \frac{100.09 \times 1}{36.47 \times 2} = 1.372 \quad (6-123)$$

so that each gram of 100% pure HCl dissolves 1.372 g of rock. To obtain the dissolving power, the masses must be converted to volumes:

$$X_C = \frac{\rho_C \beta C}{\rho_{CaCO_3}}, \quad (6-124)$$

where ρ_C and ρ_{CaCO_3} are the densities of the acid solution and calcium carbonate, respectively, and C is the weight-fraction concentration (e.g., 0.28 for 28% acid). For example, the specific gravity of 28% acid is 1.14, whereas that for 15% acid is 1.07. A complete table of densities is in Williams *et al.* (1979). Applying this calculation for the limestone-HCl reaction, X_{15} is 0.082, and X_{28} is 0.161. Similarly, for dolomite the values are 0.071 and 0.141, respectively.

The stoichiometric equations for acid reactions provide a relation for the coupling between fracture geometry and acid spending. Because there are many unknowns in acid fracturing, the modeling can be simplified by neglecting the variation in density of the acid and using that of 10% acid, which is a suitable average for most acid fracture treatments. In this case, X_{100} can be approximated as $10X_{10}$ and X_C as CX_{100} . Now, consider the volume of a fracture element of cross-sectional area (width times height) A and length δx in which the acid concentration changes by an amount ΔC . The volume of acid spent is $A \cdot \delta x \cdot \Delta C$, and the volume $\Delta A \cdot \delta x$ of rock dissolved is

$$\Delta A_{etch} = X_{100} A \Delta \bar{C}, \quad (6-125)$$

where A_{etch} is the etched area and \bar{C} is the average acid concentration in the cross section.

6-9.3. Acid fracture conductivity

Acid fracture conductivity is much more poorly understood than propped fracture conductivity. The flow rate through an open channel of width w is proportional to w^3 . If the etched channel were under no stress, this proportional relation would be used to determine the conductivity of an acid fracture. However, the stress in the reservoir acts to close the channel. If the etching were completely uniform, this closing could be calculated in a manner similar to that used to calculate the width of an elliptical fracture, except that the net pressure is negative. As an approximation, for a uniform etched width, the shape of the resulting closed fracture would be

$$w(z) = w_{etch} - \frac{4\sigma_c}{E'} \sqrt{h_f^2 - z^2}, \quad (6-126)$$

where w_{etch} is the etched width, and the width is set to zero wherever Eq. 6-126 predicts a negative width. It is apparent from this equation that the width in most of the channel would be much lower than that of an open channel, as most of the channel would have closed completely. This would clearly reduce fracture conductivity significantly.

Fortunately, acid etches the rock surface in a non-uniform manner, because of rock heterogeneity and fingering of the acid through the wider previously etched channels. This results in numerous horizontal “pillars” supporting the channels between them, for which Eq. 6-126 could be used with the fixed fracture height h_f replaced by the distance between the pillars. It is not practical to model this in detail, because the pattern is not generally known. Because conductivity is higher in formations where numerous small channels occur supported by numerous pillars, uniform etching is not desirable. If, however, the pillars lack the strength to support the additional load required to keep the channels open, some of the pillars will collapse, reducing the conductivity. Fracture conductivity is thus dependent not only on the etching pattern, but also on the rock strength and closure stress. Nierode and Kruk (1973) developed an empirical equation for conductivity:

$$(wk)_{eff} = C_1 \exp(-C_2 \sigma), \quad (6-127)$$

where

$$C_1 = 0.265 wk_{fi}^{0.822} \quad (6-128)$$

$$C_2 = \begin{cases} (13.9 - 1.3 \ln S_{RE}) \times 10^{-3} & 0 \text{ psi} < S_{RE} < 20,000 \text{ psi} \\ (3.8 - 0.28 \ln S_{RE}) \times 10^{-3} & 20,000 \text{ psi} < S_{RE} < 500,000 \text{ psi} \end{cases} \quad (6-129)$$

$$wk_{fi} = 9.36 \times 10^{13} \left(\frac{w_{etch}}{12} \right)^3, \quad (6-130)$$

where σ is the effective stress in psi, S_{RE} is the rock embedment strength in psi, and wk_{fi} is the conductivity in md-in. A typographical error in the original paper is corrected in Eq. 6-129.

6-9.4. Energy balance during acid fracturing

The total heat generated (per unit volume) by a change in acid concentration $\Delta \bar{C}$ is $\Delta \bar{C} \Delta H$, where ΔH is the heat of reaction. Coupling of the acid and heat transfer models is provided by assuming that all the heat initially increases the fluid temperature, resulting in a fluid temperature change of

$$\Delta T_{fl} = \frac{\Delta \bar{C} \Delta H}{\rho_f C_{pfl}}, \quad (6-131)$$

where ρ_f is the fluid density and C_{pfl} is the fluid heat capacity. Section 6-6 describes how heat is transferred between the fluid and the formation. The magnitude of the temperature change resulting from acid reaction may be sufficient to cause the temperature of some fluids to exceed the reservoir temperature. It is thus particularly important to use a numerical temperature calculation when simulating acid fracturing.

6-9.5. Reaction kinetics

Surface reactions such as the acid-rock reactions discussed here are complex, even under laboratory conditions. In general, the liquid-phase reaction between species A and B to form products C and D is governed by an expression of the form

$$r = \xi_f a_A^{n_A} a_B^{n_B} - \xi_r a_C^{m_C} a_D^{m_D}, \quad (6-132)$$

where ξ_f is the forward rate constant, ξ_r is the reverse rate constant, and a_X represents the chemical activity of species X. In the reactions of interest in acid fracturing, reverse reactions are usually much slower than forward reactions and can be neglected. In very dilute systems, the chemical activity is equal to the concentration. It is also usually observed that the reaction

rate constants are functions of temperature, following the Arrhenius equation:

$$\zeta_f^T = \zeta_f^{T_{ref}} \exp \left(\frac{-\Delta E}{R} \left(\frac{1}{T} - \frac{1}{T_{ref}} \right) \right). \quad (6-133)$$

The acid reaction rate at a surface is thus a complex function of the activities of all species involved in the reaction. Detailed modeling of the reaction in terms of these activities is not required for a hydraulic fracture simulator, because of the large amount of uncertainty in the other parameters. Instead, the reaction rate can be assumed to be governed by the simple equation for the rate of acid consumption r (Settari, 1993):

$$r = \frac{\partial M_{acid}}{\partial t} = -K_r (C_{wall} - C_{eqm})^m, \quad (6-134)$$

where the temperature-dependent reaction rate constant is

$$K_r = k_0 \exp \left(\frac{-\Delta E}{R} \left(\frac{1}{T} - \frac{1}{T_{ref}} \right) \right), \quad (6-135)$$

where M_{acid} is the moles of acid per unit rock face area, t is the time, C_{wall} is the surface acid concentration, C_{eqm} is the equilibrium concentration, m is the order of reaction, k_0 is the reaction rate constant at the reference temperature T_{ref} (298K [25°C]), ΔE is the activation energy, R is the universal gas constant, and T is the absolute temperature.

C_{eqm} is generally zero for the reactions of interest.

6-9.6. Mass transfer

Before the reaction can occur at the fracture wall, the acid molecules must be transported to the wall. In a stagnant fluid, diffusion in an ideal case can be described by Fick's law:

$$v_{A,x} = -D_A \frac{\partial C_A}{\partial x}, \quad (6-136)$$

where $v_{A,x}$ is the velocity of species A, D_A is the molecular diffusion coefficient, C_A is the acid concentration, and the derivative represents the concentration gradient. Williams *et al.* (1979) proposed accounting for leakoff by adding a term to the right-hand side of Eq. 6-136, resulting in

$$v_{A,x} = -D_A \frac{\partial C_A}{\partial x} + C_A u_L. \quad (6-137)$$

In flowing fluids, this equation is no longer valid, because acid transport is by convection rather than diffusion. For acid fracture modeling, Eq. 6-136 is simply replaced by

$$v_{A,x} = K_g (C_A - C_{wall}) + (C_A - C_{wall})u_L, \quad (6-138)$$

where the mass-transfer coefficient is

$$K_g = D_{eff} N_{Sh} / w, \quad (6-139)$$

where D_{eff} is the effective acid diffusion coefficient. The Sherwood number N_{Sh} is determined from the correlation (Lee and Roberts, 1980)

$$N_{Sh} = \begin{cases} 6.26 N_{Sc}^{1/3} & N_{Re} < 1800 \\ 0.001104 N_{Re}^{1.153} N_{Sc}^{1/3} & 1800 < N_{Re} < 7000, \\ 0.026 N_{Re}^{4/5} N_{Sc}^{1/3} & N_{Re} > 7000 \end{cases} \quad (6-140)$$

where the Reynold's and Schmidt numbers are defined respectively by

$$N_{Re} = \frac{2wv\rho_f}{\mu} \quad (6-141)$$

$$N_{Sc} = \frac{\mu}{D_{eff}\rho_f}. \quad (6-142)$$

6-9.7. Acid reaction model

If reaction occurs, the acid concentration varies across the fracture width, and the surface concentration is less than the bulk acid concentration. The surface concentration is such that the amount consumed at the surface is balanced by transport to the surface by diffusion.

The wall concentration for a given bulk concentration is obtained by equating the right-hand sides of Eqs. 6-134 and 6-138 to obtain

$$K_r (C_{wall} - C_{eqm})^m = (K_g + u_L)(\bar{C} - C_{wall}). \quad (6-143)$$

This equation, which is a general model of acid reaction, can easily be solved if $m = 1$ but is solved iteratively otherwise. If K_r is very large compared with $K_g + u_L$, then Eq. 6-143 is satisfied when C_{wall} is approximately equal to C_{eqm} . In this case, C_{eqm} can replace C_{wall} on the right-hand side of Eq. 6-143, and Eq. 6-138 can be written as

$$r = \frac{\partial M_{acid}}{\partial t} = -(K_g + u_L)(\bar{C} - C_{eqm}). \quad (6-144)$$

In this case, the reaction rate is termed mass-transfer limited, because the rate at which it occurs is controlled by the rate at which live acid can be brought to the rock surface. Similarly, if $K_g + u_L$ is very large compared with K_r , then Eq. 6-143 is satisfied when C_{wall} is approximately equal to \bar{C} . In this case, \bar{C} can replace C_{wall} on the left-hand side of Eq. 6-143, and Eq. 6-134 can be written as

$$r = \frac{\partial M_{acid}}{\partial t} = -K_r (C_{wall} - C_{eqm})^m. \quad (6-145)$$

Equation 6-145 represents the reaction-rate- or kinetics-limited case in which the rate of acid consumption is limited by the rate at the wall.

6-9.8. Acid fracturing: fracture geometry model

The movement of acid perpendicular to the fracture wall is considered in this section. The preceding sections discuss the fluid flow equations typically solved in fracture models. Acid movement within the fracture can be modeled similarly to the movement of proppant. For a fracture simulator to simulate acid fracturing treatments accurately, several specific requirements must be met relating to

- fluid tracking in the fracture and reservoir
- recession of the active fracture length
- effect of etching on the relation between pressure and width.

Although typical fluid flow calculation schemes use a coarse grid (about 10 elements), accurate fluid front tracking can be obtained only by following up to 50 fluid stages. Typical treatments include only about 10 different stages, but stages can be subdivided for better tracking of the large gradients that may occur in acid concentration within a single stage. Also, a finer grid is required to track leakoff volumes into the formation and formation exposure to fluid stages for accurate modeling of the extreme differences in leakoff characteristics and viscosity between acid and nonacid stages.

Acid fracturing treatments are typically designed with sudden changes in flow rate because the different fluids in the treatment have significantly different frictional properties. These sudden changes, as well as the high leakoff that may occur during pumping of the

acid stages, may cause recession of the active fracture length. The simulator must model this recession, which seldom occurs in proppant treatments.

For a confined fracture in a homogeneous isotropic elastic material, the relation between the net pressure and cross-sectional area A can be written as

$$p_{net} = \frac{2E'}{\pi h_f^2} A. \quad (6-146)$$

A modification to this relation is required to account for dissolution of the rock by acid. Only the elastic area A_{elas} contributes to the net pressure in the fluid, although the total area A (where $A = A_{elas} + A_{etch}$) is available as a flow channel and to store the fluid mass.

Mack and Elbel (1994) presented example problems illustrating the effects of some of the features of acid fracturing models.

6-10. Multilayer fracturing

Many fracture treatments are performed in settings that result in the formation and extension of nearly isolated fractures in different zones. Frequently it is desirable to fracture multiple zones simultaneously, because treatment of each zone separately would not be practical or would be significantly more expensive. However, the design of treatments for multiple zones requires some special considerations. For example, the amount of each fluid stage entering each zone cannot be controlled by the engineer. Fluid partitioning is important, because it dictates the size of the individual fractures formed. In addition, if the partitioning is unfavorable, premature screenouts may occur in some zones.

Some early work on the propagation of multiple fractures (Lagrone and Rasmussen, 1963; Ahmed *et al.*, 1985; Cramer, 1987; Ben Naceur and Roegiers, 1990) considered fluid partitioning in a limited way (e.g., using a limited representation of the formation or at only a single point in time). In the method described in this section, fluid partitioning is calculated throughout the treatment.

To simulate the simultaneous propagation of multiple fractures, a single-fracture model (either analytical or numerical) is integrated with a set of constraints coupling the individual fractures. For the present, it is assumed that the individual fractures are well separated, with no mechanical interaction or any fluid flow between fractures except via the well. In this case, the fractures can be represented as in Fig. 6-20. Fractures

may open and propagate in n layers. At any time, the sum of the flow rates into all layers must equal the total injection rate. In addition, the sum of the closure stress in a zone plus the pressure drops through the path from the tip of the fracture in that zone to a reference point in the well must be the same for each fracture. This set of conditions can be expressed as

$$q_i = \sum_{j=1}^n q_{i,j} \quad (6-147)$$

$$p_{ref} = \sigma_{c,j} + \Delta p_{w,j}(q_{i,j}) + \Delta p_{near\ wellbore,i}(q_{i,j}) - p_{h,j} + p_{cf,j}(q_{i,j}), \quad (6-148)$$

which is applied for each fracture. The terms on the right-hand side of Eq. 6-148 represent the closure stress, pressure drop in the fracture, pressure drop in the near-wellbore region including the perforations, hydrostatic pressure and casing friction, respectively. There are thus $n + 1$ unknowns (n flow rates $q_{i,j}$ and reference pressure p_{ref}) and $n + 1$ equations describing the system. Equation 6-148 is highly nonlinear, but the system can nevertheless be solved by standard techniques, as shown by Elbel *et al.* (1992).

Figure 6-21 shows an example of a multilayer fracture treatment modeled as a set of PKN fractures. The fluid partitioning was measured using a spinner flowmeter, and the downhole pressure was recorded. The model accurately captures the behavior of the system.

Figure 6-22 shows a more complex case. The effect of a screenout in a layer reduces the flow into that layer while increasing it into others. Another interesting effect that the model shows is the effect of crossflow, in which fluid may flow between fractures after pumping ends. If this rate is excessive, proppant may be drawn out of one or more fractures and that flush fluid may be injected into other fractures, impairing near-wellbore fracture conductivity. The crossflow also violates the assumptions of pressure decline analysis, possibly resulting in an incorrect estimate of fluid loss.

Extension of the model to cases with height growth was reported by Mack *et al.* (1992). They showed that significant differences in both fracture geometry and flow partitioning can occur if the P3D representation is used for the individual fractures, because fracture height growth changes the relation between net pressure in the fracture and the flow rate into the fracture. Figure 6-23 shows an example comparing the pressure response and the resulting fracture geometry. In

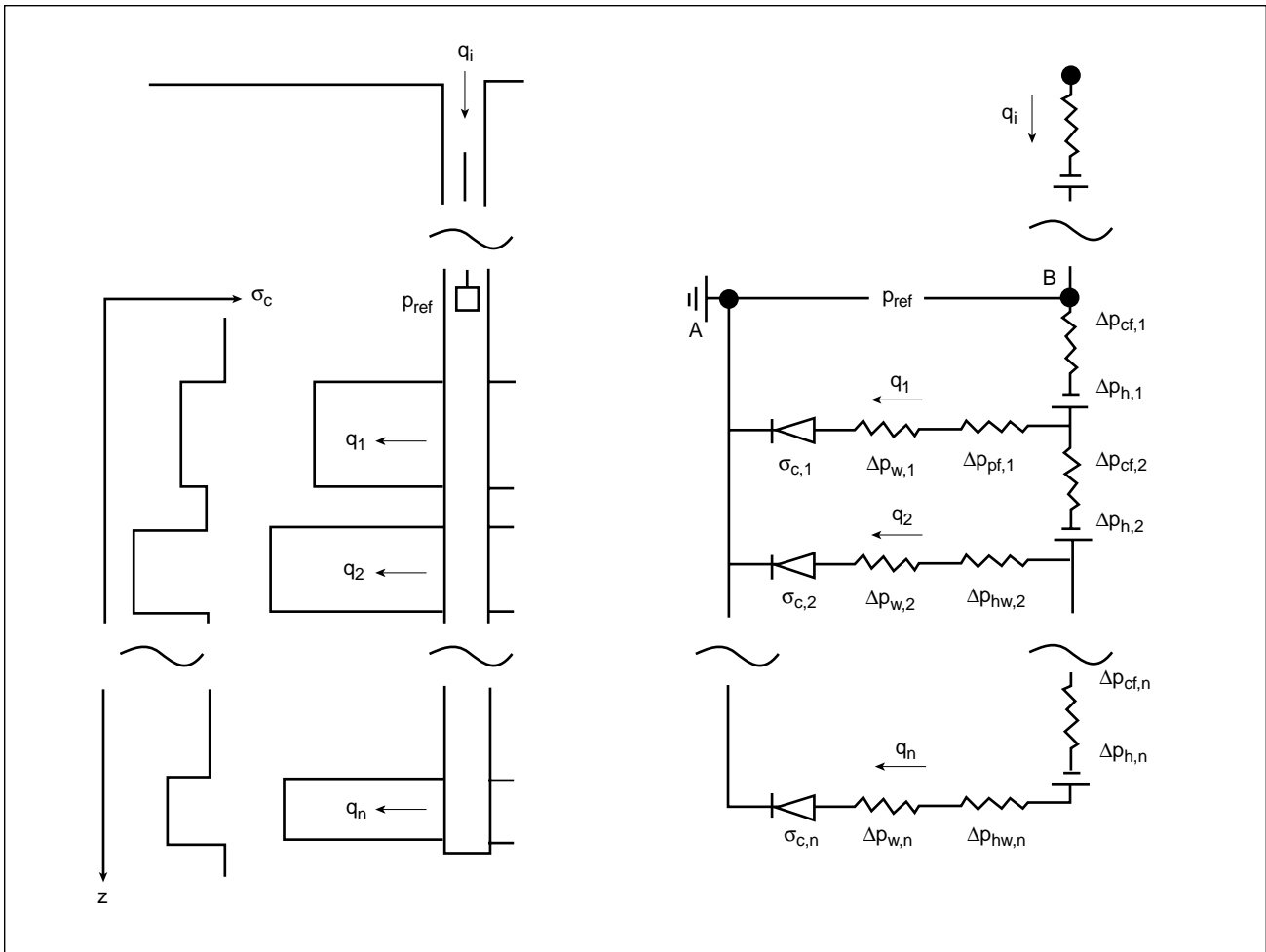


Figure 6-20. Relationships for multiple fractures propagating simultaneously.

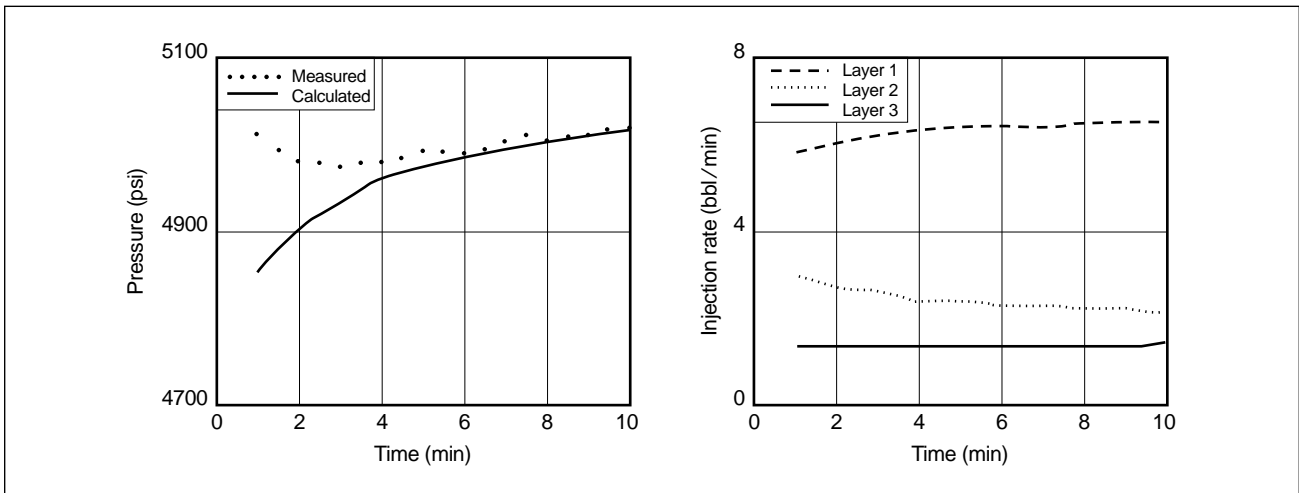


Figure 6-21. Multilayer fracture treatment modeled as a set of PKN fractures.

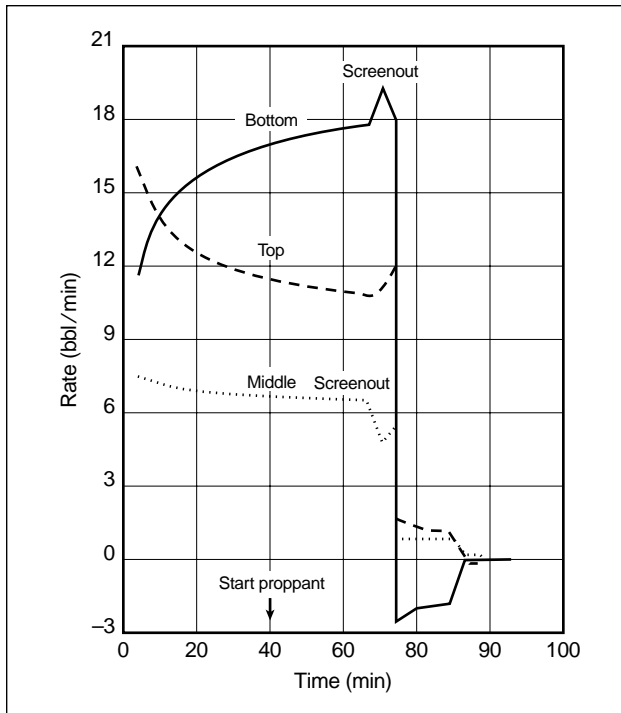


Figure 6-22. Fluid rate into three fractures, showing effects of screenout and crossflow.

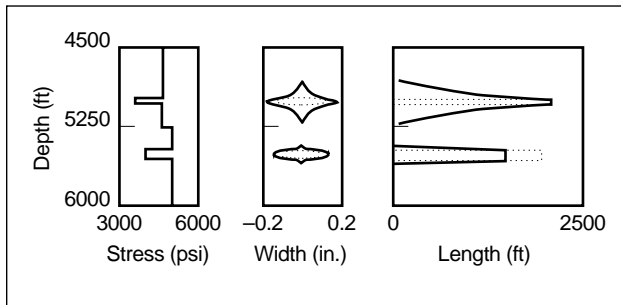


Figure 6-23. Pressure response and geometry of fractures modeled with the P3D model.

general, the multiple fractures would not connect into a continuous fracture unless the wellbore were perfectly aligned (e.g., $<2^\circ$) with the minimum stress directions. Except for this rare case, height growth would be inhibited after the tips overlapped.

6-11. Pump schedule generation

It is time consuming to design the schedule required to achieve a fracture of desired length and proppant concentration. One way to simplify the task is to use

an analytical solution such as that described in Sidebar 6L. However, the analytical solutions are generally applicable only for simple (i.e., radial, PKN or KGD) models. Another alternative is to develop a pump schedule generator that uses a numerical simulator. This tool uses the simulator in a so-called inverse mode to determine the schedule. It requires all the formation and fluid data necessary for a forward simulation. Instead of the schedule, however, the desired propped length, minimum and maximum proppant concentrations, and step in concentration between stages are specified. A typical concentration range could be 2 ppg minimum to 12 ppg maximum, with steps of 2 ppg.

To obtain the desired schedule, the simulator is started with a schedule derived from an analytic approximation or a schedule with a small pad stage and an arbitrarily sized slurry stage with the maximum proppant concentration. As the simulation proceeds, the simulation software monitors the leakoff of individual fluid elements in the fracture. As the fluid leaks off, the proppant concentration increases. If the user-specified maximum is exceeded, the simulator adjusts the proppant concentration down to the maximum value and keeps track of how much proppant has to be “converted” conceptually to fluid to maintain this. In addition, the fracture length is tracked and the schedule continually extended until the user-specified length is reached. When the desired length is reached, it is relatively simple to determine how much proppant (if any) is left in each fluid element. This represents the amount of proppant that should be in that element when pumped, providing a design proppant schedule. If proppant does not reach the fracture tip (i.e., some of the pad should have been slurry), this can be accounted for.

There are two issues that make this process more complex than as described. First, as previously noted, proppant affects fluid rheology, so modification of the amount of proppant during the simulation affects the fracture length. This is minimized by repeating the calculation with the schedule generated by the previous iteration as input. Three iterations are usually sufficient to converge on a suitable schedule. A more critical issue is that this method cannot easily account for bridging. Except during the initial small pad stage, there is always proppant everywhere in the simulated fracture, although some of it may later be converted to fluid. Bridging is therefore ignored and accounted for

6L. Approximate proppant schedules

K. G. Nolte
Schlumberger Dowell

The facility to approximate proppant schedules for routine and tip screenout (TSO) designs based on fluid efficiency (Nolte, 1986b) is an important design tool. For a specified amount of fluid or proppant, the technique requires an efficiency estimate for the proppant treatment that can be determined from a fracture calibration treatment after an appropriate adjustment for differences in the injection times of the treatments. Efficiency is the ratio of the fracture volume to the injected volume before pumping is stopped. As illustrated on Fig. 6L-1, it defines the area under the ramp addition curve. This scheduling technique is reviewed here and generalized to include the effect of fluid-loss spurt.

Conceptually, spurt loss occurs only during the addition of new fracture area and before proppant reaches the fracture tip and halts fracture extension. Therefore, for normal design practices (see Section 5-1.1), spurt loss S_p occurs only for the pad fluid and must be isolated from the efficiency η to estimate the pad volume. The modified efficiency η_c excluding spurt, which reflects only the C_L component of fluid loss, can be found from Nolte (1989) as

$$\eta_c = 1 - \frac{1 - \eta}{\kappa}; \quad \kappa = 1 + \frac{S_p}{g_0 C_L \sqrt{t_s}} \quad (6L-1)$$

$$f_{LS} = \frac{(\kappa - 1)(1 - \eta)}{\kappa} = (1 - \eta) - (1 - \eta_c), \quad (6L-2)$$

where κ is the spurt factor for the case of total fluid loss with spurt relative to the case with no spurt and $\kappa = 1$, $g_0 \equiv 1.5$ (see Chapter 9), C_L is the leakoff coefficient, t_s is the time of tip screenout or injection without a screenout, and f_{LS} is the volume fraction lost to spurt during pumping. Various means for obtaining the value of κ are discussed in Chapter 9.

The pad fraction is defined as the ratio of the pad volume to the total fluid and proppant volume injected during time t_s . In the absence of spurt loss ($\kappa = 1$), the pad fraction can be expressed in various forms:

$$f_p(\eta) \equiv \frac{(1 - \eta)^2}{(1 + \eta)} = \frac{1}{(1 + 2f_L)} \equiv \frac{1}{(1 + G^*)}, \quad (6L-3)$$

where f_L is the ratio of fracture to loss volume during injection and is equal to $\eta/(1 - \eta)$, and G^* is the decline analysis variable discussed in Chapter 9. The pad relation $(1 - \eta)^2/(1 + \eta)$, which can be alternatively expressed as shown. Numerically simulated pad data fall between the two relations. When the spurt loss becomes significant ($\kappa > 1$), the pad fraction is composed of two components: the first is equivalent to the no-spurt case given by Eq. 6L-3 and uses a value of η_c that excludes spurt loss, and the second is the contribution of spurt using Eq. 6L-2:

$$f_p(\kappa > 1) = f_p(\eta_c) + f_{LS} \quad (6L-4)$$

Figure 6L-1. Dimensionless proppant concentration versus dimensionless injected volume.

In addition to the pad, the schedule requires the volume fraction of proppant f_v to be added following the pad (Nolte, 1986b)

$$f_v(\tau) = f_0 \tau^\varepsilon; \quad \varepsilon = \frac{(1 - f_p - \eta)}{\eta}; \quad 0 < \tau < 1 \quad (6L-5)$$

to approximate a spatially uniform concentration of f_0 at the end of pumping. The dimensionless slurry time τ is 0 when proppant addition begins and unity when pumping stops. This definition provides that $f_p + \tau$ reflects the total time. Equation 6L-5 is illustrated as the curve in Fig. 6L-1, which also shows the division of volume between the pad fraction and the slurry fraction f_s . The definition of ε leads to the shaded area under the f_v curve, which is equal to the efficiency. The remaining area is $1 - \eta$, which reflects the ratio of the loss volume to the injected volume.

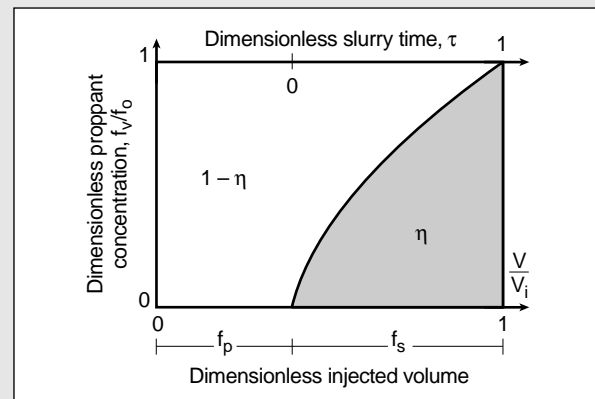
For scheduling a TSO treatment to achieve the final fracture volume V_f relative to that at screenout V_{fso} , Nolte's (1990) result can be extended to include spurt:

$$\frac{V_f(\Delta t_D)}{V_{fso}} = 1 + \frac{\Delta t_D}{\eta_{so}} + \frac{1 - \eta_{so}}{\kappa \eta_{so}} \left\{ \frac{g(\Delta t_D)}{g_0} - 1 \right\} \quad (6L-6)$$

$$\eta_p = \frac{\eta_{so}}{1 + \Delta t_D} \frac{V_f(\Delta t_D)}{V_{fso}}; \quad \Delta t_D = \frac{(t_p - t_{so})}{t_{so}} \quad (6L-7)$$

$$g(\Delta t_D) = (1 + \Delta t_D) \sin^{-1}(1 + \Delta t_D)^{-1/2} + \Delta t_D^{1/2}, \quad (6L-8)$$

where Δt_D is the dimensionless time after screenout, η_{so} and η_p are the respective efficiencies at screenout and end of pumping, t_p is the total pumping time, and t_{so} is the time at screenout. The term $g(\Delta t_D)$ is the low-efficiency dimensionless fluid-loss function defined in the Appendix to Chapter 9, which also provides additional TSO relations. Low efficiency is typical for TSO treatments. The ratio of fracture volumes defined by Eq. 6L-6 can be replaced by the ratio of corresponding average widths, as graphically represented in Fig. 10-15 for various efficiency values. For proppant scheduling, the pad volume to achieve the TSO is found by using Eq. 6L-4 with η_{so} and f_{LS} corrected for spurt by Eqs. 6L-1 and 6L-2. The proppant addition is obtained from Eq. 6L-5 in terms of the final efficiency η_p . From a practical standpoint and to avoid proppant screenout midway in the fracture, the pad can be extended by a low-proppant-concentration stage, as discussed in Section 10-4.2.



only when the final design is simulated. Depending on the required conductivity, proppant of smaller diameter may be used for the treatment.

The method described here can be extended to TSO designs by specifying both the fluid concentrations and the desired areal concentration (e.g., 1 lbm of proppant per square foot of fracture face area). The simulator is run as previously described, except that once the design length is reached, length extension is artificially prevented and pumping continued until the fracture width is sufficient to obtain the desired areal concentration. The design of TSO treatments is discussed in Chapter 10.

6-12. Pressure history matching

One of the most difficult and expensive aspects of a well-engineered fracture design is obtaining the input required for the design simulators. Formation data, such as stresses, permeability and elastic properties,

are rarely well known. Obtaining such data is frequently difficult, expensive or both. This section describes a method to obtain data from the postjob analysis of pressure recorded during a treatment.

The only direct output from the formation during a fracture treatment is the pressure history measured during and after pumping the treatment. Chapter 9 discusses the interpretation of these pressure records in detail. However, these analyses can be only quantitatively accurate for relatively simple fracture geometries. This section considers the application of a formal theory of inversion (see Sidebar 6M) to complement qualitative interpretation and to increase the quantitative information available from the pressure record.

Inverse analysis is a method of characterizing a system from its response to an imposed input. In the case of hydraulic fracturing, the system is the reservoir, surrounding layers, the well and all associated parameters. The input is the pumping of a fluid, and the response is the pressure recorded during the treatment. The pressure record is analyzed to extract the proper-

6M. Theory and method of pressure inversion

The first step in the application of pressure history inversion is parameterization of the problem. This involves defining which properties are to be determined as well as setting bounds on their values and relations between values of different parameters. For example, it may be assumed that the stress in a layer is between 5000 and 6000 psi and that the stress in a neighboring layer is between 500 and 1000 psi higher. If the parameters are represented by the vector \bar{x} and the pressure record by \bar{p} :

$$\bar{p} = F(\bar{x}), \quad (6M-1)$$

where F represents the mechanics of fracture development and relates the observed pressure to the input parameters. The pressure vector is the sequence of discrete pressures measured during the treatment. The vector \bar{x} may be a list of selected parameters, such as

$$\bar{x} = [h_f, E', \sigma], \quad (6M-2)$$

indicating that the parameters to be found are the fracture height, Young's modulus and stress, and it is assumed that all other parameters are specified. Symbolically, the inversion process can be written as

$$\bar{x} = F^{-1}(\bar{p}), \quad (6M-3)$$

which is analogous to inverting a matrix to solve a set of linear equations with a known right-hand side. In this case, however, the known vector \bar{p} is the sequence of pressure readings, the relation is highly nonlinear and cannot be solved directly, and there are many more pressure readings than there are unknown parameters.

Two cases can be distinguished: the measured data defined by

$$\bar{p}_{meas} = F_{meas}(\bar{x}) \quad (6M-4)$$

and the simulated data defined by

$$\bar{p}_{sim} = F_{sim}(\bar{x}). \quad (6M-5)$$

Equations 6M-4 and 6M-5 imply that if a model is used to calculate the pressure data for a given set of parameters, it will generate a pressure record. Similarly, in the field, a pressure record is generated by the system with a set of parameters. The function F also has subscripts *sim* and *meas* to emphasize that the model is not an exact representation of reality, so even if the correct \bar{x} is found, the calculated and measured pressures may not agree. For example, if the PKN model is selected to match the data but if significant height growth has occurred, the pressure record generated by the correct \bar{x} will not match the measured pressure.

The objective of pressure history inversion is to minimize the difference between the measured and calculated pressure records, defined using an error function:

$$\varepsilon = \left(\sum_i W_i |P_{sim,i} - P_{meas,i}|^r \right)^{1/r}, \quad (6M-6)$$

where the weighting factors W_i are typically set to 0 for points to be ignored and to 1 for all other points. The points can also be weighted according to the range of interest. For example, if only the decline period is to be matched, W_i is set to 0 for all points during pumping. The minimization of ε can be performed numerically by a routine in a standard numerical library. Essentially, the algorithm consists of selecting a sequence of sets of parameter values until a satisfactory match is obtained, similar to the 1D Newton-Raphson method (Press *et al.*, 1986) for solving a single nonlinear equation.

ties of the formation so that the fracture geometry can be determined.

This approach is common in well testing, and some of the same pitfalls and limitations should be noted. For example, the pressure record should not be assumed to be the only information available. Other information, such as logs, should be used to narrow the expected ranges of parameters or to specify relations between them. In addition, the selection of the model types to be used should be made logically on the basis of other data. This is analogous to well test interpretation (Gringarten *et al.*, 1974), in which diagnostic plots and the knowledge of boundary conditions are used to specify model type (e.g., infinite reservoir versus rectangular bounded reservoir) before using an analysis package to determine the best estimates of permeability, height, etc. If this preanalysis is not done, there is a high risk of obtaining a good match to the pressure history with the incorrect parameters because of the nonuniqueness of the response; i.e., two different sets of inputs may provide the same output pressure. Gulrajani *et al.* (1996) discussed nonuniqueness in detail. Other limitations of pressure history inversion analysis are the ability of the algorithm to represent the mechanics and the time requirements for computer processing if a sophisticated fracture model is used.

Piggott *et al.* (1992) described a method for performing fracturing pressure history inversion to obtain formation properties. These properties can be used in future designs for wells in the same field and also to confirm or refute the assumptions of the design of the pumped treatment. For example, if the postjob application of pressure history inversion analysis indicates that the stresses in the barriers were smaller than expected, resulting in the occurrence of significant height growth, the effect on geometry would be quantified (i.e., significant height growth at the expense of reduced length in the pay zone, possibly reducing production significantly). This information could then be used to adjust predictions for production from that well and to modify input parameters for future well designs. Pressure history inversion applied on a calibration treatment could be used to redesign the main treatment.

A well-characterized data set is desirable for evaluating any pressure history inversion algorithm. Piggott *et al.* used field experiments conducted by the Gas

Research Institute (Robinson *et al.*, 1991) to evaluate a pressure history inversion algorithm. These experiments are ideal for this purpose, because more data were gathered in these wells than in typical commercial wells. Figure 6-24 shows the pressure match obtained by inverting the perforation diameter and the stresses in the layers bounding the pay zone in one well. For comparison, the inverted values of the diameter and stresses are listed in Table 6-1 (Robinson *et al.*, 1991). Gulrajani *et al.* (1996) also presented several field applications of pressure history inversion. These examples show the wide range of applicability of the technique, as well as the quality of the results that can be obtained by its application.

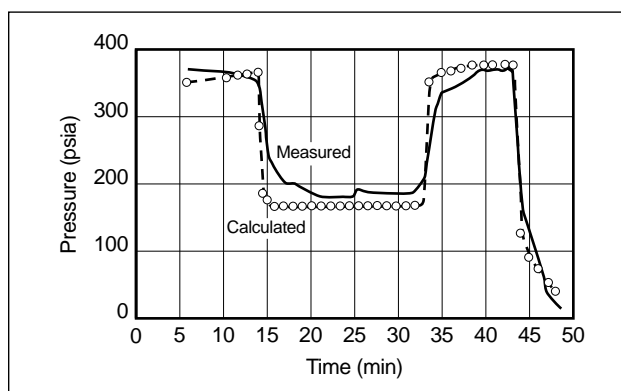


Figure 6-24. Pressure match obtained using pressure history inversion (Piggott *et al.*, 1992).

Table 6-1. Parameters assumed and from data inversion (P3D model single-layer simulation) (Robinson *et al.*, 1991).

Assumed parameters	
Young's modulus	8×10^6 psi
Poisson's ratio	0.3
Fluid-loss height	42 ft
Closure pressure	6300 psi
Number of perforations	35
Leakoff coefficient	$0.0037 \text{ ft}/\text{min}^{1/2}$
Initial fracture height	120 ft
Parameters from inversion	
Stress contrast below pay zone	337 psi
Stress contrast above pay zone	186 psi
Perforation diameter	0.18 in.